

16. Site 851¹

Shipboard Scientific Party²

HOLE 851A

Date occupied: 16 June 1991
Date departed: 16 June 1991
Time on hole: 7 hr, 47 min
Position: 2° 46.223'N, 110° 34.308'W
Bottom felt (rig floor; m, drill-pipe measurement): 3773.0
Distance between rig floor and sea level (m): 11.7
Water depth (drill-pipe measurement from sea level, m): 3761.3
Total depth (rig floor, m): 3779.5
Penetration (m): 6.5
Number of cores (including cores with no recovery): 1
Total length of cored section (m): 6.5
Total core recovered (m): 6.45
Core recovery (%): 99.2
Oldest sediment cored:
Depth (mbsf): 6.5
Nature: foraminifer nannofossil ooze
Earliest age: Pleistocene

HOLE 851B

Date occupied: 16 June 1991
Date departed: 19 June 1991
Time on hole: 2 days, 4 hr, 7 min
Position: 2° 46.223'N, 110° 34.308'W
Bottom felt (rig floor; m, drill-pipe measurement): 3772.0
Distance between rig floor and sea level (m): 11.7
Water depth (drill-pipe measurement from sea level, m): 3760.3
Total depth (rig floor, m): 4092.5
Penetration (m): 320.5
Number of cores (including cores with no recovery): 34
Total length of cored section (m): 320.5
Total core recovered (m): 318.05
Core recovery (%): 99.2
Oldest sediment cored: 318.0
Depth (mbsf): 320.5
Nature: diatom nannofossil ooze
Earliest age: late Miocene
Basement:
Depth sub-bottom (m): 320.5
Nature: basalt fragment

HOLE 851C

Date occupied: 19 June 1991
Date departed: 19 June 1991
Time on hole: 14 hr, 50 min
Position: 2° 46.214'N, 110° 34.294'W
Bottom felt (rig floor; m, drill-pipe measurement): 3772.0
Distance between rig floor and sea level (m): 11.7
Water depth (drill-pipe measurement from sea level, m): 3760.3
Total depth (rig floor, m): 3907.5
Penetration (m): 135.5
Number of cores (including cores with no recovery): 14
Total length of cored section (m): 133.0
Total core recovered (m): 136.65
Core recovery (%): 102.7
Oldest sediment cored:
Depth (mbsf): 135.5
Nature: diatom nannofossil ooze
Earliest age: late Miocene

HOLE 851D

Date occupied: 19 June 1991
Date departed: 19 June 1991
Time on hole: 1 hr, 58 min
Position: 2° 46.214'N, 110° 34.294'W
Bottom felt (rig floor; m, drill-pipe measurement): 3772.0
Distance between rig floor and sea level (m): 11.7
Water depth (drill-pipe measurement from sea level, m): 3759.3
Total depth (rig floor, m): 3791.0
Penetration (m): 19.0
Number of cores (including cores with no recovery): 2
Total length of cored section (m): 19.0
Total core recovered (m): 20.1
Core recovery (%): 105.8
Oldest sediment cored:
Depth (mbsf): 19.0
Nature: foraminifer nannofossil ooze
Earliest age: Pleistocene

HOLE 851E

Date occupied: 19 June 1991
Date departed: 21 June 1991
Time on hole: 1 day, 17 hr, 6 min
Position: 2° 46.213'N, 110° 34.289'W

¹ Mayer, L., Pisias, N., Janecek, T., et al., 1992. *Proc. ODP, Init. Repts.*, 138: College Station, TX (Ocean Drilling Program).

² Shipboard Scientific Party is as given in list of participants preceding the contents.

Bottom felt (rig floor; m, drill-pipe measurement): 3772.0
Distance between rig floor and sea level (m): 11.7
Water depth (drill-pipe measurement from sea level, m): 3760.3
Total depth (rig floor, m): 4090.4
Penetration (m): 318.4
Number of cores (including cores with no recovery): 35
Total length of cored section (m): 318.4
Total core recovered (m): 316.69
Core recovery (%): 99.5
Oldest sediment cored:
 Depth (mbsf): 318.14
 Nature: foraminifer diatom nannofossil ooze
 Earliest age: late Miocene
Basement:
 Depth sub-bottom (m): 318.4
 Nature: unknown

Principal results: Site 851 is the fourth of our seven-site, north-south transect along 110° W. The site is presently located near the northern limit of the westward-flowing South Equatorial Current (SEC). This site, along with the other sites drilled along this transect, will provide material for detailed studies of equatorial circulation of the last 10 m.y. The transect also serves as the eastern end-member of a series of studies (Legs 85 and 130) aimed at understanding the regional and global response of the equatorial Pacific Ocean to changes in climate.

Five holes were drilled at Site 851. Hole 851A was a single APC mud-line core dedicated to whole-round geochemical and physical property measurements. Hole 851B was APC-cored to 140.5 mbsf, before excessive overpull required switching to the XCB-coring system. This hole was continued to 320.5 mbsf, where we reached the basement. After we completed three logging runs in Hole 851B, we APC-cored Hole 851C to a depth of 135.5 mbsf. Hole 851D, dedicated for detailed paleomagnetic studies, was APC-cored to 19.0 mbsf. Finally, Hole 851E was APC-cored to 133 mbsf, when we continued with the XCB to a total depth of 318.4 mbsf, when again, the basement was reached. Triple APC- and double XCB-coring at this site, combined with real-time analyses of continuous GRAPE density, susceptibility, and color reflectance data showed that 100% of the section had been recovered between 0 to 133 mbsf and that in the remaining section, only five short intervals had not been fully recovered. The composite section we constructed from carefully splicing the overlapping holes suggests that gaps between successive cores are different for APC- and XCB-cored intervals. We estimated that a single APC-core recovered about 90% of a section, while a single XCB-core recovered about 75% of a section.

The sedimentary sequence at Site 851 spans the interval from the uppermost middle Miocene to the Pleistocene and can be described as a single lithologic unit composed of a mixture of foraminifer nannofossil and diatom nannofossil oozes. The interval between 205 and 287 mbsf is dominated by diatom nannofossil ooze with interbeds of diatom ooze that range in thickness from a few centimeters to 10 m. As with many of the equatorial sites of Leg 138, laminated diatom-rich intervals were found. At Site 851, these intervals were located just above a chert horizon at about 280 mbsf.

Sediments from the upper 80 m of Site 851 display stable magnetic remanence. A magnetostratigraphy, spanning from the Brunhes Chron to the Cochiti Subchron, can be identified for the past 4 m.y. The three holes that reached the early Matuyama contain a correlatable feature that might correspond to the Reunion event. Within the Cochiti Subchron, all three deeper holes have similar fine-scale structure in their declination profiles. When combined with Site 848 and the short magnetic interval of Site 850, this site provides important magnetostratigraphic control for the 110° W transect.

Biostratigraphic age control was provided by all four of the chief planktonic microfossil groups. Calcareous nannofossils are abundant and well preserved throughout the sequence, while planktonic foraminifers are

abundant and poorly to moderately well preserved. Radiolarians are common to abundant and moderately well to well preserved throughout the section, down to just above the basement. Diatoms are rare to abundant throughout the section. Diatom preservation is moderate to good in the Pleistocene through the upper Miocene and poor in the middle Miocene.

Sedimentation rates at this site were moderate during the late Pliocene and Pleistocene, ranging from 15 to 20 m/m.y. During the late Miocene and early Pliocene, rates were relatively high, ranging from 40 to 65 m/m.y. In the lower part of the section, 7 to 10 Ma, sedimentation rates are about 35 m/m.y. The temporal pattern of sedimentation rates at Site 851 follows that of the other sites drilled along the 110°W transect (and elsewhere in the equatorial Pacific Ocean), but with slightly lower average rates reflecting its more northerly position.

Three logging runs were completed that included geophysical and geochemical tool strings and the formation microscanner. For the most part, variability in the logs reflects changes in the calcium carbonate content of the sedimentary sequence and shows a high degree of correlation with directly measured sediment properties, such as GRAPE density. From FMS data, we were able to identify thin chert intervals in a 9-m section that had not been recovered using the XCB-coring system. The chert in Site 851 seems less well developed than that in Site 850.

Interstitial-water chemistry data at Site 851 show a continuation of trends identified from the sites along the southern end of the 110° W transect. At this site, the intensity of reducing conditions is much less than it is at Sites 849 and 850, located to the south within the high productivity region of the equatorial divergence. Unlike Site 850, where the presence of chert may have partitioned the water column profiles into two different regimes, the chert found at Site 851 seems to have had little impact on pore-water chemistry. Finally, the pore waters at Site 851, like other sites along the western transect, show little influence of basement alteration, which suggests that either conditions near the basement were not conducive to extensive low-temperature weathering of basement or that lateral advection of water overwhelmed the effects of alteration.

The combination of moderately high sedimentation rate, magnetic stratigraphy, and good microfossil preservation makes Site 851 the "mother-lode" of the 110° W transect, with excellent shows of paleomagnetic "gold" and paleoceanographic "platinum." At the conclusion of Site 851, Leg 138 paleomagnetists had completed 8.9 log (m²kt).

BACKGROUND AND SCIENTIFIC OBJECTIVES

Site 851 is located near the northern extent of the westward-flowing South Equatorial Current (SEC; Fig. 1) and near the southern limit of the seasonal migration of the boundary between the North Equatorial Countercurrent (NECC) and the SEC. Objectives at this site were to provide a record of the history of the SEC as well as to document the movement of the boundary between the SEC and the NECC.

Site 851 is situated on crust formed at the East Pacific Rise (Fig. 2). Based on estimates of basement subsidence and spreading rates for this sector of the Pacific Ocean, we expected the basement age at this site to be approximately 12 to 13 Ma. A detailed site survey of the area was conducted as part of the *Thomas Washington* Venture 1 cruise. The site is on a broad northwest-southeast-trending topographic high and has somewhat complex basement relief (Fig. 3). The complexity of the basement structure is mirrored (though in a subdued manner) in the surface relief. However, Site 851 lies in an area of relatively flat basement and thus relatively flat seafloor terrain (Fig. 4). The average sediment thickness around the site is approximately 330 m. The numerous flat-lying reflectors draping over the basement topography imply fairly undisturbed pelagic accumulation.

OPERATIONS

Transit to Site 851

The transit to Site 851 covered 81 nmi in 7 hr at an average speed of 11.6 kt. Upon reaching the first survey way point at 1400 hr (All times reported in this section are local time, L, where local time =

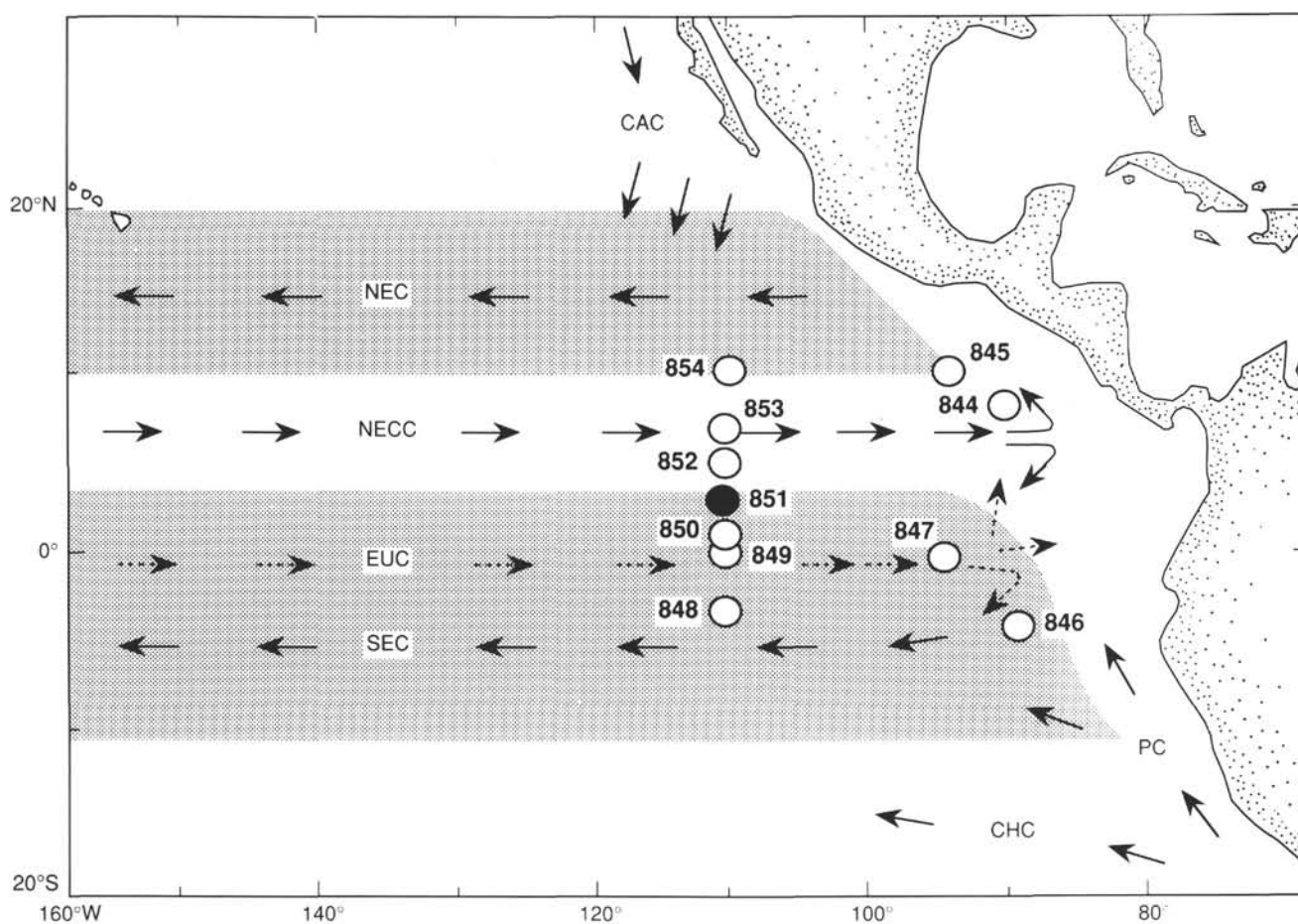


Figure 1. Location of Site 851 and generalized circulation system of the eastern equatorial Pacific Ocean. Other Leg 138 sites are shown for reference. Surface current shown as solid arrows, subsurface current as dashed arrows. CAC = California Current; NEC = North Equatorial Current; NECC = North Equatorial Countercurrent; EUC = Equatorial Undercurrent; SEC = South Equatorial Current; PC = Peru Current; and CHC = Chile Current. Shaded area illustrates general latitudinal extent of the SEC and NEC.

Universal Time Coordinated [UTC] minus 7 hr. All times reported in Table 1 are UTC.) 16 June, the seismic equipment was deployed and a 1-hr survey began. After deployment of a beacon at 1500L, the survey was continued past the site for 10 min. After the survey was completed, the *JOIDES Resolution* was returned to the site, and the thrusters and hydrophones were lowered by 1600L. Based upon the precision depth recorder (PDR), the depth to the seafloor was 3775.9 mbrf.

Hole 851A

This hole was dedicated to whole-round geochemical and physical property sampling. The first (and only) core for this hole was on deck at 2306L June 16 and from it 6.45 m of sediment was recovered, establishing the mud line at 3773.0 mbrf (see Table 1 for a summary of coring operations). After retrieval of Core 138-851A-1H, the bit was pulled above the mud line to begin the next hole.

Hole 851B

Core 138-851B-1H was on deck at 2400L 16 June. From this core, 7.58 m of sediment was recovered. Piston coring continued through Core 138-851B-13H (121.5 mbsf), and orientation began on the fourth core. An overpull of 100,000 lb was encountered during the retrieval of Core 138-851B-13H, which required a switch to XCB-coring at this point. Average sediment recovery for the APC section was 105%.

Coring proceeded with the XCB-coring system until 318 mbsf (Core 138-851B-34X), where contact with basement was indicated by a marked decrease in the rate of penetration. After being cored for an additional 20 min, the hole was deepened to only 320.5 mbsf. The bottom of the core (-34X) contained basaltic fragments, which confirmed contact with the basement. As depth objectives for the hole at this point had been reached, it was prepared for logging. Recovery in the XCB section was 94.8%.

Logging Operations at Hole 851B

The hole was swept with mud, and pipe was set to a logging depth of 62.0 mbsf. All three standard ODP tool strings were run, and we had only a few operational problems (Table 2). The heave compensator did not function properly; therefore, we logged the hole without it. However, seas were calm and swells remained below 2 to 3 ft high.

Hole 851B was first logged with the geophysical tool string. The downgoing log was stopped at 178.0 mbsf because of software problems. Both the main logging (323.1–83.8 mbsf) and repeat (175.3–89.9 mbsf) passes went smoothly.

Next, the hole was logged with the geochemical tool string. To minimize activation of the borehole, the same GST calibration procedure was used as that in Hole 850B. The tool string was lowered to total depth, and several meters of extra cable were payed out. Then, the GST was calibrated as the slack was pulled out of the cable. Calibration was finished before the tool had moved more than 1 m in

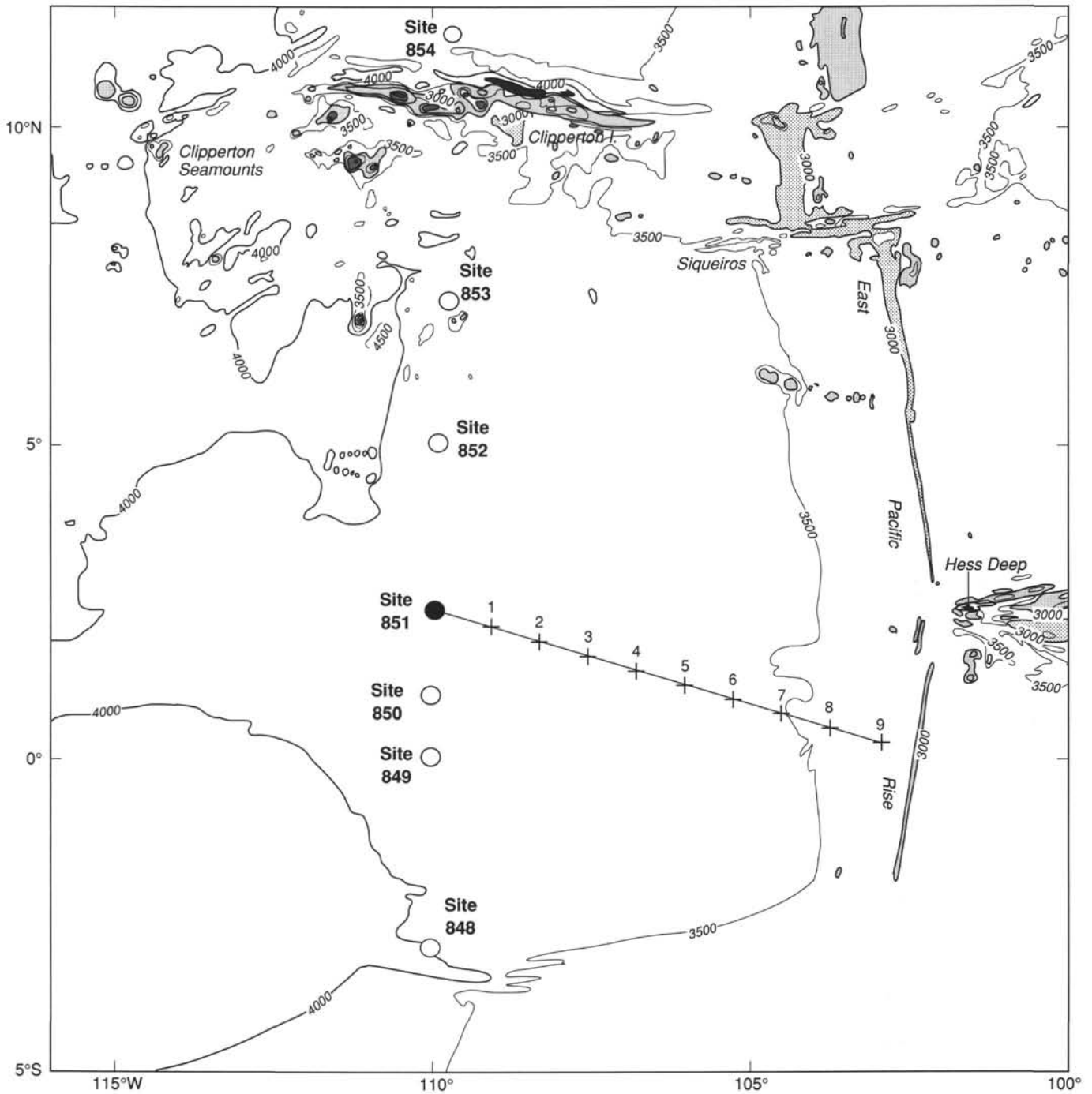


Figure 2. Generalized bathymetric map showing location of Site 851 and other Leg 138 sites drilled along the 110°W transect (from Mammerickx, 1989). Backtracked path of Site 851 (using the pole of rotation of van Andel et al., 1975) is shown for 1 m.y. increments. Bathymetry in meters.

the borehole. No spikes from hole activation during calibration should be in the records. The geochemical log was run from 321.9 mbsf to the mud line. When the GST entered the pipe, however, it lost its calibration and did not respond properly during the remaining pass up to the mud line.

The FMS was run from 323.1 to 219.5 mbsf and again from 323.1 to 68.6 mbsf. Logging with the FMS proceeded smoothly, and at the end of the second run, the tool string was brought into the pipe with none of the caliper-closing problems encountered in previous holes. At the conclusion of logging, we pulled the drill string out of the hole,

and the bit cleared the mud line at 0254L 19 June, thereby ending Hole 851B.

Hole 851C

This hole was drilled to ensure an overlap in the APC-cored section and to provide enough material for high-resolution sampling. The *JOIDES Resolution* was offset 20 m south, and the bit washed down 2.5 mbsf, where the first piston core was taken at 0420L 19 June. Piston coring advanced without any problems to 135.5 mbsf (Core 138-

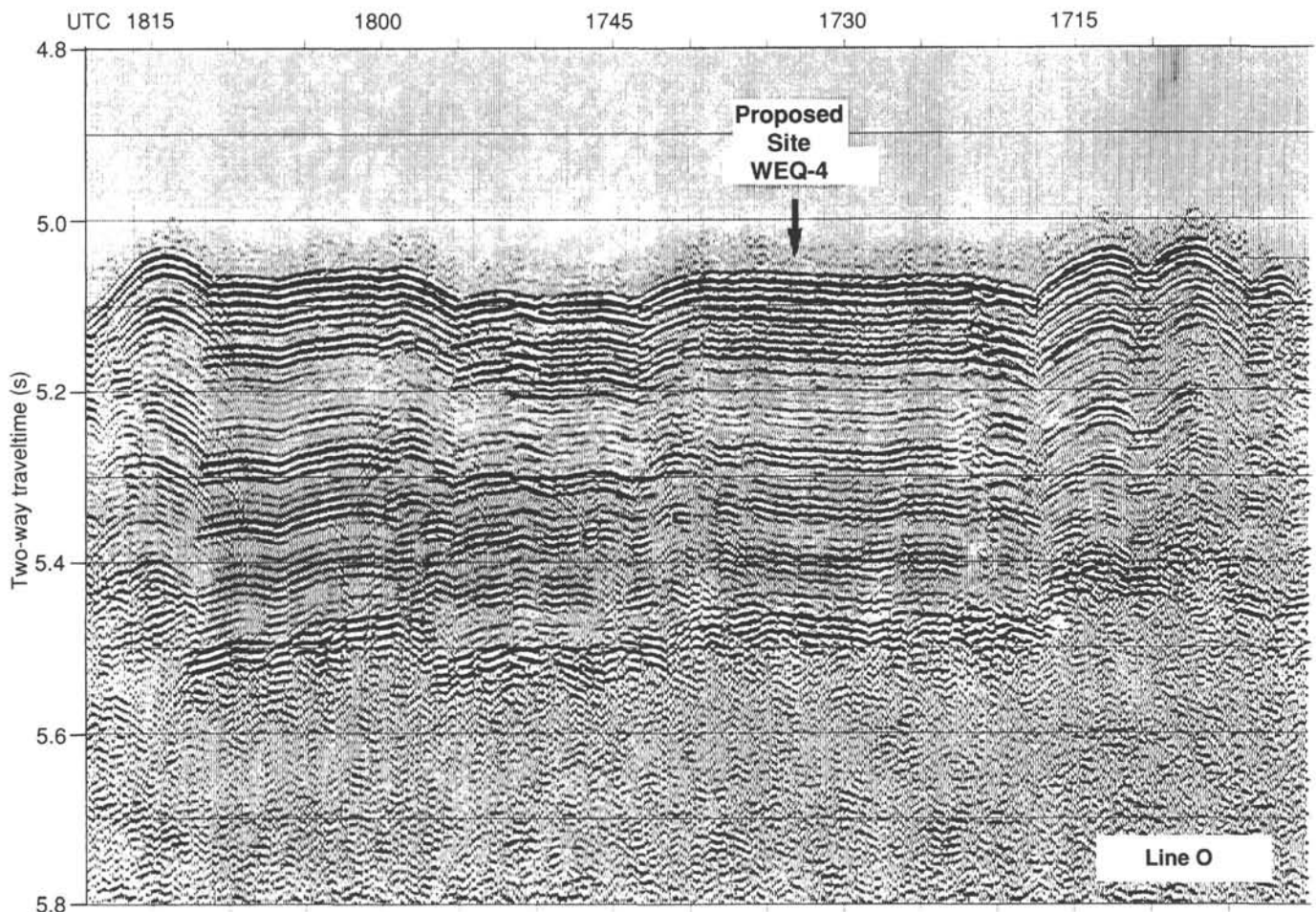


Figure 4. Analog seismic line collected with an 80-in.³ water gun during the *Thomas Washington* cruise, Venture 1. Proposed Site WEQ-4 is shown.

bility, and color reflectance data (see “Sedimentation Rates” section, this chapter) and visual descriptions of lithologic changes. The sedimentary sequence consists mainly of nanfossil ooze with varying amounts of foraminifers and radiolarians; however, one interval was dominated by diatom ooze (Fig. 5).

The lithologic description is based on lithologic parameters that included continuously measured density (GRAPE), magnetic susceptibility, and color reflectance (Fig. 6), as well as percentages of components from smear slides, visual color, and sedimentary structures. Logging measurements (velocity, resistivity, density, Ca-yield, and FMS) (see “Downhole Measurements” section, this chapter), CaCO₃ and organic carbon analyses (see “Organic Geochemistry” section, this chapter), and laboratory measurements of density and water content (see “Physical Properties” section, this chapter) also were used to characterize lithologic changes.

Description of Units

Lithologic Unit I

Intervals:

- Core 138-851A-1H
- Cores 138-851B-1H through -34X
- Cores 138-851C-1H through -14H,
- Cores 138-851D-1H through -2H
- Cores 138-851E-1H through -35X

Age: Pleistocene to middle Miocene

Depth: 0–6.45 mbsf, Hole 851A; 0–321.49 mbsf, Hole 851B; 0–136.14 mbsf, Hole 851C; 0–19.5 mbsf, Hole 851D; 0–318.14 mbsf, Hole 851E

The primary variability in lithology at Site 851 can be characterized by the relative proportions of biogenic carbonate and silica. Thus, changes in measurements of percentage of CaCO₃ (see “Organic Geochemistry” section, this chapter) provide a first-order index of lithologic variations. Sediments at the top and bottom of the sequence have higher percentages of CaCO₃ with less variability ($76 \pm 8\%$, 0–220 mbsf; $75 \pm 8\%$, 290 mbsf–basement) than the interval between 220 and 290 mbsf, which has lower and more variable percentages of CaCO₃ ($57 \pm 17\%$). Smear slide estimates of carbonate content (%foraminifer + %nanfossil) are in agreement with the general pattern indicated by measurements of percentages of CaCO₃ (Fig. 7). Clay is rare.

Superimposed on the first-order variations in the relative proportion of carbonate and silica are changes in the fossil groups that contributed to these components, changes in organic carbon content and diagenesis, and changes in physical properties because of lithology and compaction with depth. The lithologic description has been organized into four depth intervals on the basis of a synthesis of the lithologic parameters measured.

The uppermost interval (0–86.9 mcd; 0–6.45 mbsf, Hole 851A; 0–76.5 mbsf, Hole 851B; 0–75.4 mbsf, Hole 851C; 0–19.5 mbsf, Hole 851D; 0–76.4 mbsf, Hole 851E) is dominated by foraminifer nanfossil ooze of Pleistocene to early Pliocene age. The sediments contain 30% to 80% nanfossils, 10% to 40% foraminifers, 2%–30% radiolarians, 2%–20% diatoms, and 0%–10% clay.

The foraminifer nanfossil ooze is interbedded with sediments that contain up to 30% radiolarians and 25% diatoms. Meter-scale

variability in measured lithologic parameters (e.g., GRAPE density and water content) is associated with changes in the ratio of nanofossils to biogenic silica (radiolarians and diatoms).

From 0 to 5.65 mbsf, the sediment contains iron and manganese oxides and is grayish-brown (10YR 4/2), very pale brown (10YR 7/3), and light gray (10YR 7/4). In Section 2 of Cores 138-851A-1H, -851B-1H and -851E-1H, and Section 1 from Core 138-851D-1H, three grayish-brown intervals appear to correlate among holes (Fig. 8). Differences in the thickness of these bands in the four holes may indicate local variations in sedimentation, slight differences in the intensity of bioturbation, or stretching of the sediment during core recovery. Below the oxidized/reduced transition at 5.65 mbsf, the sediment is white (N8, N9, 5Y 8/1), light gray (5Y 7/1), and gray (5Y 6/1). Light greenish-gray (5G 7/1) and gray (N6) diagenetic bands are common, contain an unidentified sulfide mineral other than pyrite, and are associated with small amplitude (approximately $1-5 \times 10^{-5}$ SI) spikes in magnetic susceptibility. Burrowing and mottling in this interval is slight to moderate.

Between approximately 76.5 and 205.0 mbsf in Hole 851B, 75.4 and 136.14 mbsf in Hole 851C, and 76.4 and 202.55 mbsf in Hole 851E, the sediments (of early Pliocene to late Miocene age) are dominated by diatom nanofossil ooze with minor amounts of radiolarians (1%–20%) and foraminifers (2%–25%).

Decimeter-scale interbeds throughout this section are associated with small-scale variations in GRAPE density and color and probably are related to changes in the proportion of diatoms to nanofossils.

The diatom nanofossil ooze interval is light gray (N7 and 5Y 7/1) to white (N8) with intervals and burrows filled with light yellowish-gray (5Y 8/1) sediment. Gray (N6) diagenetic bands and laminations are common, and light greenish-gray (5G 7/1) bands are less common, but present throughout. Gray (N5) spots and streaks of pyrite are also present throughout. The light greenish-gray bands and the darkest gray bands often are associated with very small peaks in susceptibility. Bioturbation, pyrite mottling, and burrow fills and bands of diatom-rich sediment are much more common in this section than in the overlying foraminifer nanofossil ooze and the underlying interval of interbedded nanofossil and diatom oozes.

Between 205.0 and 287.0 mbsf in Hole 851B and 202.55 and 285.5 mbsf in Hole 851E, the sediments (of late Miocene to middle Miocene age) are dominated by diatom nanofossil ooze and interbedded with diatom ooze of varying thickness (a few centimeters to 10 m). The highest abundances of radiolarians at the site are found in this interval (0%–25%, average: ~10%). Foraminifers vary from 0% to 21%, but are generally about 4%, and clay is present in very low concentrations (2%). Calcium carbonate contents are lower and more variable than above ($57 \pm 17\%$). Concentrations of nanofossils (10%–90%, average: 40%) and diatoms (2%–85%, average, 40%) also are variable. Density (GRAPE, gravimetric, and logging measurements, Fig. 6) and logging resistivity values are generally lower and more variable in this interval than elsewhere in the site. Water content values are as high in this interval as they are in the foraminifer nanofossil ooze, but are much more variable (see “Physical Properties” section, this chapter). This interval also is distinguished by its low reflectance and high susceptibility values (see “Color Reflectance” and “Susceptibility” sections, this chapter).

Like the overlying interval of diatom nanofossil ooze, the interval between 205 and 287 mbsf has large-scale (5- to 15-m-thick) variations in lithology with more siliceous sections centered at 230, 250, and 265 mbsf. Each of these sections contains interbeds of nanofossil diatom ooze with up to 80% diatoms, mostly *Thalassiothrix longissima*. Thin (10–20 cm) laminated interbeds of nanofossil diatom ooze within the high-silica sections are centered at 250 mbsf (Fig. 9). A thick (about 2 m) interval of laminated diatom ooze (Fig. 10) was recovered in the bottom of Core 138-851B-29X (1.5 m in Core 138-851E-30X) above chert fragments in the core catchers of Cores 138-851B-29X (272.8 mbsf) and -851E-30X (271.1 mbsf). Recovery was low in the diatom-rich section at 265 mbsf in Holes 851B and

851E, perhaps because of the presence of chert. Only the sequence of laminated diatom ooze directly above this chert was recovered. Resistivity, velocity, and FMS logs (see “Downhole Measurements” section, this chapter) suggest that one thin (2 cm) layer of chert occurs at 273.7 mbsf. The FMS log reveals a discontinuous chert nodule horizon at a few centimeters below this.

The nanofossil-rich sediments within this interval are light gray (N7 and 5Y 7/1), light greenish-gray (5GY 7/1), and white (N8 and 5Y 8/1). The diatom-rich interbeds are primarily olive gray (5Y 5/2), light gray (5Y 7/1), and white (5Y 8/1). The laminated diatom ooze directly overlying the chert in Cores 138-851B-29X and -851E-30X contains some dark greenish-gray (5GY 4/1) and olive (5Y 4/3) laminations as well (Fig. 10). Gray (N6) and light greenish-gray (5G 7/1) color bands (resulting from reduction diagenesis) are present throughout this interval, but in general, pyrite mottling and banding is less common than in the overlying diatom nanofossil ooze interval.

From 287.0 to 321.49 mbsf in Hole 851B and from 285.5 to 318.14 mbsf in Hole 851E, sediments of middle Miocene age are similar to those from ~75 to ~205 mbsf, with high concentrations of nanofossils (30%–90%, average, 60%), low concentrations of foraminifers (about 4%), and widely varying concentrations of radiolarians (1%–30%) and diatoms (4%–65%). Like the upper lithologies of the Site 851 sedimentary sequence, this section has consistently high percentage of CaCO₃ values (about 75%). Small-scale (decimeter) variations in the proportion of diatoms to nanofossils were detected in the GRAPE and reflectance data. The boundary (at 287.0 mbsf) between this interval and the overlying diatom-rich interval is marked by a rapid increase down the core in velocity, resistivity, density, and Ca-yield logs (see “Downhole Measurements” section, this chapter). This change in the log data is consistent with a change from silica-rich sediments above the boundary to carbonate-rich sediments below and is expected as sediments become more compacted with depth. Based on hardness and physical properties, this sediment is probably chalk. Because this shift in the physical properties at 287 mbsf is coincident with a large change in lithology, however, it is difficult to define clearly the zone at which ooze becomes chalk.

Sediments containing iron and manganese oxides are present between 304.3 mbsf and the basement at 320.49 mbsf, Hole 851B (318.14 mbsf, Hole 851E). Manganese oxide dendrites were found throughout the last 18 m above the basement (approximately 302–320 mbsf; Cores 138-851B-33X, -851E-34X, and -35X). Laminations between 319.4 mbsf and the basement (Core 138-851B-34X) may be related to variations in the amount of iron oxides (possibly hematite and goethite), manganese oxides, clay, and nanofossils (Figs. 11 and 12). Some laminated beds (0.2- to 0.4-cm-thick) overlie scoured contacts and have flaser bedding, suggesting that reworking may have occurred.

Between 287 and 304.3 mbsf, the sediments are light gray (5Y 7/1 and 5Y 7/2), light greenish-gray (5GY 7/1), and white (N8, 5Y 8/1), with diagenetic gray (N6) bands and burrow halos. Below 304.3 mbsf, the sediments are pale yellow (2.5Y 8/2 to 5Y 8/3), very pale brown (10YR 8/2 to 10YR 8/3), and brownish-yellow (10YR 6/6). Only slight bioturbation and color mottling are apparent in these sediments just above the basement. Laminations in Core 138-851B-34X are grayish-brown (10YR 5/2), reddish-yellow (7.5YR 7/6), and pale yellow (2.5YR 7/3).

Color Reflectance Spectroscopy

Color reflectance for 511 bands over a range of wavelengths from 450 to 950 nm was measured at intervals ranging from 4 to 8 cm in Site 851. Generally, carbonate-rich sediments have higher reflectance than siliceous sediments. For example, the three broad carbonate minima at 110, 135, and 185 mbsf also are intervals of low reflectance (Fig. 13). The low carbonate content diatom-rich sediments between 230 and 270 mbsf also have low reflectance.

Although carbonate content appears to affect reflectance properties, evidence exists that other lithologic constituents have a

Table 1. Summary of coring operations at Site 851.

| Core no. | Date (June 1991) | Time (UTC) | Depth (mbsf) | Length cored (m) | Length recovered (m) | Recovery (%) |
|---------------|------------------|------------|--------------|------------------|----------------------|--------------|
| 138-851A-1H | 17 | 0605 | 0-6.5 | 6.5 | 6.45 | 99.2 |
| Coring totals | | | | 6.5 | 6.45 | 99.2 |
| 138-851B-1H | 17 | 0700 | 0-7.5 | 7.5 | 7.58 | 101.0 |
| 2H | 17 | 0755 | 7.5-17.0 | 9.5 | 9.67 | 102.0 |
| 3H | 17 | 0840 | 17.0-26.5 | 9.5 | 10.10 | 106.3 |
| 4H | 17 | 0940 | 26.5-36.0 | 9.5 | 9.91 | 104.0 |
| 5H | 17 | 1035 | 36.0-45.5 | 9.5 | 9.89 | 104.0 |
| 6H | 17 | 1130 | 45.5-55.0 | 9.5 | 10.10 | 106.3 |
| 7H | 17 | 1225 | 55.0-64.5 | 9.5 | 10.04 | 105.7 |
| 8H | 17 | 1320 | 64.5-74.0 | 9.5 | 10.04 | 105.7 |
| 9H | 17 | 1425 | 74.0-83.5 | 9.5 | 10.14 | 106.7 |
| 10H | 17 | 1520 | 83.5-93.0 | 9.5 | 9.96 | 105.0 |
| 11H | 17 | 1615 | 93.0-102.5 | 9.5 | 10.01 | 105.3 |
| 12H | 17 | 1720 | 102.5-112.0 | 9.5 | 10.11 | 106.4 |
| 13H | 17 | 1820 | 112.0-121.5 | 9.5 | 10.15 | 106.8 |
| 14H | 17 | 1920 | 121.5-131.0 | 9.5 | 9.87 | 104.0 |
| 15H | 17 | 2020 | 131.0-140.5 | 9.5 | 9.89 | 104.0 |
| 16X | 17 | 2140 | 140.5-150.1 | 9.6 | 9.50 | 98.9 |
| 17X | 17 | 2240 | 150.1-159.8 | 9.7 | 9.77 | 101.0 |
| 18X | 17 | 2335 | 159.8-169.4 | 9.6 | 9.69 | 101.0 |
| 19X | 18 | 0025 | 169.4-179.1 | 9.7 | 9.63 | 99.3 |
| 20X | 18 | 0125 | 179.1-188.3 | 9.2 | 9.83 | 107.0 |
| 21X | 18 | 0215 | 188.3-197.5 | 9.2 | 8.84 | 96.1 |
| 22X | 18 | 0305 | 197.5-207.1 | 9.6 | 9.79 | 102.0 |
| 23X | 18 | 0355 | 207.1-216.8 | 9.7 | 9.77 | 101.0 |
| 24X | 18 | 0445 | 216.8-226.4 | 9.6 | 9.76 | 101.0 |
| 25X | 18 | 0540 | 226.4-236.1 | 9.7 | 9.79 | 101.0 |
| 26X | 18 | 0630 | 236.1-245.8 | 9.7 | 9.15 | 94.3 |
| 27X | 18 | 0730 | 245.8-255.5 | 9.7 | 9.88 | 102.0 |
| 28X | 18 | 0835 | 255.5-265.1 | 9.6 | 9.64 | 100.0 |
| 29X | 18 | 0940 | 265.1-274.8 | 9.7 | 7.73 | 79.7 |
| 30X | 18 | 1040 | 274.8-284.0 | 9.2 | 0.00 | 0.0 |
| 31X | 18 | 1135 | 284.0-293.6 | 9.6 | 9.96 | 104.0 |
| 32X | 18 | 1240 | 293.6-303.2 | 9.6 | 9.34 | 97.3 |
| 33X | 18 | 1345 | 303.2-312.9 | 9.7 | 9.93 | 102.0 |
| 34X | 18 | 1520 | 312.9-320.5 | 7.6 | 8.59 | 113.0 |
| Coring totals | | | | 320.5 | 318.05 | 99.2 |
| 138-851C-1H | 19 | 1120 | 2.5-12.0 | 9.5 | 9.32 | 98.1 |
| 2H | 19 | 1215 | 12.0-21.5 | 9.5 | 9.86 | 104.0 |
| 3H | 19 | 1310 | 21.5-31.0 | 9.5 | 9.94 | 104.0 |
| 4H | 19 | 1410 | 31.0-40.5 | 9.5 | 10.18 | 107.1 |
| 5H | 19 | 1510 | 40.5-50.0 | 9.5 | 8.72 | 91.8 |
| 6H | 19 | 1605 | 50.0-59.5 | 9.5 | 9.99 | 105.0 |
| 7H | 19 | 1700 | 59.5-69.0 | 9.5 | 9.89 | 104.0 |
| 8H | 19 | 1755 | 69.0-78.5 | 9.5 | 9.59 | 101.0 |
| 9H | 19 | 1855 | 78.5-88.0 | 9.5 | 9.43 | 99.2 |
| 10H | 19 | 1955 | 88.0-97.5 | 9.5 | 9.23 | 97.1 |
| 11H | 19 | 2050 | 97.5-107.0 | 9.5 | 10.09 | 106.2 |
| 12H | 19 | 2150 | 107.0-116.5 | 9.5 | 10.15 | 106.8 |
| 13H | 19 | 2250 | 116.5-126.0 | 9.5 | 10.12 | 106.5 |
| 14H | 19 | 2350 | 126.0-135.5 | 9.5 | 10.14 | 106.7 |
| Coring totals | | | | 133.0 | 136.65 | 102.7 |
| 138-851D-1H | 20 | 0205 | 0.0-9.5 | 9.5 | 10.10 | 106.3 |
| 2H | 20 | 0310 | 9.5-19.0 | 9.5 | 10.00 | 105.2 |
| Coring totals | | | | 19.0 | 20.10 | 105.8 |
| 138-851E-1H | 20 | 0355 | 0.0-9.5 | 9.5 | 9.86 | 104.0 |
| 2H | 20 | 0450 | 9.5-19.0 | 9.5 | 9.69 | 102.0 |
| 3H | 20 | 0555 | 19.0-28.5 | 9.5 | 10.06 | 105.9 |
| 4H | 20 | 0700 | 28.5-38.0 | 9.5 | 10.05 | 105.8 |
| 5H | 20 | 0755 | 38.0-47.5 | 9.5 | 10.12 | 106.5 |
| 6H | 20 | 0900 | 47.5-57.0 | 9.5 | 10.11 | 106.4 |
| 7H | 20 | 1000 | 57.0-66.5 | 9.5 | 10.10 | 106.3 |
| 8H | 20 | 1100 | 66.5-76.0 | 9.5 | 9.89 | 104.0 |
| 9H | 20 | 1200 | 76.0-85.5 | 9.5 | 10.10 | 106.3 |
| 10H | 20 | 1305 | 85.5-95.0 | 9.5 | 10.13 | 106.6 |
| 11H | 20 | 1405 | 95.0-104.5 | 9.5 | 10.13 | 106.6 |
| 12H | 20 | 1505 | 104.5-114.0 | 9.5 | 10.11 | 106.4 |

Table 1 (continued).

| Core no. | Date (June 1991) | Time (UTC) | Depth (mbsf) | Length cored (m) | Length recovered (m) | Recovery (%) |
|---------------|------------------|------------|--------------|------------------|----------------------|--------------|
| 13H | 20 | 1605 | 114.0–123.5 | 9.5 | 10.06 | 105.9 |
| 14H | 20 | 1710 | 123.5–133.0 | 9.5 | 10.18 | 107.1 |
| 15X | 20 | 1805 | 133.0–139.0 | 6.0 | 8.94 | 149.0 |
| 16X | 20 | 1900 | 139.0–145.0 | 6.0 | 8.13 | 135.0 |
| 17X | 20 | 1950 | 145.0–154.7 | 9.7 | 9.75 | 100.0 |
| 18X | 20 | 2035 | 154.7–164.3 | 9.6 | 9.70 | 101.0 |
| 19X | 20 | 2130 | 164.3–173.9 | 9.6 | 9.45 | 98.4 |
| 20X | 20 | 2225 | 173.9–183.1 | 9.2 | 9.71 | 105.0 |
| 21X | 20 | 2315 | 183.1–192.3 | 9.2 | 7.01 | 76.2 |
| 22X | 21 | 0000 | 192.3–201.9 | 9.6 | 7.38 | 76.9 |
| 23X | 21 | 0055 | 201.9–211.6 | 9.7 | 9.79 | 101.0 |
| 24X | 21 | 0140 | 211.6–221.2 | 9.6 | 9.87 | 103.0 |
| 25X | 21 | 0230 | 221.2–230.9 | 9.7 | 9.78 | 101.0 |
| 26X | 21 | 0320 | 230.9–240.6 | 9.7 | 9.81 | 101.0 |
| 27X | 21 | 0415 | 240.6–250.3 | 9.7 | 9.83 | 101.0 |
| 28X | 21 | 0510 | 250.3–259.9 | 9.6 | 9.87 | 103.0 |
| 29X | 21 | 0600 | 259.9–269.6 | 9.7 | 9.02 | 93.0 |
| 30X | 21 | 0700 | 269.6–279.3 | 9.7 | 1.54 | 15.9 |
| 31X | 21 | 0800 | 279.3–288.5 | 9.2 | 8.83 | 96.0 |
| 32X | 21 | 0855 | 288.5–298.1 | 9.6 | 8.40 | 87.5 |
| 33X | 21 | 0955 | 298.1–307.8 | 9.7 | 9.01 | 92.9 |
| 34X | 21 | 1100 | 307.8–317.4 | 9.6 | 9.54 | 99.4 |
| 35X | 21 | 1250 | 317.4–318.4 | 1.0 | 0.74 | 74.0 |
| Coring totals | | | | 318.4 | 316.69 | 99.5 |

Table 2. Summary of logging operations at Site 851.

| Date (June 1991) | Time (L) | Cumulative hours | Base of string (mbsf) | Remarks |
|------------------|----------|------------------|-----------------------|---|
| 18 | 0820 | 0.0 | | Last core on deck. |
| 18 | 1015 | 1.9 | | Start rig up. |
| 18 | 1135 | 3.3 | | Geophys. tool rigged up (NGT/SDT/HLDT/DIT/TLT); RIH. |
| 18 | 1249 | 4.5 | 91.1 | Start downlog. |
| 18 | 1255 | 4.6 | 178.0 | Stop downlog; software glitch kills it. |
| 18 | 1302 | 4.7 | 323.1 | At TD, start main log up, no heave compensator. |
| 18 | 1357 | 5.6 | 83.8 | End main log; close calipers and drop for repeat section. |
| 18 | 1410 | 5.8 | 175.3 | Start repeat logging pass upward. |
| 18 | 1430 | 6.2 | 89.9 | Stop repeat logging pass; close calipers and POOH. |
| 18 | 1545 | 7.4 | | Geophys. tool string as wellhead. |
| 18 | 1710 | 8.8 | | RIH w/geochem. string (NGT/ACT/GST/TLT). |
| 18 | 1820 | 10.0 | 0.6 | Pause at mud line. |
| 18 | 1834 | 10.2 | 322.5 | At TD; no heave comp; payout about 15 ft extra cable; calibrate while moving up slowly. |
| 18 | 1836 | 10.3 | 321.9 | GST calibrated; start main log. |
| 18 | 2005 | 11.7 | 61.9 | GST loses calibration after entering pipe. Bad GST data to mud line. |
| 18 | 2022 | 12.0 | 0 | Stop main log; POOH. |
| 18 | 2135 | 13.2 | | Geochem. string at wellhead. |
| 18 | 2230 | 14.2 | | RIH w/FMS string (NGT/GPIT/FMS). |
| 18 | 2345 | 15.4 | 323.1 | At TD, start FMS repeat log; no heave compensator. |
| 19 | 0000 | 15.7 | 219.5 | End repeat section, drop to TD. |
| 19 | 0007 | 15.8 | 323.1 | At TD, start main log up. |
| 19 | 0041 | 16.3 | 68.6 | Stop main log, close calipers and POOH. |
| 19 | 0200 | 17.7 | | FMS string at wellhead. |
| 19 | 0230 | 18.2 | | Rigged down from logging. |

major influence on the spectral characteristics of the sediment. For example, the high-carbonate foraminifer nannofossil ooze in the upper 76.5 m has relatively low reflectance. Comparison of the reflectance spectra of nannofossil ooze from 49.68 mbsf with those of diatom ooze with nannofossils from 271.60 mbsf (Fig. 13) shows that the high-carbonate sediment has only slightly higher reflectance overall. The shape of the spectral patterns differs for the two lithologies; however, the nannofossil ooze has the highest reflectance in the short wavelengths, and the diatom ooze has the highest reflectance in the long wavelengths. Thus, ratios of

reflectance from different wavelengths may distinguish sediments having differing lithologic constituents.

The use of ratios to identify the presence of a lithologic constituent can be illustrated with examples from the top interval (0–5.65 mbsf) and the basal interval (304.3 mbsf–basement) of oxidized sediments (Fig. 14). The spectral patterns of these two lithologies containing iron and manganese oxides (see examples from 0.10 and 315.14 mbsf) suggest that the presence of oxides causes high reflectance in the long wavelengths (near-infrared [nIR]) relative to the short wavelengths (blue and green). The oxidized sediments of the basal interval also

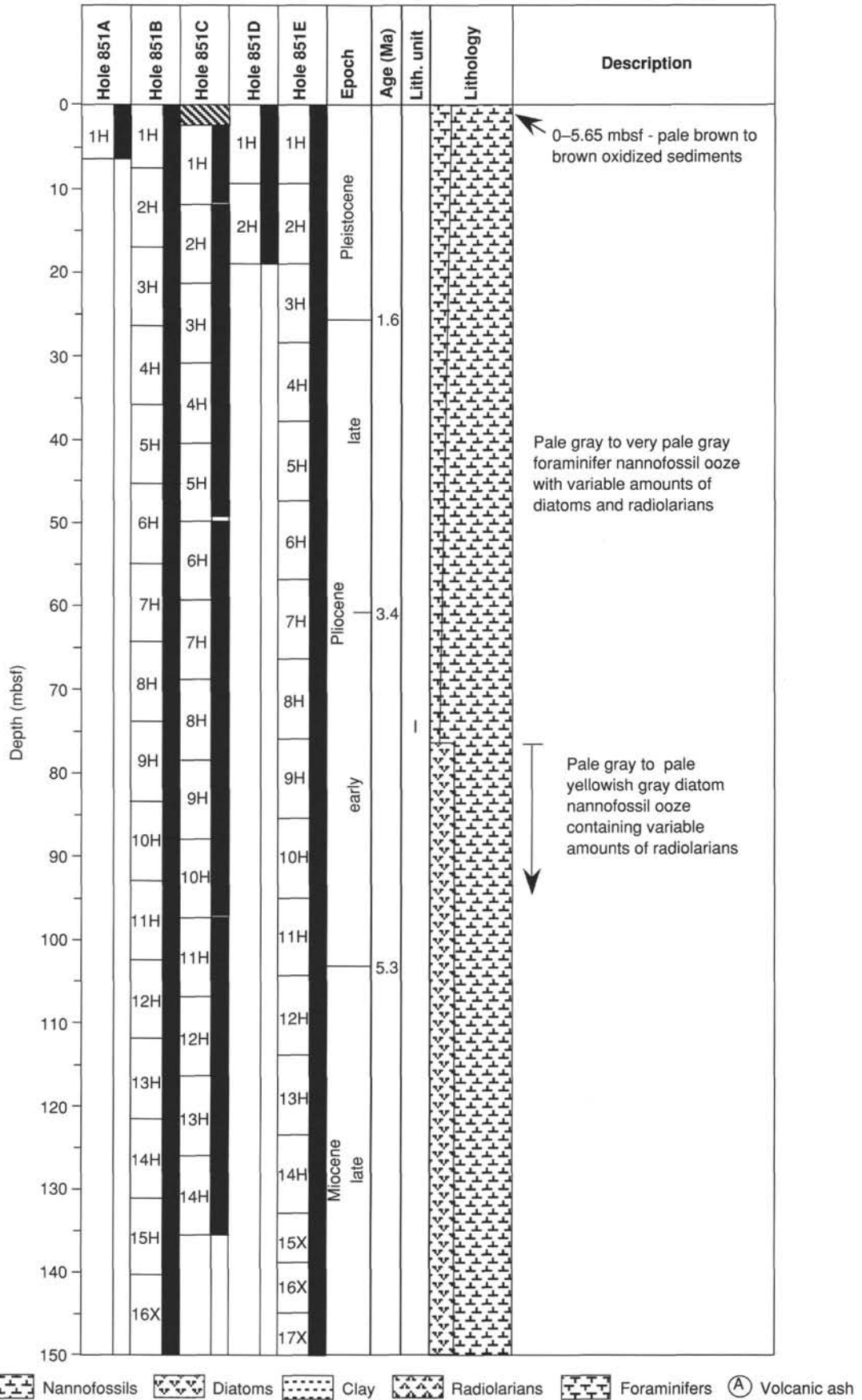


Figure 5. Lithologic summary at Site 851.

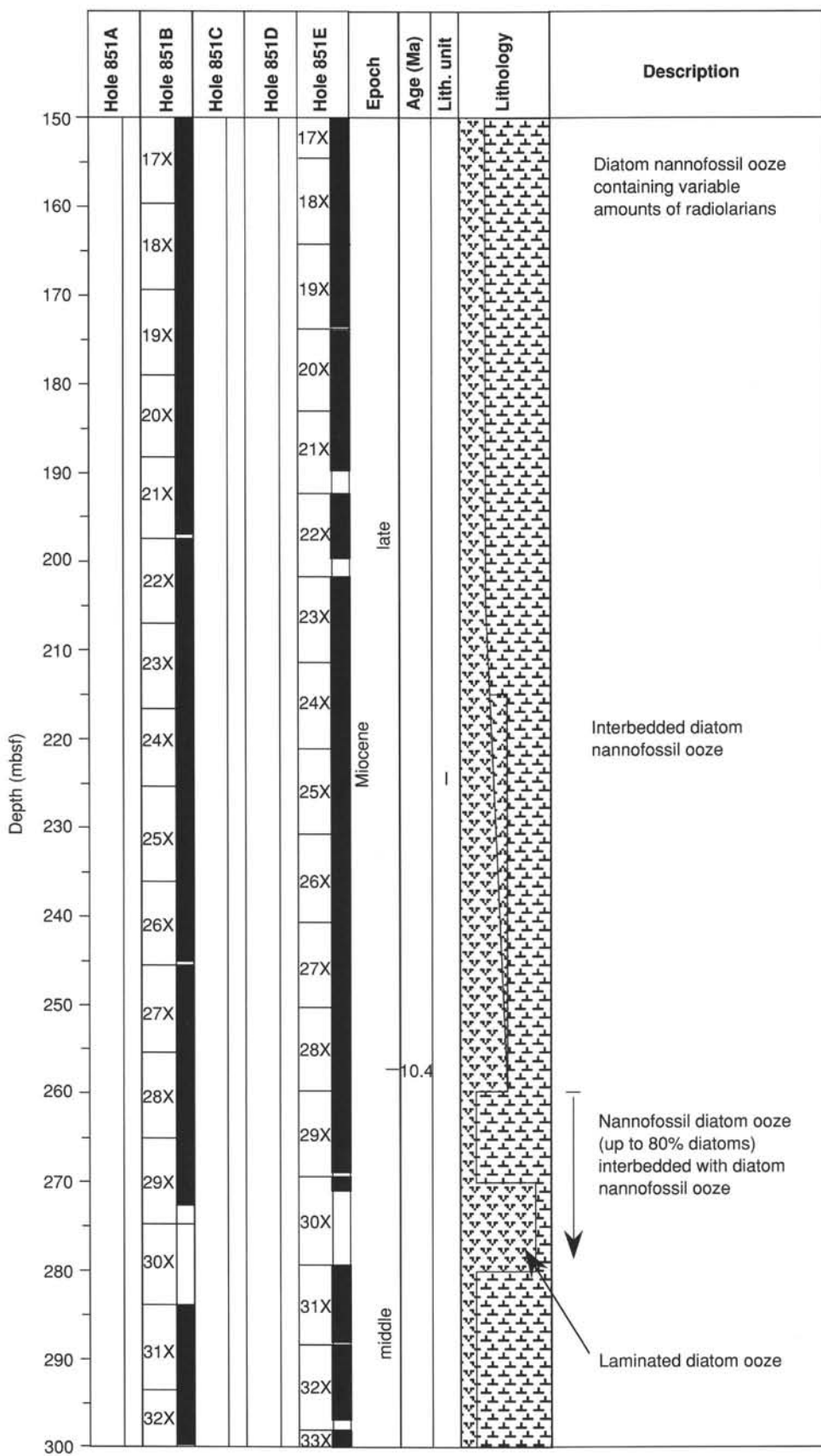


Figure 5 (continued).

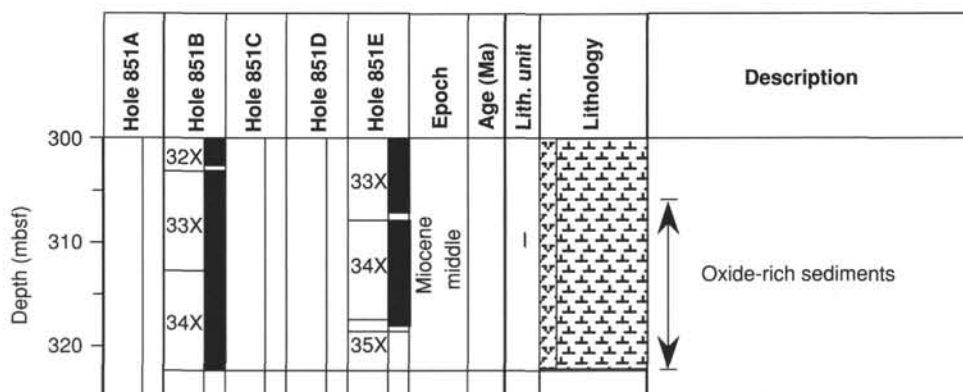


Figure 5 (continued).

have relatively high reflectance at 600 nm (yellow), possibly a result of the presence of an oxide or clay mineral not found in the upper interval. However, high nIR/red ratios are not unique to oxidized sediments, because they also characterize the interval of diatom ooze at approximately 275 mbsf.

Magnetic Susceptibility

Site 851 has two intervals of relatively high susceptibility (Fig. 6). The first coincides with the foraminifer nannofossil ooze (0–76.5 mbsf), and the second is within the interbedded diatom ooze and diatom nannofossil ooze interval (205.0–265 mbsf). Two intervals of relatively low susceptibility are coincident with the diatom nannofossil ooze (76.5–205.0 mbsf) and the nannofossil ooze/chalk with radiolarians and diatoms (287.0 mbsf–basement). No obvious correlations of susceptibility with the clay or the biogenic components of the sediment can be seen (Fig. 7). However, aluminum values (see “Downhole Measurements” section, this chapter) are slightly higher in sediments having high susceptibilities, suggesting that estimates of the percentage of clay from smear slides are unreliable in sediments having low clay content. Sedimentation rates (see “Sedimentation Rates” section, this chapter) are slightly higher in the low-susceptibility intervals, and slightly lower in the high-susceptibility intervals, suggesting that part of the susceptibility variation results from dilution of the clay component.

Organic carbon content also has highest values ($0.135 \pm 0.08\%$) in the interval of low magnetic susceptibility (between 76.5 and 205.0 mbsf) (see “Organic Geochemistry” section, this chapter). Uranium log values (see “Downhole Measurements” section, this chapter) are in agreement with measurements of organic carbon, with highest values in the interval between 76.5 and 205.0 mbsf. This suggests that reduction of iron-bearing phases is more intense in this interval of low susceptibility. Pyrite mottling and diagenetic banding occur most frequently in this interval.

Trace Fossils

Trace fossils are common to abundant throughout the sediments recovered at Site 851, except in the upper 30 m, where bioturbation is slight, and within intervals of laminated diatomaceous sediment, where bioturbation is absent. Open burrows are present as deep as 25 mbsf. Burrowing increases from 20 to 50 mbsf in more siliceous sediments. Within the foraminifer nannofossil ooze (0–80 mbsf), the overall light bioturbation is consistent with the common preservation of *Skolithos* (Fig. 15), which as a near-surface burrow would normally be destroyed with strong subsurface bioturbation. Bioturbation appears stronger within the more diatom-rich intervals, perhaps associated with higher concentrations of organic matter here. The concentrated decimeter-thick zones of diatom-rich burrow fills, common in

the diatom ooze between 80 and 185 mbsf, probably represent bioturbated original beds. The preservation of intervals of laminated sediment indicate recurring periods in which conditions were hostile to a burrowing benthos.

Between about 47 and 92 mbsf, greenish-gray, radiolarian-, clay- and diatom-rich interbeds and the immediately adjoining sediment are moderately to strongly bioturbated with abundant solid burrows and *Planolites*. The intervening foraminifer nannofossil ooze has only slight burrowing. *Skolithos* burrows are common adjacent to the darker beds, but not within them, while *Zoophycos* spreiten are scattered within darker beds. *Chondrites* are observed rarely within burrow fills. Pyritized burrows are common in only one interval, between 50 and 65 mbsf.

The diatom nannofossil ooze between about 76.5 and 185 mbsf is moderately to strongly bioturbated, except in the thin interval of diatom-poor nannofossil ooze between 150 and 160 mbsf. Solid burrows and *Planolites* are commonly concentrated in decimeter-thick zones that are darker than the enclosing, more nannofossil-rich lithology. The fill of these burrows is commonly rich in pyrite and diatoms and, between 140 and 155 mbsf, also in foraminifers. *Chondrites* is common, both within burrow fills and in the surrounding sediment. Bioturbation is also strong in the less diatom-rich interval between 185 and 210 mbsf and concentrated in the darker, more diatom-rich horizons.

In the diatom- and radiolarian-rich interval from 210 and 250 mbsf, burrowing is generally slight in the paler more nannofossil-rich sediment and stronger in the darker, diatom- and radiolarian-rich interbeds where it is frequently intense (Fig. 16). Solid burrows, *Planolites* and *Chondrites* occur, but *Zoophycos* was not observed.

In the interval between 252 and 280 mbsf, the intensity of burrowing is moderate, except within zones of laminated diatomaceous sediment, which appear to lack bioturbation (Fig. 11). Paler intervals of intermittently laminated, partly bioturbated, more nannofossil-rich sediments are interbedded with the laminated diatom ooze (Fig. 9). These laminated zones also are associated with other, highly bioturbated diatom-rich beds. Solid burrows, *Planolites*, and *Chondrites* are common within these zones. Within the interval from 280 to 305 mbsf, bioturbation is light to moderate and is concentrated in zones rich in burrows filled with light gray diatom-rich sediments.

Summary of Lithology

The sedimentary sequence of Site 851 can be divided into four dominant lithologies with different characteristics. The Pleistocene to lower Pliocene foraminifer nannofossil ooze (0–76.5 mbsf, Hole 851B; 0–86.9 mcd), has a high percentage of CaCO_3 , high water content, high susceptibility, and low GRAPE density values relative to the underlying sections. Lower Pliocene to upper Miocene diatom nannofossil ooze (76.5–205.0 mbsf, Hole 851B; 86.9–244.35 mcd) has a high percentage

of CaCO₃, low water content, low susceptibility, and high GRAPE density values. Both lithologies have interbedded diatom- and radiolarian-rich nannofossil oozes, which have been recorded as decimeter-scale low-amplitude variations by most lithologic parameters.

The upper Miocene to middle Miocene interbedded diatom ooze and diatom nannofossil ooze (205.0–287.0 mbsf, Hole 851B; 244.35–345.4 mcd) has the most variable lithology of the sequence because of large changes in the ratio of diatoms to nannofossils. These sediments are distinguished by lower and more variable GRAPE density, high susceptibility, low reflectance and high water content values. Several intervals of laminated diatom ooze are present. The thickest interval (2 m) occurs just above chert, at 272.8 mbsf. Logging data (resistivity, FMS, density) suggest that this chert layer is 1 to 2 cm thick, that another discontinuous chert layer occurs a few centimeters below, and that the laminated diatom ooze interval continues 2 m below the chert.

The middle Miocene nannofossil ooze and chalk with diatoms and radiolarians (287.0–basement, Hole 851B; 345.4–387.04 mcd) have low susceptibility, high GRAPE density, high reflectance (particularly in the basal interval of oxidized sediments), low water content, and high velocity values. The basal sediments contain laminated clay-, oxide-, and nannofossil-rich sediments and possible sedimentological evidence for reworking.

BIOSTRATIGRAPHY

The sedimentary sequence recovered from the five holes cored at Site 851 consists of a nearly 320-m-thick continuous record from the upper Pleistocene through the uppermost middle Miocene. A well-constrained biostratigraphy has been provided by both calcareous and siliceous microfossils (Tables 3 through 6; Fig. 17). Calcareous nannofossils are abundant and well preserved throughout the sequence. Planktonic foraminifers are abundant, but poorly to moderately well preserved in the Pleistocene and the Pliocene. These are few to common, but poorly preserved in the Miocene, and are rare or absent in some intervals especially rich in siliceous microfossils. In the deepest sediments, planktonic foraminifers are common to abundant and have been partly recrystallized. Radiolarians are common to abundant and moderately well to well preserved throughout the section, down to a level slightly above the basement. The deepest sediments, however, are barren of radiolarians. Diatoms are rare to abundant throughout the sequence. Their preservation is moderate to good in the Pleistocene through the upper Miocene interval and poor in the middle Miocene interval.

The epoch boundaries are best approximated as follows:

| Boundary | Hole | Depth (mbsf) | Depth (mcd) | Event |
|--------------------------|------|--------------|---------------|--|
| Pliocene/ Pleistocene | 851B | 27.10–26.69 | 31.25–31.09 | B <i>Gephyrocapsa oceanica</i> s.l. |
| late/early Pliocene | 851B | 62.75–63.10 | 71.2–71.5 | T <i>Reticulofenestra pseudumbilicus</i> |
| Miocene/ Pliocene | 851B | 103.01–102.8 | 116.16–117.80 | T <i>Discoaster quinqueramus</i> |
| late/middle Miocene | 851B | 258.9–259.3 | 314.8–315.30 | T <i>Coccolithus miopelagicus</i> |

The stratigraphically lowest sample (138-851B-34X-CC) was placed in calcareous nannofossil Subzone CN5b and in foraminiferal Zone N14, allowing us to assign an age of 11.1–11.3 Ma for the sediments just above the basement.

Calcareous Nannofossils

Calcareous nannofossils recovered at Site 851 represent a stratigraphic succession from the upper Pleistocene (Zone CN14b from Okada

and Bukry [1980] and NN20 from Martini [1971]) through the upper middle Miocene (Zones CN5b and NN7; Fig. 17). Nannofossils are abundant and generally well preserved throughout the entire sequence and provide a detailed and well-constrained biostratigraphy. Discoasterids are common or abundant in the Pliocene and uppermost Miocene intervals (Cores 138-851B-4H through -28X) and rare and overgrown in the upper middle Miocene interval (Cores 138-851B-29X through -34X). Etching on placoliths was observed in some samples from the upper Miocene interval (Cores 138-851B-25X through -28X). Common reworked nannofossils from the upper Miocene Zone CN9 and middle Miocene Zones CN6 and CN5b are present in the Pliocene interval from Cores 138-851B-6H through -8H. The nannofossil events recognized at Site 851 are reported in Table 3.

In the Pleistocene interval (Cores 138-851B-1H through -3H), the assemblage is characterized by helicolithids, *Pseudoemiliania lacunosa*, *Calcidiscus* spp., and different morphotypes of *Gephyrocapsa* spp. The first occurrence of *Gephyrocapsa oceanica* s.l. approximates the Pleistocene/Pliocene boundary and was recorded between Samples 138-851B-3H-CC and -4H-1, 19 cm, and Samples 138-851C-3H-3, 70 cm, and -3H-3, 140 cm.

The Pliocene interval (Cores 138-851B-4H through -11H) is characterized by rich and well-preserved assemblages, with common to abundant *Reticulofenestra* spp., *Calcidiscus* spp., *Coccolithus pelagicus*, discoasterids, helicoliths, ceratolithids, and sphenolithids in the lower Pliocene interval. The last occurrence of *Reticulofenestra pseudumbilicus*, which approximates the upper Pliocene/lower Pliocene boundary, was recorded between Samples 138-851B-7H-6, 25 cm, and -7H-6, 60 cm.

The last occurrence of *Discoaster quinqueramus*, which approximates the Pliocene/Miocene boundary, was recorded between Samples 138-851B-11H-7, 30 cm, and -12H-1, 30 cm. Through all their stratigraphic range (Samples 138-851B-11H-CC to -20X-CC, corresponding to Zones CN9/NN11), *D. quinqueramus* and *Discoaster berggreni* are common and characterize the uppermost Miocene assemblage. The first occurrence of *Amaurolithus primus* is recorded between Samples 138-851B-18X-CC and -19X-1, 25 cm, and Samples 138-851E-19X-4, 25 cm, and -19X-4, 60 cm.

The total range of *Discoaster hamatus* (Zones CN7 and NN9) corresponds to the stratigraphic interval from Samples 138-851B-25X-1, 60 cm, through -28X-3, 40 cm. In this interval, rare specimens of *Catinaster coalitus* and *Catinaster calyculus* were observed. *Catinaster coalitus* is rare and scattered in the interval below the first occurrence of *D. hamatus* (between Samples 138-851B-28X-3, 40 cm, and -28X-3, 80 cm). Thus, its first occurrence, which corresponds to the base of Zone CN6 (NN8), was difficult to define and was tentatively placed between Samples 138-851B-29X-5, 71 cm, and -29X-CC. The last occurrence of *Coccolithus miopelagicus*, which approximates the upper/middle Miocene boundary, was recorded between Samples 138-851B-28X-3, 40 cm, and -28X-3, 80 cm.

The lowermost part of the Site 851 sequence (Cores 138-851B-32X through -34X) was placed in the upper middle Miocene Subzone CN5b (Zone NN7). Common specimens of *Discoaster kugleri* are recorded in the interval from Core 138-851B-32X through the bottom of the stratigraphic sequence.

Planktonic Foraminifers

Planktonic foraminifers are abundant and poorly to moderately well preserved from Cores 138-851B-1H through -10H, with a high degree of fragmentation. Below Core 138-851B-10H, preservation is poor throughout the sequence. Planktonic foraminifers are few to common from Cores 138-851B-11H through -30H and are rare (Sample 138-851B-12H-CC) or absent (Samples 138-851B-25X-CC and -27X-CC) in those intervals especially rich in siliceous microfossils. In the lowest part of the sequence (Samples 138-851B-32X-CC through -34X-CC), planktonic foraminifers are common to abundant, with a partly recrystallized fauna.

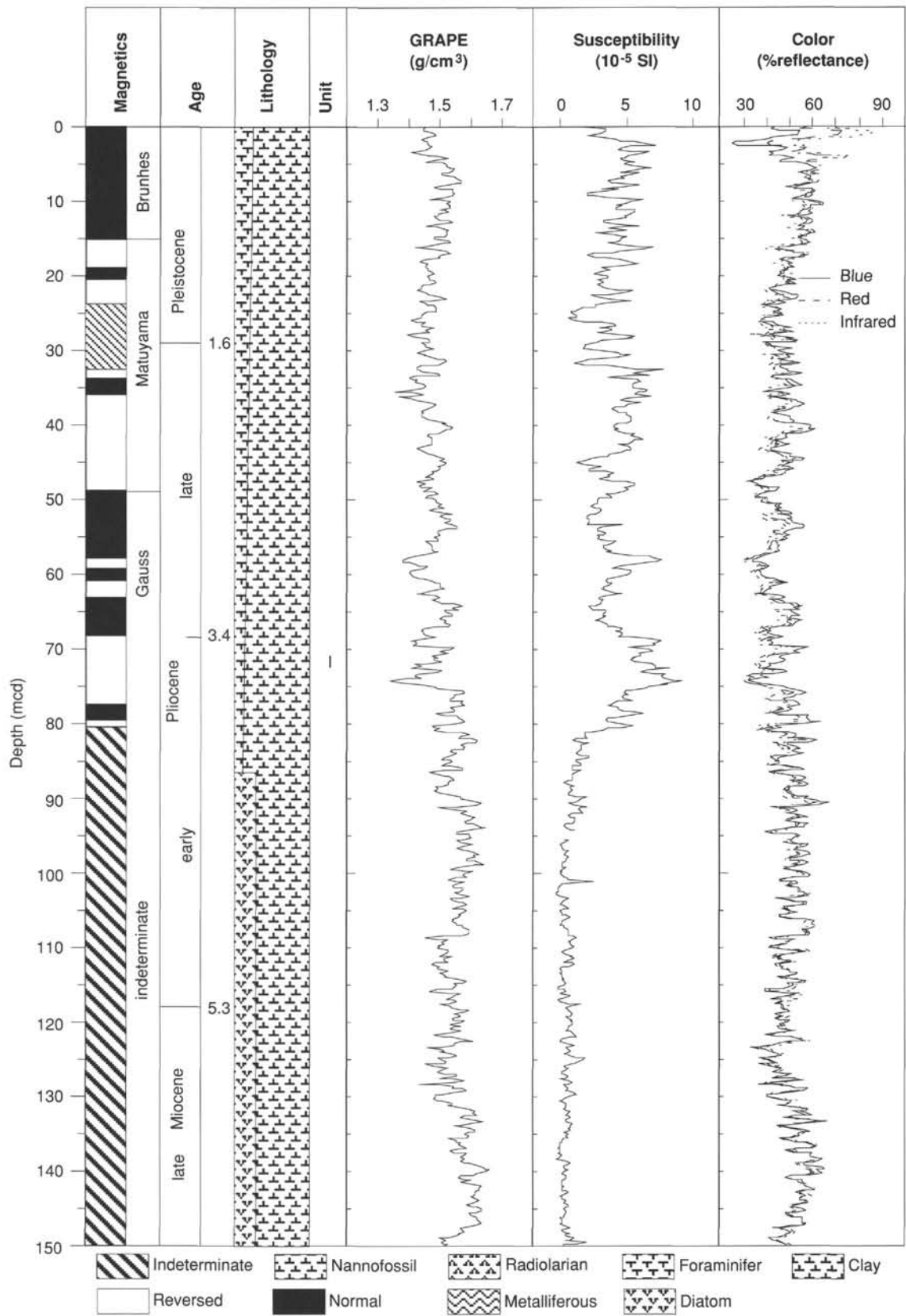


Figure 6. Composite summary of magnetics, age, graphic lithology, GRAPE density, magnetic susceptibility, and color reflectance for Site 851. The composite data consist of sections spliced together from the multiple holes drilled at the site. Data are shown plotted vs. meters composite depth (mcd), the new depth scale used when composite sections are constructed. The GRAPE density, susceptibility, and color data have been smoothed using a 20-point Gaussian filter.

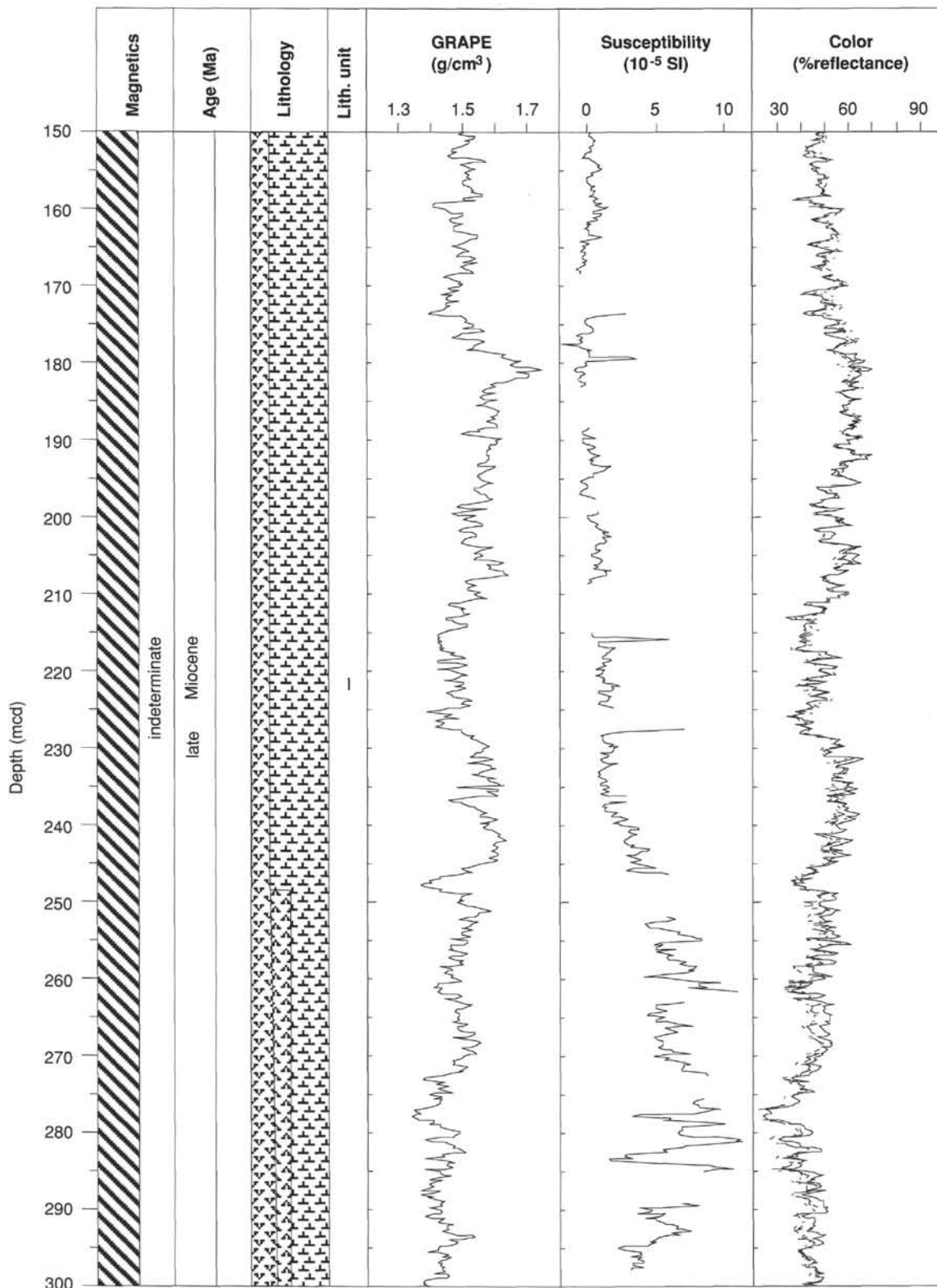


Figure 6 (continued).

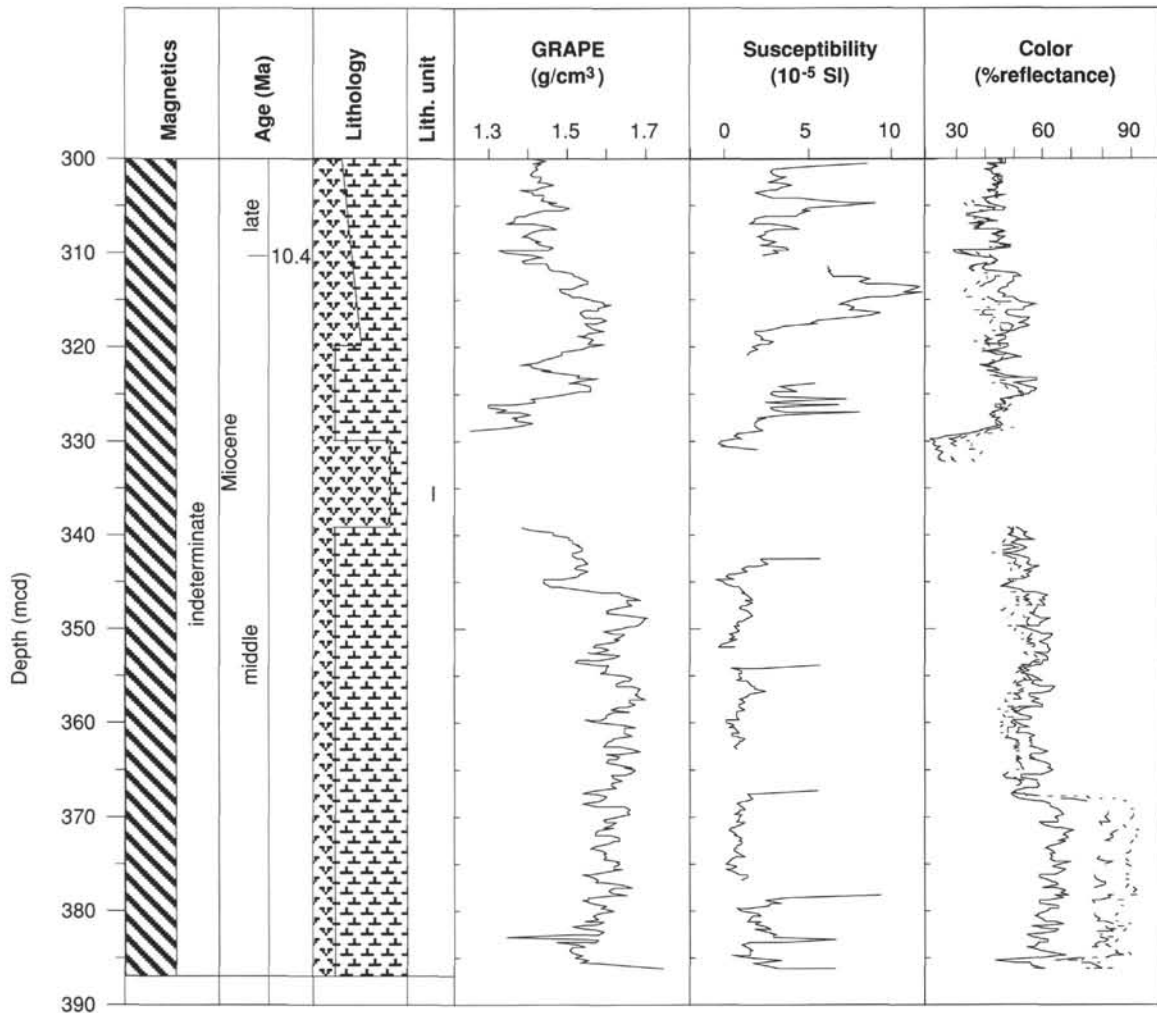


Figure 6 (continued).

The dominant components of the coarse fraction residues are foraminifers in Cores 138-851B-1H through -10H and radiolarians in Cores 138-851B-11H through -32X. Throughout the interval between Cores 138-851B-11H through -32X, other major coarse fraction components include rare to few echinoid spines, sponge spicules, and fish teeth. Pyrite is rare to few in a few samples (138-851B-7H-CC, -13H-CC, -31X-CC, and -32X-CC) and common in Sample 138-851B-14X-CC. In the lowest two samples (138-851B-33X-CC and -34X-CC), volcanic glass is abundant, and manganese micronodules are common.

Planktonic foraminiferal datums identified in the sequence are given in Table 4. The base of Pleistocene Zone N22 has been equated to the last occurrences of *Globigerinoides fistulosus* and *Globorotalia limbata* in Sample 138-851B-4H-CC and the base of upper Pliocene Zone N21 to the last occurrence of *Sphaeroidinellopsis* in Sample 138-851B-7H-CC. The base of lower Pliocene Zone N18 was placed in Sample 138-851B-10H-CC at the first occurrence of *Globorotalia tumida*. The interval from Sample 138-851B-11H-CC through -28X-CC was assigned to Zone N17 on the basis of the occurrence of the nominate taxon, *Globorotalia plesiotumida*. However, throughout this interval, the morphotypes referable to this species are rare and scattered. Furthermore, a taxonomic ambiguity exists between *G. plesiotumida* and the more common *G. limbata*, both of which change coiling direction simultaneously at several levels. As a result, the position of the base of Zone N17 remains tenuous here. Rare *Neogloboquadrina acostaensis* (whose first occurrence defines the base of Zone N16) and *Globorotalia siakensis* (whose last occurrence defines the base of Zone N15) co-occur in Sample 138-851B-31X-CC,

which precluded our identifying Zone N15. The lowest part of the sequence from Cores 138-851B-32X-CC through -34X-CC was assigned to Zone N14, based on the presence of *G. siakensis*.

Radiolarians

Radiolarians sampled at Site 851 range in age from the Quaternary (*Collosphaera tuberosa* Zone) to the late middle Miocene (*Diatrus pettersoni* Zone). The most recent radiolarian zone (*Buccinosphaera invaginata*) was not identified. The oldest material recovered that could be identified to the zonal level (*D. pettersoni* Zone) is from Sample 138-851B-34X-4, 109 cm.

Preservation and abundance of the radiolarians are moderately good within the Pleistocene-Pliocene section. Only a trace of reworking of older radiolarians is found into the upper Pliocene part of the section in Sample 138-851B-8H-4, 110 cm. The Pleistocene-Pliocene section appears to be complete, with all the major zones and radiolarian datums recognized in the samples studied. Occurrences of *Spongaster pentas* and *Spongaster berminghamsi* were scattered at this site, which made it impossible for us to use the first and last occurrences of these species for correlation with other sites. The occurrence of *Acrobotrys tritubus* is also scattered, and its first and last appearances could not be used as reliable datums in any of the sites studied.

Radiolarians are common to abundant throughout the upper to upper middle Miocene part of the section, and preservation is generally good. Below Core 138-851B-24X, preservation decreases some-

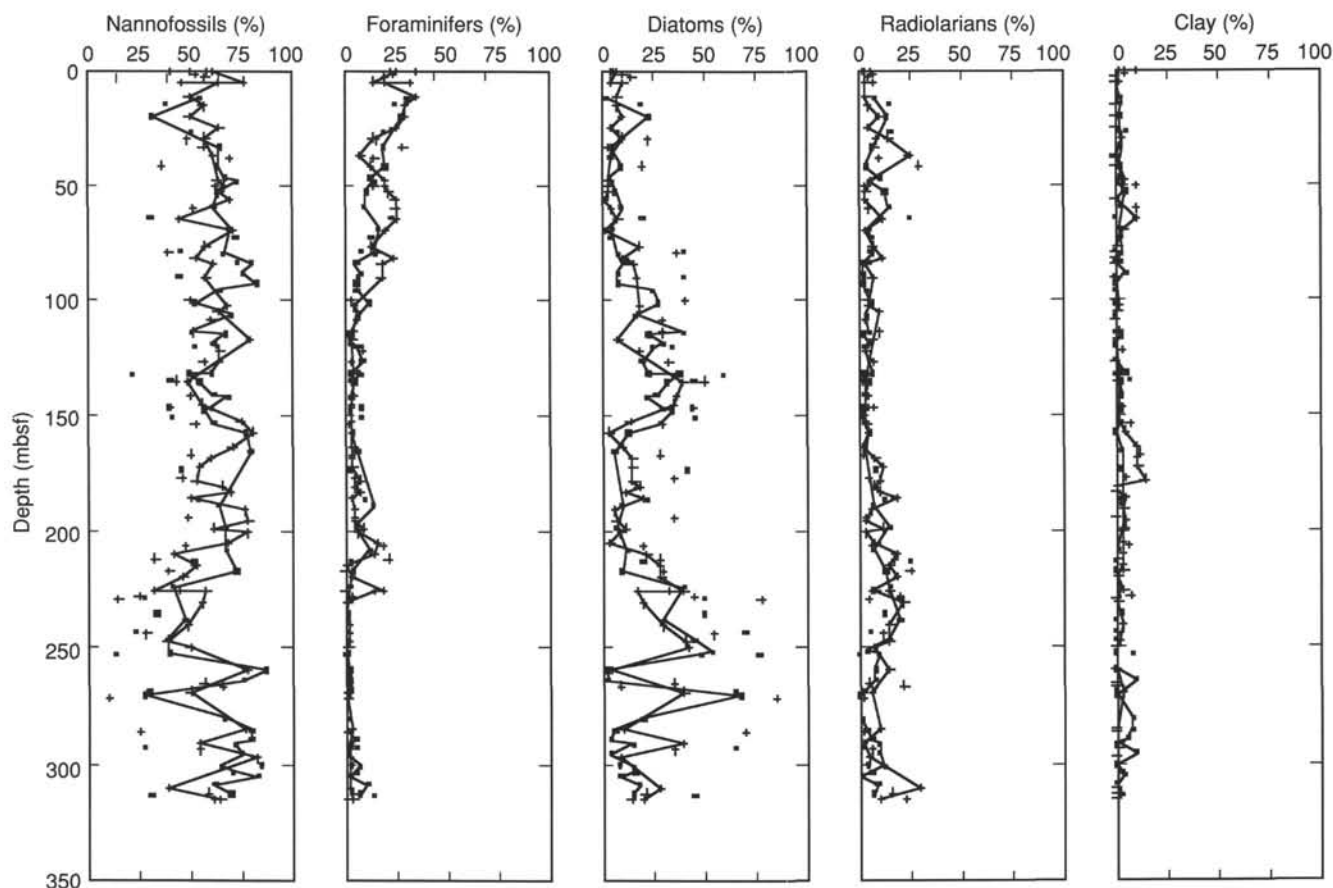


Figure 7. Smear slide data for Holes 851A and 851B (crosses) and Hole 851E (squares). Major lithologies (curves) have been separated from minor lithologies (points).

what, but remains either good or moderately good down to the lowermost part of Core 138-851B-34X. The core-catcher sample of this deepest recovered core, however, was barren of radiolarians. The oldest reliable datum (Table 5) is the last appearance of *Carpocanium cristata* (between Samples 138-851B-28X-CC and -29X-1, 110 cm). This datum occurs within the middle part of the *Diartus pettersoni* Zone and has an age of $10 (\pm 0.1)$ Ma within the tropical Indian and Pacific oceans (Johnson and Nigrini, 1985).

Diatoms

Generally, diatoms are present in the Quaternary (*Pseudoenotia doliolus* Zone) through upper middle Miocene (*Crasedodiscus coscinodiscus* Zone) sediments recovered from Site 851. Diatom preservation varies from sample to sample, with diatoms exhibiting moderate to good preservation in the Quaternary through upper Miocene interval, moderate preservation in the lower upper Miocene, and poor preservation in the upper middle Miocene. Rare to abundant diatoms occur throughout the stratigraphic sequence.

The diatom assemblage at Site 851 is somewhat similar to that observed at Site 850. Characteristic species include *Azpeitia nodulifer*, *Denticulopsis hustedtii*, *Hemidiscus cuneiformis*, *Nitzschia cylindrica*, *Nitzschia fossilis*, *Nitzschia jouseae*, *Nitzschia miocenica*, *Nitzschia reinholdii*, *Pseudoenotia doliolus*, *Rhizosolenia praebergonii*, *Thalassionema nitzschioides*, *T. nitzschioides* var. *parva*, *Thalassiosira convexa*, *Thalassiosira miocenica*, *Thalassiosira praeconvexa*, *Thalassiosira yabei*, and *Thalassiothrix longissima*. The diatom assemblage is dominated in specific intervals by specimens of either *A. nodulifer*, *Thalassiothrix longissima*, *Thalassionema nitzschioides*, and *Hemidiscus cuneiformis*, or *Denticulopsis hustedtii*.

Five holes were cored at Site 851. Hole 851A consists of one mud-line core representing the *P. doliolus* Zone. Holes 851B and 851E extend from the *P. doliolus* Zone to the *C. coscinodiscus* Zone. Hole 851C represents the *P. doliolus* through the upper portion of the *T. convexa* Zone, while Hole 851D consists of two cores dedicated for paleomagnetic analysis and that represents the *P. doliolus* and Subzone B of the *N. reinholdii* Zone.

The following discussion focuses on the stratigraphic results obtained from Holes 851B, 851C, and 851E. Cores 138-851B-1H, -851C-1H, and -851E-1H were assigned to the *P. doliolus* Zone, based on the occurrence of *P. doliolus* stratigraphically above the last occurrence of *N. reinholdii*. The last occurrence of *N. reinholdii* was placed in Samples 138-851B-2H-CC; -851C-1H-CC; and -851E-2H-1, 80 cm, which allowed us to place the *P. doliolus*/*N. reinholdii* boundary between Samples 138-851B-1H-CC and -2H-CC; -851C-1H-CC and -2H-CC; and -851E-1H-CC and -2H-1, 80 cm.

Samples 138-851B-2H-CC through -4H-1, 90 cm; -851C-2H-CC and -3H-CC; and -851E-2H-1, 80 cm, through -3H-CC were placed in the *N. reinholdii* Zone. The Subzone B/Subzone A boundary (the last occurrence of *Rhizosolenia praebergonii*) was placed in the interval between Samples 138-851B-3H-CC and -4H-1, 90 cm; -851C-2H-C and -3H-CC; and -851E-2H-CC and -3H-CC.

The intervals from Samples 138-851B-4H-3, 60 cm, through -6H-3, 1 cm; -851C-4H-CC through -6H-2, 90 cm; and -851E-5H-4, 90 cm, through -5H-CC were placed in the *R. praebergonii* Zone. This zone was divided into three subzones on the basis of the occurrences of *T. convexa* and *N. jouseae*. Samples 138-851B-4H-3, 60 cm, through -5H-1, 75 cm, and Sample -851E-5H-CC were assigned to Subzone C; Samples 138-851B-5H-3, 75 cm, and -5H-CC; -851C-5H-2, 90 cm; and -851E-5H-4, 90 cm, were assigned to Subzone B;

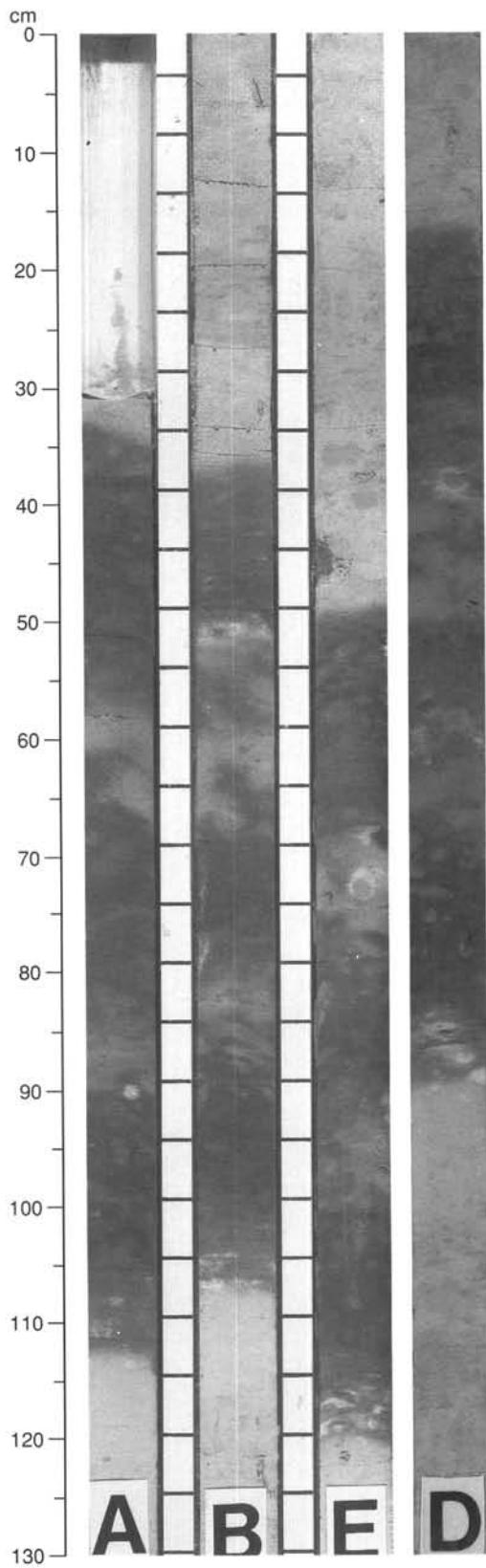


Figure 8. Section 2 from Core 1H of Holes 851A, 851B, 851E, and Section 1 from Core 1H of Hole 851D showing correlated color bands.

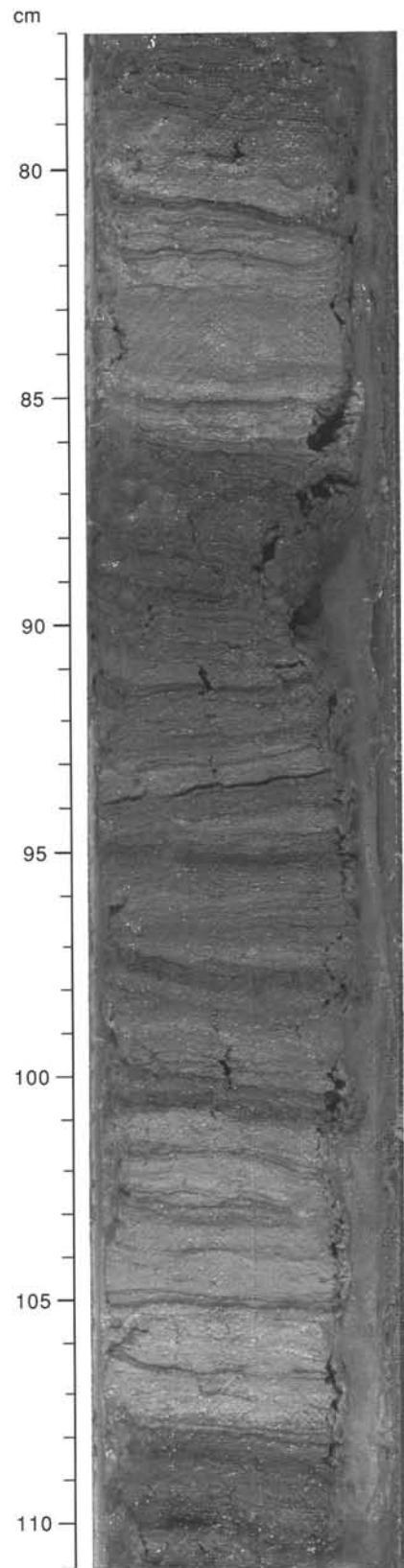


Figure 9. Alternating intervals of laminated, darker diatom ooze with intermittently laminated, more nannofossil-rich sediments. Slight bioturbation is visible in the upper lighter interval (interval 138-851E-28X-2, 77-111 cm).

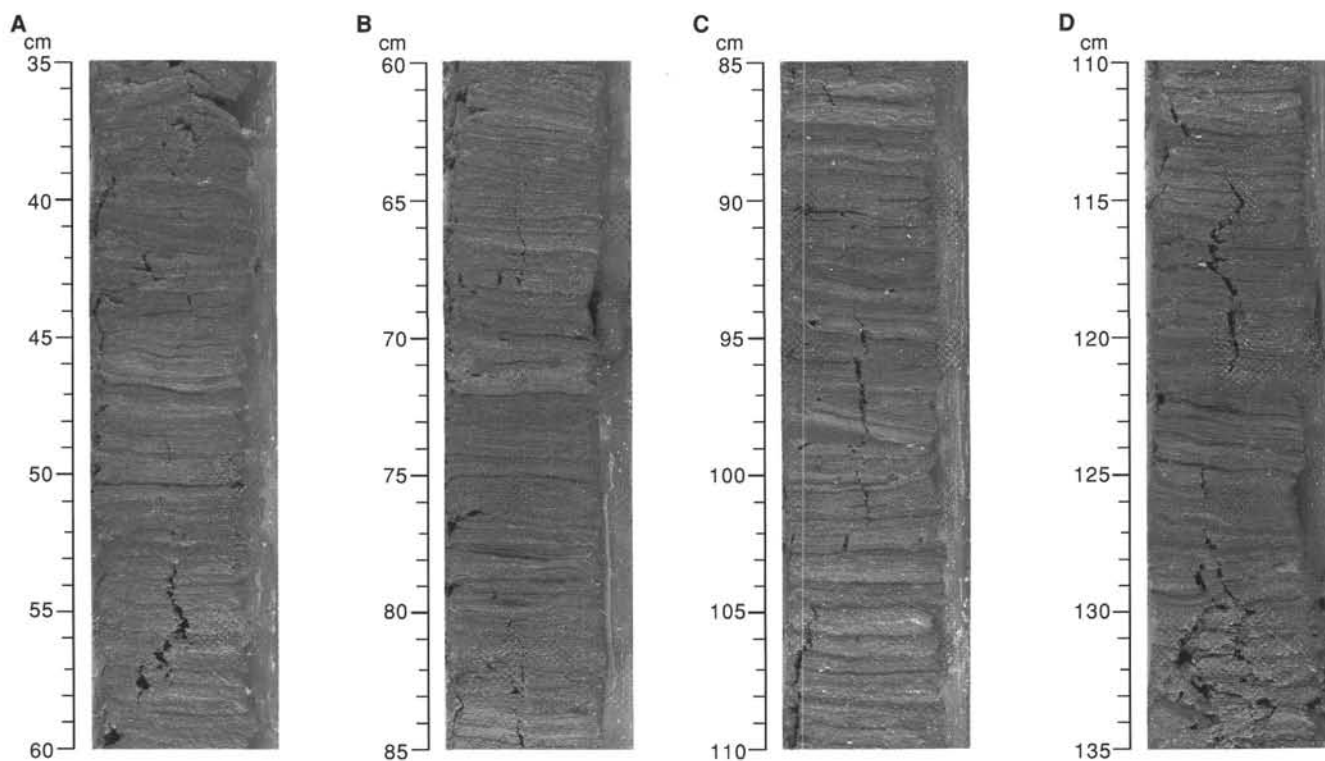


Figure 10. Composite figure showing the longest recovered interval of millimeter-scale banding and lamination (interval 138-851B-29X-5, 35–135 cm).

and Samples 138-851B-6H-3, 1 cm; -851C-5H-CC and 6H-2, 90 cm; and -851E-5H-6, 90 cm, and -5H-CC were placed in Subzone A.

The *N. jouseae* Zone was defined as the stratigraphic interval from the first occurrence of *R. praebergonii* to the first occurrence of *N. jouseae*. Samples 138-851B-6H-5, 1 cm, through -9H-CC; -851C-6H-5, 1 cm, through -8H-CC; and -851E-6H-CC through -851E-9H-4, 63 cm, were assigned to this zone. Stratigraphic events observed in this interval include the first occurrence of *T. convexa* var. *convexa* (Samples 138-851B-7H-5, 1 cm, to -7H-6, 1 cm, and -851E-7H-4, 100 cm, to 7H-5, 78 cm) and the last occurrence of *N. cylindrica* (Samples 138-851E-9H-2, 90 cm, through -9H-4, 63 cm).

Samples 138-851B-10X-CC through -15H-CC; -851C-9H-CC through -14H-CC (base of Hole 851C); and -851E-9H-5, 141 cm, through -15H-CC represent the *T. convexa* Zone. This interval was divided into three subzones as follows: Subzone C (Samples 138-851B-10H-CC through -11H-CC; -851C-9H-CC through -10H-CC; and -851E-9H-5, 141 cm, through -10H-CC); Subzone B (Samples 138-851B-12H-CC to -15H-2, 90 cm), and Subzone A (Samples 138-851B-15H-6, 20 cm through 15H-CC).

The *N. miocenica* Zone represents the interval from the first occurrence of *T. miocenica* and *T. convexa* to the first occurrence of *N. miocenica*. This zone was subdivided into two subzones on the basis of the first occurrence of *T. praeconvexa*. Sample 138-851B-16X-CC was assigned to Subzone B, and Samples 138-851B-17X-CC through -18X-CC and -851E-15X through -17X-CC were placed in Subzone A. Subzone B was not recognized in Hole 851B. The *Nitzschia miocenica*/*Nitzschia porteri* zonal boundary was placed in the interval between Samples 138-851B-18X-CC and -19X-CC and Samples 138-851E-17H-CC and -18X-CC.

The occurrence of *N. porteri*, *N. cylindrica*, and *R. paleacea* below the first occurrence of *N. miocenica* and above the last occur-

rence of the *T. yabei* Group allowed us to assign Samples 138-851B-19X-CC through -21X-CC and -851E-18X-CC through 851E-21X-CC to the *N. porteri* Zone. The occurrence of *Thalassiosira burckliana* in Sample 138-851B-21X allowed us to place the Subzone A/Subzone B boundary tentatively between Samples 138-851E-20X and -21X-CC.

Samples 138-851B-22X-CC through -25-1, 80 cm, and -851E-22X-CC through -24X-CC were placed in the *T. yabei* Zone. This zonal placement was based on the occurrence of *T. yabei* above the last occurrence of *Denticulopsis hustedtii*. *Thalassiosira burckliana* occurs in the uppermost portion of this interval (Samples 138-851B-22X-CC), indicating that this interval is equivalent to Subzone B of the *T. yabei* Zone. The exact placement of the Subzone B/Subzone A boundary cannot at present be determined.

The *Thalassiosira yabei*/*Actinocyclus moronensis* zonal boundary has been defined by the last occurrence of *A. moronensis*. However, *A. moronensis* has a scattered occurrence at Site 851. Therefore, the boundary was tentatively placed at the last occurrence of *Denticulopsis hustedtii* in Samples 138-851B-25X-2, 80 cm, and between Samples 138-851E-25X-CC and -31X-CC. The uppermost stratigraphic occurrence of *A. moronensis* is seen in Sample 138-851B-25X-2, 80 cm.

The remaining interval (Core 138-851E-32X through -34X) was assigned to the *Craspedodiscus coscinodiscus* Zone, which has an estimated age between 10.6 and 11.8 Ma.

PALEOMAGNETISM

Laboratory Procedures

The paleomagnetic measurements at Site 851 consisted primarily of remanence measurements with the pass-through magnetometer, following the procedures outlined in the "Explanatory Notes" chap-

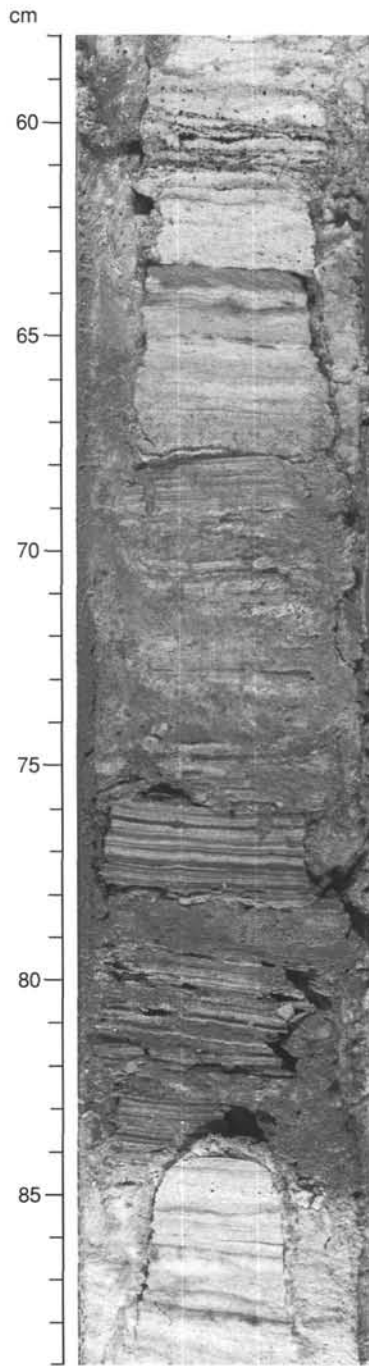


Figure 11. Laminations of clay-, nannofossil-, and oxide-rich sediments from the basal oxidized section just above basement (interval 138-851B-34X-5, 58–89 cm).

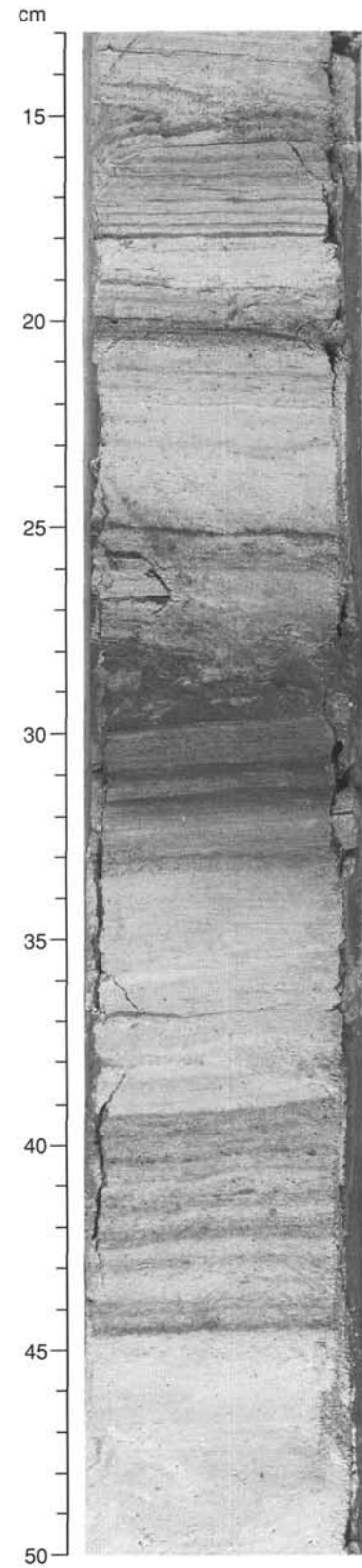


Figure 12. Oxidized section just above basement (interval 138-851B-34X-6, 13–50 cm) showing laminations and evidence for sediment reworking.

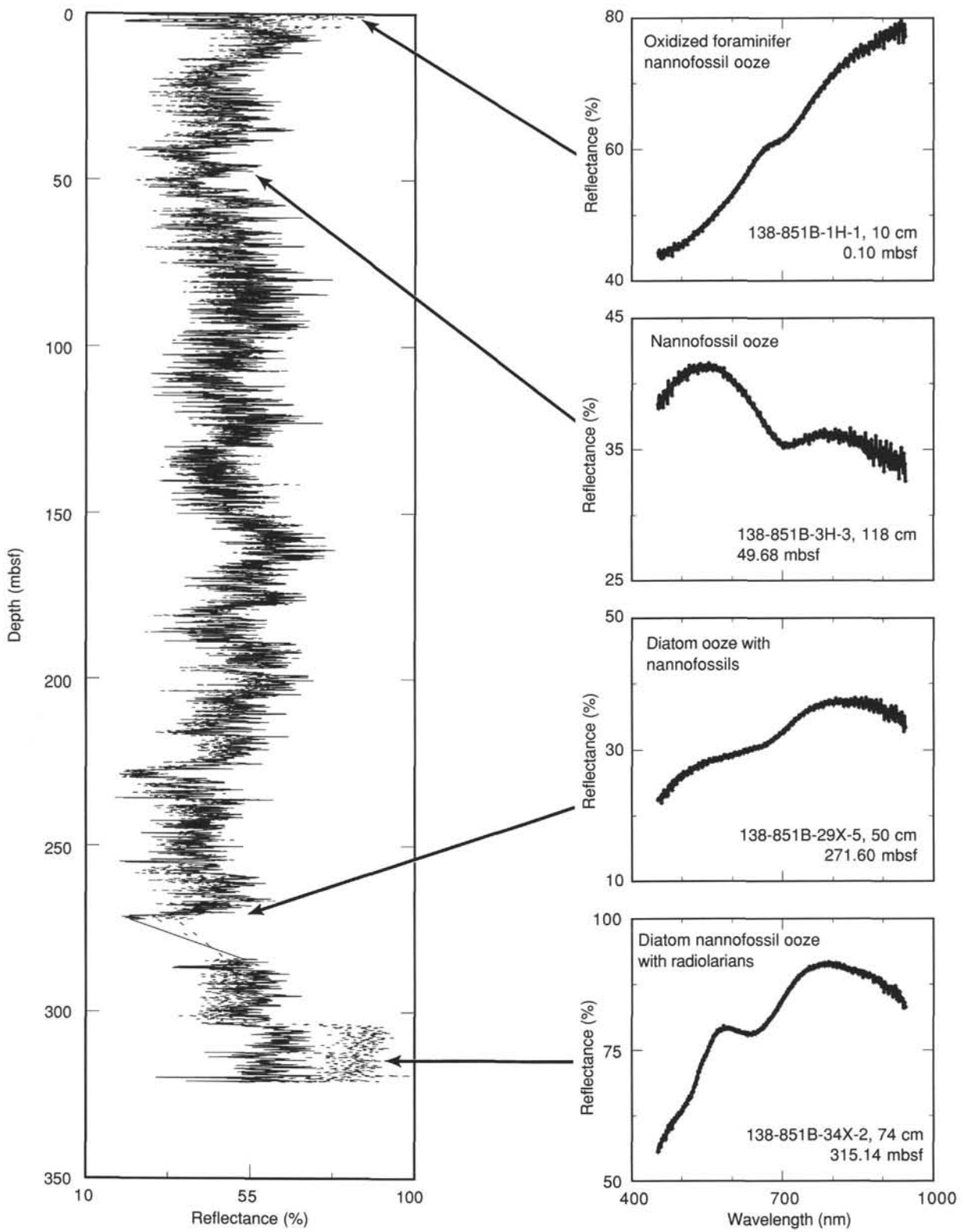


Figure 13. Percentage of blue (solid line), red (dashed line), and near-infrared (dotted line) reflectance for Site 851B, with spectral patterns for four different lithologies.

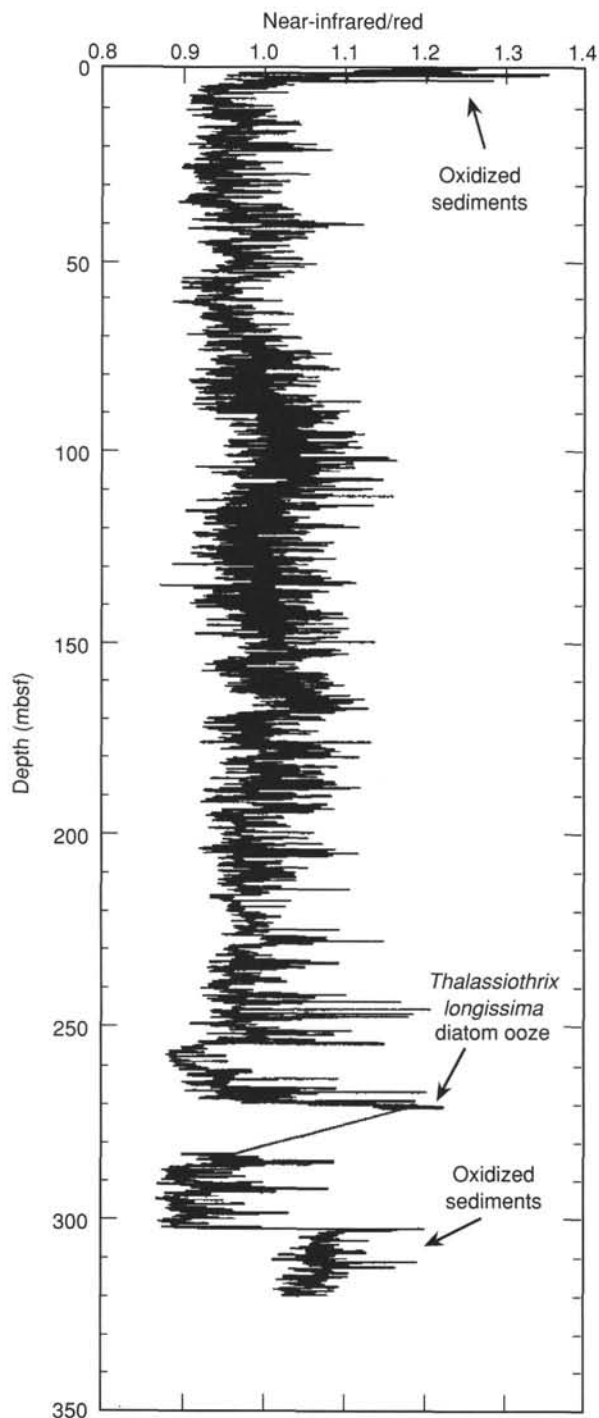


Figure 14. Near-infrared/red reflectance vs. depth in Hole 851B.

ter (this volume). In Hole 851A (one core, four sections), we measured the natural remanent magnetization (NRM) and demagnetized the remanence to peak alternating fields (AF) of 10 and 15 mT to determine the preferred demagnetization level for obtaining the stable directions. Based on these results, AF “cleaning” at 15 mT was chosen for blanket demagnetizations at Site 851, because it successfully removed the secondary overprints. Subsequently, all Site 851 cores studied for paleomagnetism were “cleaned” at 15 mT AF in the pass-through cryogenic magnetometer. In addition, in Holes 851B and 851C, NRMs were measured for most sections. NRMs were not

measured for Hole 851E. In Hole 851B, we measured all 15 APC cores. However, in Holes 851C and 851E, only the top eight APC cores were measured, because the deeper sediments did not lend themselves to shipboard paleomagnetic analysis. Discrete samples were taken from Cores 138-851B-8H through -14H for a shore-based pilot study.

Hole 851D, which comprises two APC cores at the top of the section, was intended primarily for high-resolution (“U channel”) shore-based paleomagnetic sampling. The cores from Hole 851D were subjected to GRAPE measurements, were split, described, and then their color reflectance was scanned. However, no shipboard susceptibility or remanence measurements were performed for Hole 851D. These measurements will be performed at the Scripps Institution of Oceanography paleomagnetic laboratory. As at the other Leg 138 sites, susceptibilities were routinely measured in unsplit core sections using the multisensor track (MST). To speed the laboratory core flow at Site 851, susceptibilities were not measured for Cores 138-851E-1H-1 to -17X-1, nor for Cores 138-851E-17X-3 to -19X-1. In addition, at Hole 851C, susceptibilities in Cores 138-851C-5H and -6H were measured in split archive-half sections. The raw susceptibility data archived for these two cores thus should be multiplied by 1.26×10^{-5} , rather than 0.63×10^{-5} (as indicated in the “Explanatory Notes” chapter, this volume, to give a correct SI volume normalization).

Results and Discussion

Shipboard paleomagnetic results for Site 851 have been confined to the top 80 mcd (~70 mbsf), where the magnetic signal usually was readily resolvable. Except for several short low magnetization/low susceptibility zones between 23 and 32 mcd (between the Jaramillo and Olduvai), this interval has a stable characteristic remanence, which was revealed by the 15-mT AF demagnetization. At the base of this interval, a distinct boundary that shows a sharp downhole decrease in magnetization intensity and susceptibility was observed (Fig. 18). Below this horizon, magnetization intensity decreases to 0.1-mA/m levels, comparable to the signal from the plastic core liners. Hence, no paleomagnetic interpretations were possible from shipboard measurements below this transition.

The stability of the magnetization signal is indicated by the shallow inclinations, which is consistent with the low latitude of Site 851, the sharp 180° changes in declination during reversals, and the good serial correlation of the data (Figs. 19, 20, and 21). The stability of the remanence is further illustrated by demagnetization results from two discrete samples from the same core (Fig. 22). For these samples, the upward drilling overprint, which was ubiquitous at all Leg 138 sites, essentially has been removed by the 5-mT AF treatment; the characteristic remanence then has decayed to the origin for higher AF levels. The shallow-inclination and antipodal characteristic directions of these samples are consistent with results from the pass-through magnetometer.

The magnetostratigraphy in the upper 80 mcd of Site 851 was established with relative ease, even in cores where no MST orientation was available (Figs. 19, 20, 21, and Table 7). The polarity zonations established in all holes agree closely when adjusted to composite depth with only minor discrepancies (e.g., 50-cm offset in Core 138-851B-8H, Fig. 23). Several factors contributed to the ease of magnetostratigraphic interpretation: (1) the demagnetized remanence was relatively free from secondary overprints, (2) the same sedimentary section was cored in three holes with excellent recovery, and (3) the main features of the Pliocene–Pleistocene magnetic polarity time scale (MPTS) were well constrained by biostratigraphy. Every chronozone and subchronozone of the MPTS for the past 4 m. y. from the Brunhes to the Cochiti in the Gilbert were identified in the upper 80 mcd of Site 851 (Fig. 23, Table 8). At all three deeper holes at Site 851, the early Matuyama in the zone between the Gauss/Matuyama boundary and the onset of the Olduvai contain correlatable features at 39.4 and 47.3 mcd, which might correspond to the Reunion and X(?) sub-

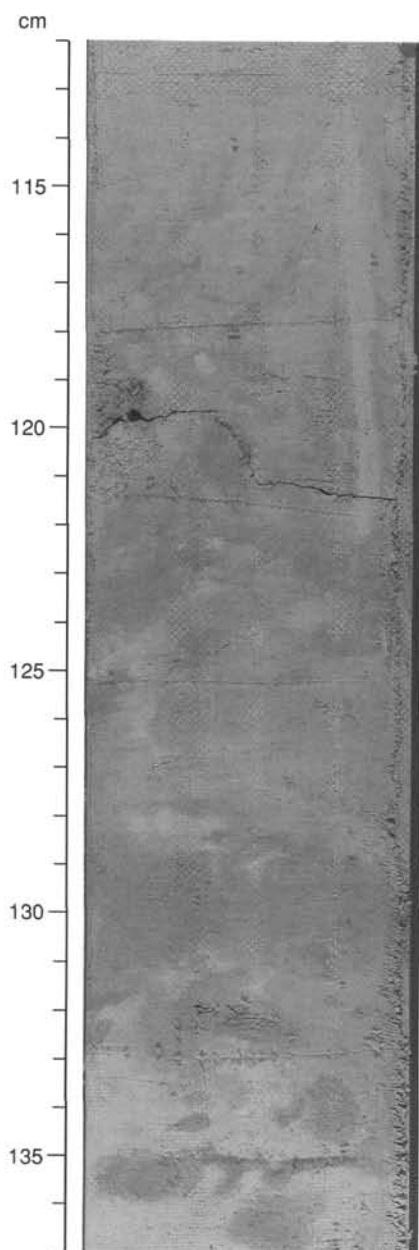


Figure 15. A single *Skolithos* burrow above bioturbated radiolarian clay and diatom-rich interbed in the interval at 138-851C-7H-4, 112–137 cm.

chons, respectively (Mankinen and Dalrymple, 1979). Moreover, the Cochiti at all three holes is characterized by fine structure in the declination profiles (Fig. 19, 20, and 21). Further shore-based studies of discrete samples will examine whether these features are of sedimentological or geomagnetic origin.

The susceptibility profile at Hole 851B (Fig. 24) exhibits a sharp decrease near 70 mbsf (80 mcd) from values averaging 3 to 4×10^{-5} SI to values near zero between 70 and 190 mbsf, which corresponds to a zone of diatom enrichment (see “Lithostratigraphy” section, this chapter) and higher uranium content (see “Downhole Measurements” section, this chapter), presumably related to periods of increased productivity and higher organic content. Biostratigraphy indicates a significant increase of sedimentation rates in this zone (see “Sedimentation Rates” section, this chapter). Thus, although magnetic particle dilution from higher sediment accumulation in the interval from 70 to 190 mbsf might account for part of the magnetization/susceptibility

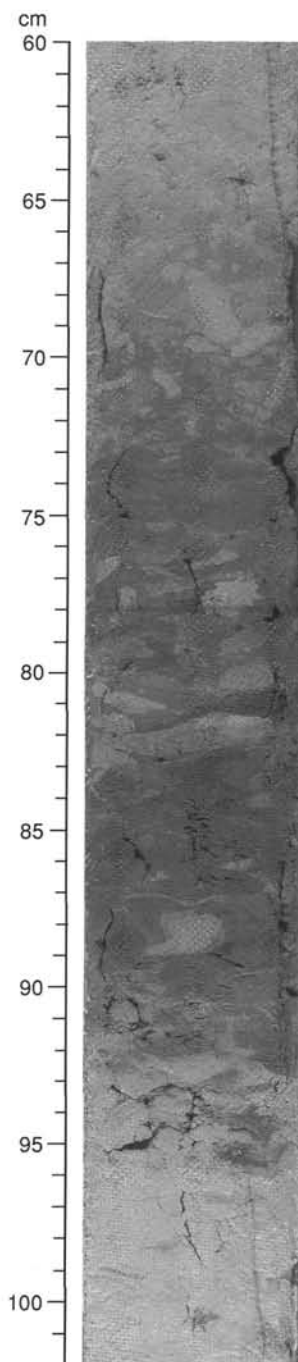


Figure 16. Intense burrowing within a diatom- and radiolarian-rich interbed in radiolarian diatom nannofossil ooze in Section 138-851E-26X-1 at 60–102

decrease, the abruptness of the boundary at 70 mbsf (80 mcd) and the virtual disappearance of the magnetic signal between 70 and 190 mbsf suggests that dissolution of the magnetite might be a significant factor. A zone of higher susceptibility between about 210 to 270 mbsf in Hole 851B correlates with higher aluminum concentrations (see “Downhole Measurements” section, this chapter), which suggests that a higher terrigenous component is present.

SEDIMENTATION RATES

A sedimentary section a little more than 300 m thick that covered the time interval from the late Pleistocene to the bottom of the late

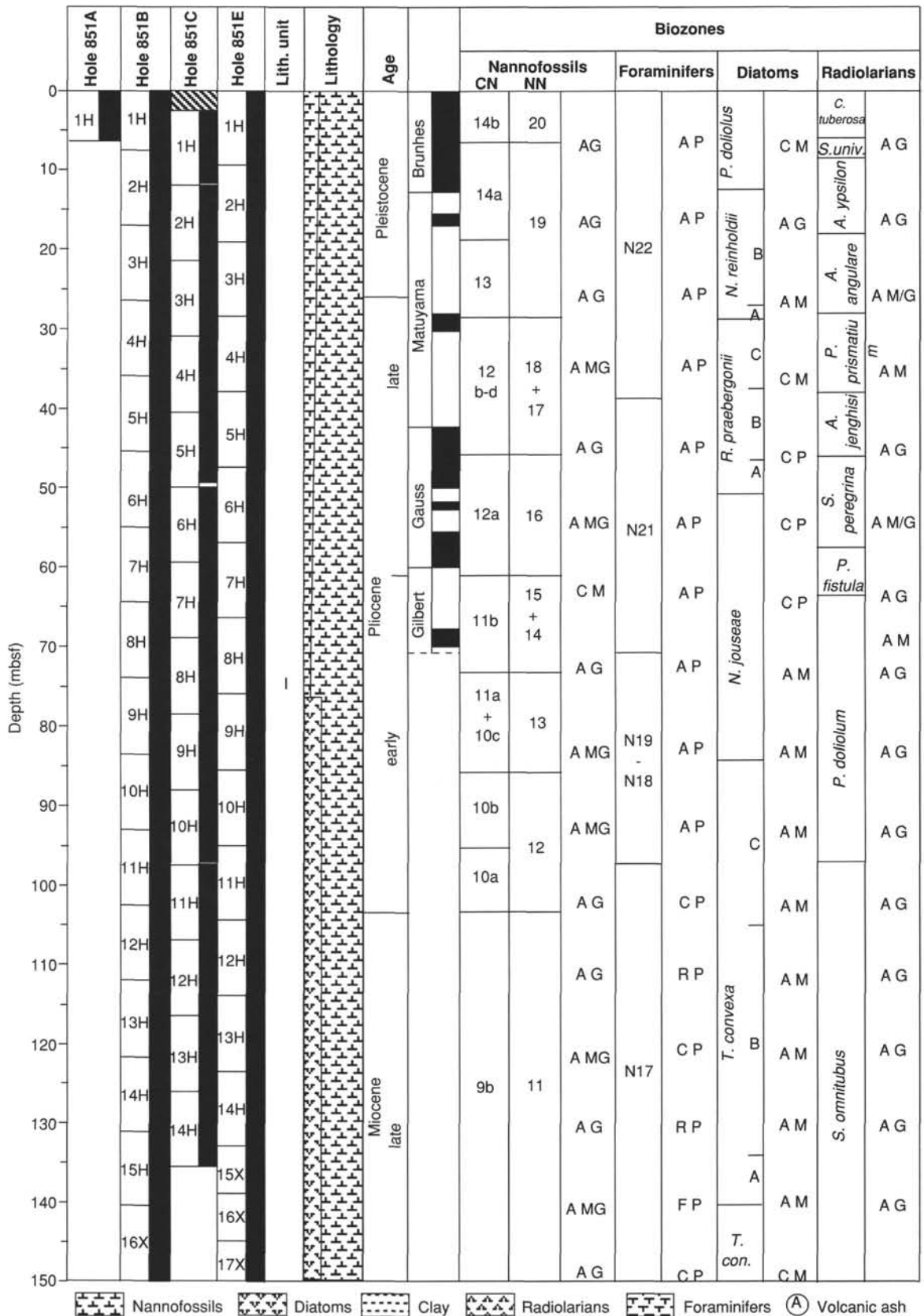


Figure 17. Biostratigraphic summary for Site 851. Hatched areas represent intervals where zones could not be assigned because of rarity or absence of microfossils. Dashed line represents uncertainty in placement of a zonal boundary. Microfossil abundance is recorded as A = abundant; C = common; F = few; R = rare; B = barren. Microfossil preservation is recorded as G = good; M = moderate; P = poor. This is a general overview of biostratigraphic results at Site 851. The data presented here are based on results from Hole 851B. Placement of specific stratigraphic boundaries may differ slightly between Hole 851B and Holes 851C and 851D.

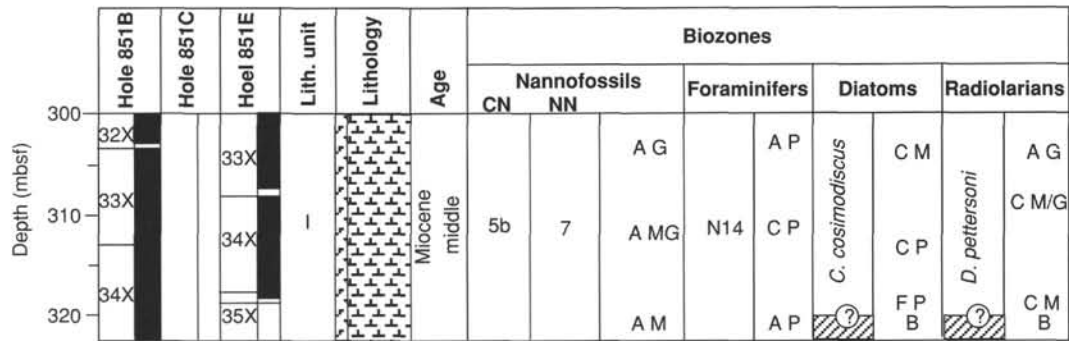


Figure 17 (continued).

Miocene was recovered at Site 851. Biostratigraphic age control was provided by all four of the chief planktonic microfossil groups.

The composite depth section for Site 851 is given in Table 9. This composite was formed by comparing shipboard measurements of GRAPE, magnetic susceptibility, and percentage of reflectance data (from the automated color analyzer) at adjacent holes. These comparisons were then integrated to form a single composite depth section for the site (a detailed discussion about the construction of composite sections during Leg 138 is presented in Hagelberg et al., this volume).

For the holes and cores listed in Column 1 of Table 9, Column 2 gives the ODP sub-bottom depth of the core top and core bottom (in meters below seafloor, or mbsf). Note that the depth given in Column 2 corresponds to the depth of the bottom of the recovered core. This depth places the core catchers in their correct positions in the composite section and is not the same as the standard ODP core-catcher depth. Column 3 shows the length of core recovered. Column 4 gives the composite depth of the core top and core bottom (in meters composite depth, or mcd). Column 5 indicates the amount of offset between the ODP and the composite depths. Conversion from ODP sub-bottom to composite depths was done by adding the offset listed in Column 5 for a given core.

Both GRAPE density and percentage of reflectance data showed a relatively high-amplitude variability through much of the section at Site 851 (Fig. 25, back pocket). The magnetic susceptibility record shows relatively high amplitudes from 0 to 80 mcd and from 240 mcd to the basement, which made it a useful correlation tool in these intervals. This site was double-cored to basement at two holes (Holes 851B and 851E), with the objective of producing a continuous section having overlap to the basement. In the XCB-cored section, GRAPE, color, and susceptibility data were sufficient to correlate these two holes down to the basement at 387.04 mcd.

Analysis of the composite section indicated that overlap of adjacent holes was maintained down through all of the APC-cored (14 cores) and most of the XCB-cored (30 cores) intervals at Site 851. In the XCB-cored section, overlap was not maintained in five locations. Two locations of no overlap occurred at the beginning of the XCB-cored interval, between Cores 138-851B-15H and -851B-16X and between Cores 138-851B-16X and -851E-17X. The remaining intervals of no overlap between adjacent holes are Cores 138-851B-21X and -851E-21X, Cores 138-851B-22X and -851E-22X, and Cores 138-851B-29X and -851E-30X. When no overlap

Table 3. Sample and depth constraints of calcareous nannofossil events for Hole 851B.

| Event | Hole 851B | | | Hole 851C | | |
|---|----------------------|---------------|---------------|--------------------|--------------|-------------|
| | Interval (cm) | Depth (mbsf) | Depth (mcd) | Interval (cm) | Depth (mbsf) | Depth (mcd) |
| T <i>Pseudoemiliania lacunosa</i> | 1H-5, 95-1H-5, 140 | 6.95-7.40 | 6.95-7.40 | | | |
| B <i>Gephyrocapsa</i> sp. 3 | 2H-6, 50-2H-CC | 15.50-17.17 | 17.85-20.05 | 2H-3,140-2H-4, 25 | 16.40-16.75 | 20.40-20.75 |
| T <i>Gephyrocapsa</i> spp. >5.5 µm | 3H-2, 90-3H-3, 30 | 19.40-20.30 | 23.55-24.45 | 2H-6, 25-2H-6, 70 | 19.75-20.20 | 23.75-24.20 |
| B <i>Gephyrocapsa</i> spp. >5.5 µm | 3H-5, 30-3H-5, 60 | 23.30-23.60 | 27.45-27.75 | | | |
| T <i>Calcidiscus macintyreii</i> | 3H-6, 100-3H-7, 46 | 25.50-26.46 | 29.65-30.24 | | | |
| B <i>Gephyrocapsa oceanica</i> s.l. | 3H-CC-4H-1, 19 | 27.10-26.69 | 31.25-32.09 | 3H-3, 70-3H-3, 140 | 25.20-25.90 | 31.25-31.95 |
| T <i>Discoaster brouweri</i> | 4H-3, 100-4H-3, 150 | 30.50-31.00 | 35.90-36.40 | | | |
| T <i>Discoaster surculus</i> | 5H-7, 65-5H-CC | 45.65-45.89 | 51.95-52.19 | | | |
| T <i>Discoaster tamalis</i> | 5H-7, 65-5H-CC | 45.65-45.89 | 51.95-52.19 | | | |
| T <i>Sphenolithus</i> spp. | 7H-3, 58-7H-4, 60 | 58.58-60.10 | 67.03-68.55 | | | |
| T <i>Reticulofenestra pseudoumbilicus</i> | 7H-6, 25-7H-6, 60 | 62.75-63.10 | 71.20-71.55 | | | |
| B <i>Discoaster asymmetricus</i> | 8H-7, 37-8H-CC | 73.87-74.54 | 83.77-84.44 | | | |
| B <i>Ceratolithus rugosus</i> | 10H-2, 25-10H-2, 60 | 85.25-85.60 | 97.20-97.55 | | | |
| B <i>Ceratolithus acutus</i> | 11H-2, 60-11H-2, 110 | 95.10-95.60 | 108.25-108.75 | | | |
| T <i>Discoaster quinqueramus</i> | 11H-CC-12H-1, 30 | 103.01-102.80 | 116.16-117.80 | | | |
| T <i>Amaurolithus amplifucus</i> | 13H-3, 68-13H-4, 70 | 115.68-117.20 | 131.48-133.00 | | | |
| B <i>Amaurolithus amplifucus</i> | 15H-6, 69-15H-7, 63 | 139.19-140.63 | 157.54-158.98 | | | |
| B <i>Amaurolithus primus</i> | 18X-CC-19X-1, 25 | 169.49-169.65 | 197.94-199.40 | | | |
| T <i>Minylitha convallis</i> | 19X-1, 25-19X-1, 58 | 169.65-169.93 | 199.40-199.68 | | | |
| B <i>Discoaster berggreni</i> | 20X-CC-21X-1, 25 | 188.93-188.55 | 224.88-227.90 | | | |
| T <i>Discoaster hamatus</i> | 24X-7, 30-25X-1, 60 | 226.10-227.00 | 272.20-276.10 | | | |
| B <i>Minylitha convallis</i> | 25X-1, 60-25X-2, 60 | 227.00-228.50 | 276.10-277.60 | | | |
| T <i>Coccolithus miopelagicus</i> | 28X-3, 40-28X-3, 80 | 258.90-259.30 | 314.80-315.20 | | | |
| B <i>Discoaster hamatus</i> | 28X-3, 40-28X-3, 80 | 258.90-259.30 | 314.80-315.20 | | | |
| B <i>Catinaster coalitus</i> | 29X-5, 71-29X-CC | 271.81-272.83 | 330.21-331.23 | | | |

T = top occurrence; B = bottom occurrence.

between adjacent holes was encountered, the core depths were adjusted so as to leave no gaps among the cores.

Examination of the composite depth section at this site (Table 9) shows that the average amount of additional offset applied to successive cores depended on the coring method. In the APC-cored interval, the length of the sedimentary section in composite depth is about 13% greater than the mbsf depth. In the XCB-cored interval, this difference was about 26%. If this relationship held at other sites, then, in general, much more of the sedimentary sequence could be lost among successive XCB cores in a single hole than in between successive APC cores. The results from coring Site 851 demonstrated that most of the "missing" section can be recovered through a double XCB-coring strategy. If this site had been cored a single time in the section below the range of the APC, perhaps only approximately 75% of the total sedimentary section would have been recovered (Fig. 25, back-pocket).

Developing a satisfactory sedimentation rate record for Site 851 was assisted by a good paleomagnetic record for the Pleistocene and part of the Pliocene. In addition, all four microfossil groups provided good biostratigraphic information in different parts of the record. In Table 10 we give the control points selected to generate the age-vs.-depth plots shown in Figure 26. At the base of the section, the top of the range of *Coccolithus gigas* var. *diorama* (10.7 Ma) and the first appearance of *Hemidiscus cuneiformis* (11.1 Ma) were observed between Samples 138-851B-31X-CC and -32X-CC and between Samples 138-851B-32X-CC and -33X-CC, respectively. The lowest control point used to estimate sedimentation rates was an average of these two estimates (see Fig. 26B; the additional datum indicated on this plot at 11.5 Ma, the last appearance of *Actinocyclus ingens*, was regarded as less reliable). Nannofossil and diatom datums fall close to the age-depth line shown in Figures 26A and 26B; several of the radiolarian datums in the Miocene section deviate from it (Fig. 26C). The pattern of deviation is consistent with that observed at Sites 849 and 850 and suggests an inconsistency in the calibration of the datums for the various microfossil groups.

The pattern of sedimentation rate variation vs. age (Fig. 27) and depth (Fig. 28) has some resemblance to those of Sites 848, 849, and 850; two peaks of high sedimentation rate occur for the

earliest Pliocene and the late Miocene. In addition, a slightly higher sedimentation rate in the deepest part of the section exists at the base of the late Miocene. Note that the development of a true composite section leads to an exaggeration of the sedimentation rate. With recovery using the APC, this amounts to about 10% to 15% (which is negligible compared to the uncertainties involved when estimating sedimentation rates from biostratigraphic datums determined aboard the ship). On the other hand, through that part of the record that was recovered with the XCB (for Site 851, below 160 mcd), the exaggeration in sedimentation rate is nearer 25%, which is enough to bias a comparison with sites where only a single XCB section was cored, so that a composite depth section was not created.

INORGANIC GEOCHEMISTRY

Fifteen interstitial water samples were collected at Site 851: two from Hole 851A at 1.4 and 5.9 mbsf and 13 from Hole 851B, from 26.0 mbsf to just above the basement at 317.4 mbsf (Table 11). Results from these two holes are here considered to constitute a single depth profile.

An interstitial-water sample was taken from Sections 1 and 4 of the solitary core that makes up Hole 851A. Core 138-851A-1H consisted of foraminifer nannofossil ooze with diatoms through Section 138-851A-1H-4. The first interstitial-water sample was taken from the brown ooze that composes Section 138-851A-1H-1; the second sample from this core was taken from Section 138-851A-1H-4, just below the brown/green transition at 115 cm (see "Lithostratigraphy" section, this chapter).

Interstitial-water sampling in Hole 851B began with a sample from the third core (Section 138-851B-3H-6), which is composed of yellowish-gray to greenish-gray foraminifer nannofossil ooze with diatoms and radiolarians. Beginning with this core, one interstitial-water sample was taken from every third core through Core 138-851B-27X. Core 138-851B-30X was retrieved without sediment, but every core was sampled for interstitial water down to the basement, beginning with Core 138-851B-31X.

In general, the sediments in Hole 851B consist of variations of nannofossil ooze. Some chert fragments were recovered in Sample

Table 3 (continued).

| Event | Hole 851E | | |
|---|---------------------|---------------|---------------|
| | Interval (cm) | Depth (mbsf) | Depth (mcd) |
| T <i>Pseudoemiliana lacunosa</i> | | | |
| B <i>Gephyrocapsa</i> sp. 3 | 2H-5, 15-2H-5, 45 | 15.65-15.95 | 19.15-19.45 |
| T <i>Gephyrocapsa</i> spp. >5.5 μ m | | | |
| B <i>Gephyrocapsa</i> spp. >5.5 μ m | | | |
| T <i>Calcidiscus macintyreii</i> | | | |
| B <i>Gephyrocapsa oceanica</i> s.l. | | | |
| T <i>Discoaster brouweri</i> | | | |
| T <i>Discoaster surculus</i> | | | |
| T <i>Discoaster tamalis</i> | | | |
| T <i>Sphenolithus</i> spp. | | | |
| T <i>Reticulofenestra pseudoumbilicus</i> | | | |
| BC <i>Discoaster asymmetricus</i> | | | |
| B <i>Ceratolithus rugosus</i> | | | |
| B <i>Ceratolithus acutus</i> | | | |
| T <i>Discoaster quinqueramus</i> | 11H-6, 44-11H-6, 90 | 102.94-103.40 | 116.24-116.70 |
| T <i>Amaurolithus amplificus</i> | | | |
| B <i>Amaurolithus amplificus</i> | | | |
| B <i>Amaurolithus primus</i> | 19X-4, 25-19X-4, 60 | 169.05-169.40 | 199.25-199.60 |
| T <i>Minylitha convallis</i> | | | |
| B <i>Discoaster berggreni</i> | | | |
| T <i>Discoaster hamatus</i> | 25X-4, 25-25X-4, 56 | 225.95-226.26 | 275.05-275.36 |
| B <i>Minylitha convallis</i> | | | |
| T <i>Coccolithus miopelagicus</i> | | | |
| B <i>Discoaster hamatus</i> | | | |
| B <i>Catinaster coalitus</i> | | | |

Table 4. Sample and depth constraints of planktonic foraminifer events for Hole 851B.

| Event | Interval | Hole 851B | |
|---------------------------------------|---------------|---------------|---------------|
| | | Depth (mbsf) | Depth (mcd) |
| T <i>Globigerinoides fistulosus</i> | 3H-CC-4H-CC | 27.10-36.41 | 31.25-41.81 |
| T <i>Globorotalia limbata</i> | 3H-CC-4H-CC | 27.10-36.41 | 31.25-41.81 |
| T <i>Globigerinoides obliquus</i> | 5H-CC-6H-CC | 45.89-55.60 | 52.19-63.45 |
| T <i>Dentoglobigerina altispira</i> | 5H-CC-6H-CC | 45.89-55.60 | 52.19-63.45 |
| B <i>G. fistulosus</i> | 6H-CC-7H-CC | 55.60-65.04 | 63.45-73.49 |
| T <i>Sphaeroidinellopsis</i> spp. | 6H-CC-7H-CC | 55.60-65.04 | 63.45-73.49 |
| B <i>Globorotalia tumida</i> | 10H-CC-11H-CC | 93.46-103.01 | 105.41-116.16 |
| B <i>Globorotalia plesiotumida</i> | 28X-CC-29X-CC | 265.14-272.83 | 321.04-331.23 |
| B <i>Neogloboquadrina acostaensis</i> | 31X-CC-32X-CC | 293.96-302.94 | 352.36-363.19 |
| T <i>Globorotalia siakensis</i> | 30X-CC-31X-CC | 274.80-293.96 | 333.20-352.36 |

T = top occurrence; B = bottom occurrence.

Table 5. Sample and depth constraints of radiolarian events for Site 851.

| Event | Interval | Hole 851B | | Hole 851C | | |
|--|---------------|---------------|---------------|-------------|--------------|-------------|
| | | Depth (mbsf) | Depth (mcd) | Interval | Depth (mbsf) | Depth (mcd) |
| T <i>Stylatractus universus</i> | 1H-4-1H-CC | 5.60-7.58 | 5.60-7.58 | | | |
| B <i>Collosphaera tuberosa</i> | 1H-CC-2H-2 | 9.90-12.45 | 7.58-10.10 | | | |
| T <i>Lamprocyrtis neoheteroporos</i> | 2H-CC-3H-4 | 19.55-20.10 | 19.60-22.60 | | | |
| T <i>Anthocyrtidium angulare</i> | 2H-CC-3H-2 | 17.17-19.60 | 22.70-23.75 | | | |
| T <i>Theocorythium vetulum</i> | 2H-CC-3H-2 | 17.17-19.60 | 22.70-23.75 | | | |
| B <i>Lamprocyrtis nigrinae</i> | 2H-CC-3H-2 | 17.17-19.60 | 22.70-23.75 | | | |
| B <i>Theocorythium trachelium</i> | 3H-CC-4H-2 | 31.25-33.30 | 27.10-29.50 | | | |
| B <i>Pterocorys minytorax</i> | 3H-CC-4H-2 | 31.25-33.30 | 27.10-29.50 | | | |
| B <i>Anthocyrtidium angulare</i> | 3H-6-3H-CC | 29.75-31.25 | 25.60-27.10 | | | |
| T <i>Pterocanium prismatium</i> | 3H-CC-4H-2 | 31.25-33.30 | 27.10-29.50 | | | |
| T <i>Lamprocyrtis heteroporos</i> | 3H-2-3H-4 | 23.75-26.75 | 19.60-22.60 | | | |
| T <i>Anthocyrtidium jenghisi</i> | 4H-CC-5H-2 | 36.41-38.60 | 41.81-44.90 | | | |
| B <i>Theocalyptra davisiana</i> | 5H-6-5H-CC | 44.60-45.89 | 50.90-52.20 | | | |
| T <i>Stichocorys peregrina</i> | 5H-CC-6H-2 | 45.89-48.10 | 54.90-55.95 | | | |
| T <i>Anthocyrtidium pliocenica</i> | 6H-CC-7H-3 | 63.45-65.20 | 55.51-58.00 | | | |
| B <i>Lamprocyrtis neoheteroporos</i> | 5H-6-5H-CC | 44.60-45.89 | 50.90-52.20 | | | |
| B <i>Lamprocyrtis heteroporos</i> | 6H-4-6H-6 | 57.95-60.95 | 50.10-53.10 | | | |
| T <i>Phormostichoartus fistula</i> | 6H-CC-7H-3 | 65.20-66.45 | 55.60-58.00 | | | |
| T <i>Lychnodietyrum audax</i> | 7H-5-7H-6 | 69.45-70.95 | 61.00-62.50 | | | |
| T <i>Spongaster pentas</i> | 7H-CC-8H-2 | 65.04-67.10 | 73.45-75.70 | | | |
| T <i>Phormostichoartus doliolum</i> | 7H-6-7H-CC | 62.50-65.04 | 70.95-73.45 | | | |
| B <i>Amphirhopalum ypsilon</i> | 7H-CC-8H-2 | 65.04-67.10 | 73.45-77.00 | | | |
| B <i>Spongaster tetras</i> | 8H-CC-9H-CC | 74.54-84.14 | 84.44-94.54 | | | |
| T <i>Didymocyrtis penultima</i> | 8H-2-8H-4 | 77.00-78.99 | 67.10-70.10 | 6H-CC-7H-CC | 59.99-69.39 | 68.69-78.99 |
| B <i>Pterocanium prismatium</i> | 10H-CC-11H-2 | 93.46-95.60 | 105.45-107.60 | | | |
| T <i>Spongaster berminghami</i> | 11H-6-11H-CC | 114.75-116.15 | 101.60-103.00 | | | |
| T <i>Solenosphaera omnitubus</i> | 11H-4-11H-6 | 98.60-101.60 | 111.75-114.75 | | | |
| T <i>Siphostichartus corona</i> | 12H-CC-13H-2 | 112.61-113.60 | 127.60-129.40 | | | |
| T <i>Acrobotrys tritubus</i> | 14H-CC-15H-2 | 131.37-133.60 | 150.40-151.95 | | | |
| T <i>Stichocorys johnsoni</i> | 14H-CC-15H-2 | 131.37-133.60 | 148.55-150.40 | | | |
| <i>Stichocorys delmontensis</i> > <i>S. peregrina</i> | 17X-2-17X-4 | 152.70-155.70 | 176.20-179.20 | | | |
| T <i>Calocyrtella caepa</i> | 14H-CC-15H-2 | 131.37-133.60 | 150.40-151.95 | | | |
| B <i>Solenosphaera omnitubus</i> | 17X-CC-18X-2 | 159.87-162.40 | 183.40-190.85 | | | |
| T <i>Diartus hughesi</i> | 19X-CC-20X-2 | 208.75-217.65 | 179.00-181.70 | | | |
| B <i>Acrobotrys tritubus</i> | 18X-CC-19X-CC | 169.49-179.00 | 197.45-208.75 | | | |
| B <i>Spongaster berminghami</i> | 22X-6-22X-CC | 205.10-207.29 | 244.45-246.65 | | | |
| T <i>Stichocorys wolffii</i> | 23X-6-23X-CC | 214.70-216.87 | 259.65-261.85 | | | |
| T <i>Botryostrobus miralestensis</i> | 21X-4-21X-6 | 193.90-196.90 | 233.25-236.25 | | | |
| T <i>Diartus pettersoni</i> | 21X-6-21X-CC | 196.90-197.14 | 236.25-236.49 | | | |
| B <i>Lithopera bacca</i> | 28X-CC-29X-1 | 265.14-266.20 | 321.04-324.60 | | | |
| <i>Diartus pettersoni</i> > <i>D. hughesi</i> | 22X-CC-23X-2 | 207.29-209.70 | 246.65-254.65 | | | |
| B <i>Diartus hughesi</i> | 23X-2-23X-4 | 209.70-212.70 | 254.65-257.65 | | | |
| T <i>Cyrtocapsella japonica</i> | 26X-4-26X-6 | 241.70-244.70 | 294.50-297.50 | | | |
| T <i>Lithopera thornburgi</i> | 26X-6-26X-CC | 244.70-245.30 | 297.50-298.10 | | | |
| T <i>Carpocanium cristata</i> | 28X-CC-29X-1 | 265.14-266.20 | 321.04-324.60 | | | |

T = top occurrence; B = bottom occurrence; > = evolutionary transition.

138-851B-29X-CC, and one can reasonably assume that this deposit was responsible for the absence of recovery with Core 138-851B-30X. Unlike Sites 849 and 850, however, no distinct chert layers were recovered at this site. Moreover, the chert recovered at 273 mbsf does not seem to have influenced the interstitial-water profiles (Figs. 29, 30, and 31) as much as at the previous two sites. This observation suggests that the chert at Site 851 is more fractured and less contiguous than the layers encountered at the previous two sites. This hypothesis is supported by logging data (see “Downhole Measurements” section, this chapter). Shifts in resistivity and “silica flux” across the chert in Hole 851B are less pronounced in Hole 851B than those across chert layers in Holes 849B or 850B.

Indications of hydrothermal influence do not appear until the deepest core at the site (Core 138-851B-33X), which contains hematite, goethite, and oxide manganese dendrites (see “Lithostratigraphy” section, this chapter). Material in the core catcher from this core

(138-851-33X-CC) graded from metalliferous sediment, to highly altered basalt fragments, to basalt chips.

The smell of H₂S was completely absent at this site. This observation brings the olfactory record for the western transect full-circle. The odor of H₂S was absent at Site 848, strong at Site 849, weak at Site 850, and absent at Site 851. This qualitative scale is consistent with the diagenetic status of these sediments, as recorded in the interstitial-water chemistry.

Downhole changes in the chemistry of interstitial waters at Site 851 (Table 11) are dominated by recrystallization; alteration of crust seems may be less important here than at other Leg 138 sites. The perturbations in pore-water chemistry associated with diagenesis are also less pronounced at this site than those detected at the previous two sites.

The total spreads in sodium (Fig. 29A) and chloride (Fig. 29B) concentrations at this site are 1.6% and 1.4%, respectively. While these changes are somewhat greater than the analytical precision

Table 5 (continued).

| Event | Hole 851E | | |
|---|---------------|---------------|---------------|
| | Interval | Depth (mbsf) | Depth (mcd) |
| T <i>Stylatractus universus</i> | | | |
| B <i>Collosphaera tuberosa</i> | 1H-CC-2H-CC | 9.86-22.69 | 9.86-19.19 |
| T <i>Lamprocyrtis neoheteroporos</i> | 1H-1-2H-50 | 0-20.10 | 0-16.60 |
| T <i>Anthocyrtidium angulare</i> | 2H-CC-3H-CC | 22.69-33.26 | 19.19-29.06 |
| T <i>Theocorythium vetulum</i> | 2H-CC-3H-CC | 22.69-33.26 | 19.19-29.06 |
| B <i>Lamprocyrtis nigrinae</i> | 2H-CC-3H-CC | 22.69-33.26 | 19.19-29.06 |
| B <i>Theocorythium trachelium</i> | 2H-CC-3H-CC | 22.69-33.26 | 19.19-29.06 |
| B <i>Pterocorys minythorax</i> | 2H-CC-3H-CC | 22.69-33.26 | 19.19-29.06 |
| B <i>Anthocyrtidium angulare</i> | | | |
| T <i>Pterocanium prismatium</i> | 2H-CC-3H-CC | 22.69-33.26 | 19.19-29.06 |
| T <i>Lamprocyrtis heteroporos</i> | | | |
| T <i>Anthocyrtidium jenghisi</i> | | | |
| B <i>Theocalyptra davisiana</i> | | | |
| T <i>Stichocorys peregrina</i> | 5H-CC-6H-CC | 54.92-65.21 | 48.10-57.60 |
| T <i>Anthocyrtidium pliocenica</i> | 5H-CC-6H-CC | 54.92-65.21 | 48.10-57.60 |
| B <i>Lamprocyrtis neoheteroporos</i> | | | |
| B <i>Lamprocyrtis heteroporos</i> | | | |
| T <i>Phormostichoartus fistula</i> | 6H-CC-7H-CC | 65.21-75.70 | 57.60-67.10 |
| T <i>Lychnodictyum audax</i> | | | |
| T <i>Spongaster pentas</i> | 6H-CC-7H-CC | 65.21-75.70 | 57.60-67.10 |
| T <i>Phormostichoartus doliolum</i> | | | |
| B <i>Amphirhopalum ypsilon</i> | | | |
| B <i>Spongaster tetras</i> | | | |
| T <i>Didymocyrtis penultima</i> | | | |
| B <i>Pterocanium prismatium</i> | 9H-CC-10H-CC | 97.15-107.63 | 87.05-95.60 |
| T <i>Spongaster berminghami</i> | | | |
| T <i>Solenosphaera omnitubus</i> | | | |
| T <i>Siphostichartus corona</i> | | | |
| T <i>Acrobotrys tritubus</i> | 14H-CC-15H-CC | 150.38-158.34 | 133.70-149.40 |
| T <i>Stichocorys johnsoni</i> | 13H-CC-14H-CC | 140.36-150.38 | 130.30-133.70 |
| <i>Stichocorys delmontensis</i> | | | |
| <i>S. peregrina</i> | | | |
| T <i>Calocycletta caepa</i> | 14H-CC-15H-CC | 150.38-158.34 | 133.70-149.40 |
| B <i>Solenosphaera omnitubus</i> | | | |
| T <i>Diartus hughesi</i> | | | |
| B <i>Acrobotrys tritubus</i> | | | |
| B <i>Spongaster berminghami</i> | | | |
| T <i>Stichocorys wolffii</i> | | | |
| T <i>Botryostrobos miralestensis</i> | | | |
| T <i>Diartus pettersoni</i> | | | |
| B <i>Lithopera bacca</i> | | | |
| <i>Diartus pettersoni</i> > <i>D. hughesi</i> | | | |
| B <i>Diartus hughesi</i> | | | |
| T <i>Cyrtocapsella japonica</i> | | | |
| T <i>Lithopera thornburgi</i> | | | |
| T <i>Carpocanium cristata</i> | | | |

Table 6. Sample and depth constraints of diatom events for Site 851.

| Event | Hole 851B | | | Hole 851C | | |
|--|---------------------|---------------|---------------|---------------|---------------|---------------|
| | Interval (cm) | Depth (mbsf) | Depth (mcd) | Interval (cm) | Depth (mbsf) | Depth (mcd) |
| T <i>Nitzschia reinholdii</i> | 1H-CC-2H-CC | 7.58-17.17 | 7.58-19.52 | | | |
| T <i>Nitzschia fossils</i> | 1H-CC-2H-CC | 7.58-17.17 | 7.58-19.52 | 1H-CC-2H-CC | 11.82-21.86 | 15.32-21.86 |
| T <i>Rhizosolenia praebergonii</i> | 3H-CC-4H-1, 90 | 27.10-27.40 | 31.25-32.80 | 2H-CC-3H-CC | 21.86-31.44 | 25.86-37.49 |
| B <i>Pseudoornotia doliolus</i> | 4H-1, 90-4H-3, 60 | 27.40-30.10 | 32.80-35.50 | 3H-CC-4H-CC | 31.44-41.18 | 37.49-48.03 |
| T <i>Thalassiosira convexa</i> | 5H-1, 75-5H-3, 75 | 36.75-39.75 | 43.05-46.05 | 4H-CC-5H-CC | 41.18-49.22 | 48.03-57.72 |
| T <i>Nitzschia jouseae</i> | 5H-CC-6H-3, 1 | 45.89-48.51 | 52.19-56.36 | 4H-CC-5H-CC | 41.18-49.22 | 48.03-57.72 |
| B <i>Rhizosolenia praebergonii</i> | 6H-3, 1-6H-5, 1 | 48.51-51.51 | 56.36-59.36 | 5H-CC-6H-CC | 49.22-59.99 | 57.72-68.69 |
| T <i>Actinocyclus ellipticus</i> | 5H-CC-6H-CC | 45.89-55.60 | 52.14-63.45 | | | |
| B <i>Thalassiosira convexa</i> var. <i>convexa</i> | 7H-5, 1-7H-6, 1 | 61.01-62.51 | 69.46-70.96 | 6H-CC-7H-CC | 59.99-69.39 | 68.69-78.99 |
| B <i>Asteromphalus elegans</i> | 7H-CC-8H-CC | 65.04-74.54 | 73.49-84.44 | | | |
| T <i>Nitzschia cylindrica</i> | 9H-CC-10H-CC | 84.14-93.46 | 94.54-105.41 | 8H-CC-9H-CC | 78.59-87.93 | 89.09-100.23 |
| B <i>Nitzschia jouseae</i> | 9H-CC-10H-CC | 84.14-93.46 | 94.54-105.41 | 8H-CC-9H-CC | 78.59-87.93 | 89.09-100.23 |
| T <i>Thalassiosira miocenica</i> | 11H-CC-12H-CC | 103.01-112.64 | 116.16-127.64 | 10H-CC-11H-CC | 97.23-107.59 | 110.33-122.24 |
| T <i>Nitzschia miocenica</i> | 13H-CC-14H-2, 70 | 122.19-123.70 | 137.99-140.85 | 12H-CC-13H-CC | 117.15-126.62 | 133.15-143.72 |
| T <i>Nitzschia miocenica</i> var. <i>elongata</i> | 14H-5, 70-14H-6, 70 | 128.20-129.70 | 145.35-146.85 | 13H-CC-14H-CC | 126.62-136.14 | 143.72-154.54 |
| T <i>Thalassiosira praeconvexa</i> | 15H-2, 90-15H-6, 20 | 133.40-138.70 | 151.75-157.05 | | | |
| B <i>Thalassiosira miocenica</i> | 15H-CC-16H-4, 80 | 140.89-145.80 | 159.24-164.55 | | | |
| B <i>Thalassiosira convexa</i> var. <i>aspinosa</i> | 15H-CC-16X-4, 80 | 140.89-145.80 | 159.24-164.55 | | | |
| B <i>Thalassiosira praeconvexa</i> | 16X-CC-17X-CC | 150.00-159.87 | 168.55-183.37 | | | |
| T <i>Nitzschia miocenica</i> | 18X-CC-19X-2, 80 | 169.49-171.70 | 197.94-201.45 | | | |
| T <i>Rhizosolenia paleacea</i> | 19X-2, 80-19X-3, 80 | 171.70-173.20 | 201.45-202.95 | | | |
| T <i>Actinocyclus ellipticus</i> var. <i>javanicus</i> | 20X-CC-21X-CC | 188.93-197.14 | 224.88-236.49 | | | |
| B <i>Nitzschia cylindrica</i> | 21X-CC-22X-CC | 197.14-207.29 | 236.49-246.64 | | | |
| T <i>Thalassiosira yabei</i> | 21X-CC-22X-CC | 197.14-207.29 | 236.49-246.64 | | | |
| T <i>Denticulopsis hustedtii</i> | 24X-CC-25X-1, 80 | 226.56-227.21 | 272.66-276.30 | | | |
| T <i>Actinocyclus moronensis</i> | 25X-2, 80-25X-7, 35 | 228.70-234.75 | 277.80-284.85 | | | |
| T <i>Coccinodiscus gigas</i> var. <i>diorama</i> | 31X-CC-32X-CC | 293.96-302.94 | 352.36-363.19 | | | |
| B <i>Hemidiscus cuneiformis</i> | 32X-CC-33X-CC | 302.94-313.13 | 363.19-377.08 | | | |

T = top occurrence; B = bottom occurrence.

(0.5%), the deviations are still small and can be attributed to random error and sampling artifacts. For all practical purposes, we can say that these elements are not being produced or consumed at this site, nor is there any evidence for vertical advection. The same can be said for magnesium (Fig. 30A), calcium (Fig. 30B), and potassium (Fig. 30C). The invariant nature of these profiles holds all the way to basement.

The absence of any discernable trends in these profiles can be attributed to two factors: a low organic carbon burial rate and the absence of a contiguous chert zone. Lowering the carbon burial rate results in fewer diagenetic effects. Without the complete development of chert layers, the sediment column is a more open system that allowed for unencumbered, diffusive exchange with basal sediments and that diluted the impact of basement alteration on pore-water chemistry.

Changes in interstitial alkalinity (Fig. 29C) and sulfate (Fig. 29D) were measurable at Site 851. These profiles indicate a broad zone of mildly reducing pore water that begins at about 30 mbsf and continues to 290 mbsf. These changes in sulfate values are barely detectable, and one has difficulty resolving the region of greatest diagenetic activity based on these results. The alkalinity data, however, are considerably less scattered and may indicate maximum change at about 150 to 160 mbsf. This analysis is supported by the ammonia profile (Fig. 31C), which shows a distinct maximum at these same depths. Still, while a discernable and consistent pattern exists in three diagenetic indicators: alkalinity, sulfate, and ammonia, the level of reductive activity at Site 851 is low compared to that at Sites 849 and 850.

The highest alkalinity value attained at Site 850 was 5.414 mM; the highest alkalinity value for Site 851 was 3.840 mM (Table 11). This small shift in alkalinity had a relatively large impact on calcium and magnesium geochemistries. Calcium and magnesium decrease downhole at Site 850, which is indicative of precipitating calcium carbonate, while at Site 851, calcium (Fig. 30B) and magnesium (Fig. 30A) values remain invariant throughout the sediment column.

Strontium values at Site 851 increase (Fig. 31B) in response to the recrystallization of biogenic calcite (Elderfield and Gieskes, 1982; Baker et al., 1982; Gieskes et al., 1986; Baker, 1986). The lithium

profile at Site 851 (Fig. 31B) is similar to those developed for other Leg 138 sites and shows that lithium decreases sympathetically as strontium increases.

As pointed out previously, a systematic decrease in reductive intensity exists going from Site 849, to Site 850, to Site 851. It is informative to plot lithium vs. strontium and to compare this relationship across this series of sites (Fig. 32). Three relationships emerge from this illustration: (1) lithium and strontium are linearly related at all three sites, (2) strontium increases by a different amount at every site, and (3) lithium changes by the same amount at every site. Clearly, the increase in strontium is directly related to the reductive intensity of the pore water: the greater the level of diagenesis, the greater the corrosiveness of the pore water, and the greater the extent of recrystallization. On the other hand, lithium removal may be associated with the process of recrystallization, but this removal must be noncongruent.

Data from these three sites (Fig. 32) demonstrate that diagenesis affects the geologic record of calcium carbonate in two ways. First, degradation of organic matter produces bicarbonate and precipitates carbonates. This process is manifested as decreasing trends in calcium and magnesium in the top 100 m of sediment. Precipitation was invoked to explain similar trends at a number of DSDP/ODP sites, including the Lord Howe Rise (Baker, 1986) and the Oman Margin (Pedersen and Shimmiel, 1991). Second, diagenesis increases corrosiveness and, thus, the extent of recrystallization. This process has little effect on calcium or magnesium in pore waters, but increases strontium and decreases lithium. These processes degrade the carbonate record of sediments by obscuring authigenic deposits and by diminishing preservation of biogenic calcite.

Interstitial silica at Site 851 (Fig. 30D) displays a regular increase with depth: a gradient maintained by reaction with biogenic silica (Kastner, 1981; Gieskes, 1974). A broad maximum occurs between 150 and 250 mbsf, but there is no indication of a substantial difference in silica behavior between this site and other sites on Leg 138.

Similar to what has been observed at other sites on the western transect of Leg 138, the pore-water profiles of basal sediments at Site

Table 6 (continued).

| Event | Hole 851E | | |
|--|--------------------|---------------|---------------|
| | Interval (cm) | Depth (mbsf) | Depth (mcd) |
| T <i>Nitzschia reinholdii</i> | 1H-CC-2H-1, 80 | 9.86-10.30 | 9.86-13.80 |
| T <i>Nitzschia fossils</i> | 2H-1, 80-2H-5, 80 | 10.30-16.30 | 13.80-19.80 |
| T <i>Rhizosolenia praebergonii</i> | 2H-CC-3H-CC | 19.19-29.06 | 22.69-33.26 |
| B <i>Pseudoernotia doliolus</i> | 3H-CC-4H-CC | 29.06-38.55 | 33.26-44.75 |
| T <i>Thalassiosira convexa</i> | 4H-CC-5H-2, 90 | 38.55-40.40 | 44.75-47.20 |
| T <i>Nitzschia jouseae</i> | 5H-4, 90-5H-6, 90 | 43.40-46.40 | 50.20-53.20 |
| B <i>Rhizosolenia praebergonii</i> | 6H-2, 90-6H-6, 90 | 49.90-55.90 | 57.60-63.60 |
| T <i>Actinocyclus ellipticus</i> | | | |
| B <i>Thalassiosira convexa</i> var. <i>convexa</i> | 7H-4, 100-7H-5, 78 | 62.50-63.78 | 71.10-72.38 |
| B <i>Asteromphalus elegans</i> | | | |
| T <i>Nitzschia cylindrica</i> | 9H-2, 90-9H-4, 63 | 78.40-81.13 | 89.45-92.18 |
| B <i>Nitzschia jouseae</i> | 9H-4, 63-9H-5, 141 | 81.13-83.41 | 92.18-94.46 |
| T <i>Thalassiosira miocenica</i> | 11H-CC-12H-3, 32 | 105.13-107.82 | 118.43-122.27 |
| T <i>Nitzschia miocenica</i> | 13H-CC-14H-CC | 124.06-133.68 | 140.36-150.38 |
| T <i>Nitzschia miocenica</i> var. <i>elongata</i> | | | |
| T <i>Thalassiosira praeconvexa</i> | | | |
| B <i>Thalassiosira miocenica</i> | 15X-4, 50-15X-CC | 138.00-141.94 | 154.40-158.34 |
| B <i>Thalassiosira convexa</i> var. <i>aspinosa</i> | 15X-4, 50-15X-CC | 138.00-141.94 | 154.40-158.34 |
| B <i>Thalassiosira praeconvexa</i> | 15X-CC-16X-CC | 141.94-147.13 | 158.34-167.93 |
| B <i>Nitzschia miocenica</i> | 17X-CC-18X-CC | 154.75-164.40 | 178.25-192.10 |
| T <i>Rhizosolenia paleacea</i> | | | |
| T <i>Actinocyclus ellipticus</i> var. <i>javanicus</i> | | | |
| B <i>Nitzschia cylindrica</i> | 21X-CC-22X-CC | 190.11-199.68 | 231.48-243.58 |
| T <i>Thalassiosira yabei</i> | 21X-CC-22X-CC | 190.11-199.68 | 231.48-243.58 |
| T <i>Denticulopsis hustedtii</i> | 24X-CC-25X-CC | 221.47-230.98 | 268.17-280.08 |
| T <i>Actinocyclus moronensis</i> | | | |
| T <i>Coscinodiscus gigas</i> var. <i>diorama</i> | | | |
| B <i>Hemidiscus cuneiformis</i> | | | |

851 do not reflect alteration of crust, as found at other DSDP sites (e.g., McDuff, 1981) and the eastern sites of this leg. Rather, in every case, a distinct turn toward seawater concentrations at the bottom of the hole occurs. At least two possible explanations may exist for these observations. Either the conditions near the basement were not conducive to extensive, low-temperature weathering of basalt, or lateral advection of water overwhelmed the effects of alteration.

In summary, alkalinity, sulfate, and ammonia profiles at Site 851 reflect diagenesis, but less intense diagenesis than that found at Sites 849 or 850. The increase in alkalinity values at this site apparently is not large enough to precipitate diagenetic carbonates. As a result, calcium and magnesium do not decrease with depth. Strontium increases because of recrystallization. By comparison with other sites, the extent of recrystallization may be related to the intensity of organic matter diagenesis.

ORGANIC GEOCHEMISTRY

Carbonate and Organic Carbon

Inorganic and organic carbon were measured in Hole 851B following the methods outlined in the "Explanatory Notes" chapter (this volume). From the inorganic carbon data, we calculated the weight percent of calcium carbonate (%CaCO₃). The percentage of organic carbon (%C_{org}) was determined by measuring the amount of carbon in the dried residues from Coulometer analyses after treatment with 2N HCl (see "Explanatory Notes" chapter, this volume) to optimize results in sediments low in C_{org} and high in carbonate. The analytical results are listed in Table 12 (CD ROM, back pocket) with respect to both ODP depth (mbsf) and to composite depth (mcd; see "Sedimentation Rates" section, this chapter). If a duplicate analysis was performed on a given sample, the mean value of the original analysis and the duplicate has been listed in Table 12. Duplicate percentage of CaCO₃ analyses are listed in Table 13. These results indicate a reproduceability of 0.8%.

Figures 33 and 34 show percentages of CaCO₃ and C_{org} at Site 851 vs. ODP depth and vs. composite depth and age, respectively, based

on datum levels identified at Site 851 (see "Sedimentation Rates" and "Paleomagnetism" sections, this chapter). The record of percentage of CaCO₃ at Site 851 shows high values (near 75%) in the upper 200 m of the section. The interval from 220 to 290 mbsf is punctuated by several intervals of significantly lower percentages of CaCO₃ (from 20% to 50%; Fig. 33). Concentrations of organic carbon are low (0.0% to 0.2%, with only two values in the range of 0.3% to 0.5%). The intervals having low percentages of CaCO₃ coincide with partly laminated sediments that have high diatom percentages based on smear slide results (see "Lithostratigraphy" section, this chapter). According to shipboard chronostratigraphy, the pronounced low-carbonate interval may be coeval, with intervals of low percentages of CaCO₃ at companion Sites 848, 849, and 850.

Accumulation Rates

We calculated the average values of several sedimentary parameters in time intervals delimited by the chronostratigraphic levels discussed in the "Sedimentation Rates" section (this chapter) to estimate mass accumulation rates (MARs) of bulk sediment and individual sedimentary components. The average values of percentages of CaCO₃ and C_{org}, linear sedimentation rate (LSR), dry bulk density (DBD), bulk-sediment mass accumulation rate (bulk MAR), CaCO₃ MAR, and C_{org} MAR for 20 time intervals since 10.9 Ma are listed in Table 14. The mean values are presented vs. composite depth in Figure 35 and vs. age in Figure 36. Superimposed on the mean values are estimates of the instantaneous MAR calculated for each sample. The mean accumulation rates of bulk sediment reach up to 5 g/cm²/k.y. in the period from 7 to 4 Ma at Site 851 and are similar to the accumulation rate record at Site 850 in both magnitude and temporal pattern.

Gas Geochemistry

One sample for gas analysis was taken from each core of Hole 851B. Gas was released from a sediment sample (about 5 cm³) by thermal

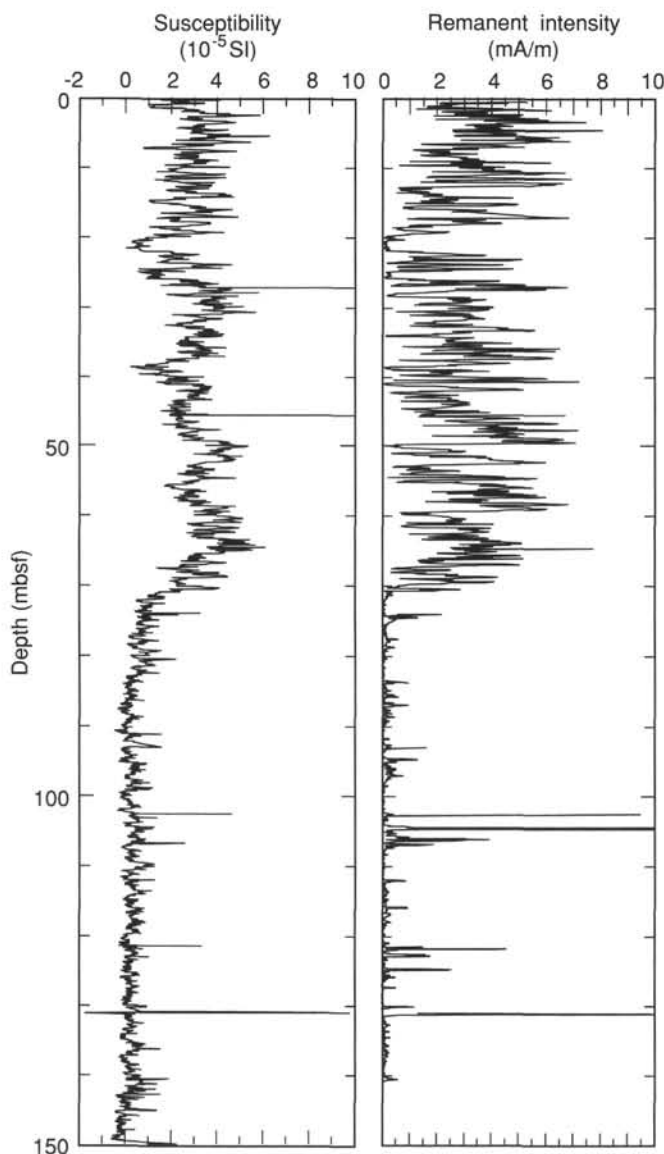


Figure 18. Downcore profiles of magnetic susceptibility and magnetization intensity, AF demagnetized at 15 mT for Hole 851B, showing the magnetic boundary at 70 mbsf (80 mcd).

desorption (i.e., the “headspace technique,” see “Explanatory Notes” section, this volume). Measured concentrations of hydrocarbons in the headspace volume (in ppm) were converted to $\mu\text{L/L}$ of sediment. Methane concentrations do not exceed $20 \mu\text{L/L}$ of sediment (Fig. 37; Table 15, CD ROM), and ethane and higher hydrocarbon gases are below detection limits.

PHYSICAL PROPERTIES

Introduction

Physical properties measured routinely in whole-round sections at Site 851 include GRAPE-density, compressional-wave velocity (using the MST), and thermal conductivity. From split-cores, we selected discrete samples for measuring index properties, including wet-bulk density, dry-bulk density, water content, porosity, and void ratio. Compressional-wave velocities were determined using the digital sonic velocimeter (DSV), and shear strength was measured using a

Table 7. Core orientations for Site 851.

| Core no. | Azimuthal orientation (0° – 360°) | Deviation from direction (0° – 360°) | Vertical drift (°) |
|--------------------------|-----------------------------------|--------------------------------------|--------------------|
| ^a 138-851A-1H | 300 | | |
| ^a -851B-1H | 220 | | |
| ^a 2H | 250 | | |
| ^a 3H | 305 | | |
| 4H | 220 | 306 | 0.8 |
| 5H | 128 | 269 | 1.7 |
| 6H | 244 | 251 | 1.5 |
| 7H | (040) | 255 | 2.0 |
| ^a 7H | 205 | | |
| 8H | 153 | 267 | 1.7 |
| 9H | 213 | 244 | 2.0 |
| 10H | 066 | 245 | 1.8 |
| 11H | 105 | 250 | 1.9 |
| 12H | 195 | 244 | 2.0 |
| 13H | 043 | 235 | 1.4 |
| 14H | 025 | 246 | 1.9 |
| 15H | 205 | 272 | 1.2 |
| ^a -851C-1H | 170 | | |
| ^a 2H | 260 | | |
| ^a 3H | 060 | | |
| 4H | (083) | 203 | 1.2 |
| ^a 4H | 340 | | |
| 5H | 148 | 235 | 1.1 |
| 6H | 055 | 197 | 1.0 |
| 7H | 140 | 221 | 1.0 |
| 8H | 343 | 204 | 1.0 |
| 9H | 177 | 226 | 1.4 |
| 10H | 252 | 264 | 0.9 |
| 11H | 007 | 149 | 0.5 |
| 12H | 035 | 154 | 0.6 |
| 13H | 308 | 338 | 0.2 |
| 14H | 346 | 205 | 0.9 |
| ^a -851E-1H | 260 | | |
| ^a 2H | 110 | | |
| ^a 3H | 300 | | |
| ^a 4H | 140 | | |
| ^a 5H | 300 | | |
| ^a 6H | 020 | | |
| ^a 7H | 350 | | |
| 8H | 190 | 350 | 1.2 |
| 9H | 012 | 018 | 1.5 |
| 10H | 111 | 000 | 0.8 |
| 11H | 254 | 349 | 1.6 |
| 12H | 075 | 025 | 0.9 |
| 13H | 269 | 360 | 1.3 |
| 14H | 075 | 013 | 0.5 |

^aSecondary orientation (SOR) angle is the value used to adjust average measured declination to 0° to 180° for normal or reversed chronozones, respectively, when no multishot orientation was available. For multishot orientation, the measured declination was corrected by adding to it the multishot azimuthal orientation and the local geomagnetic deviation (8.9°). Multishot azimuth values in () are considered to be erroneous, and for our interpretation, we used the SOR value in the following line.

Wykeham-Farrance vane shear device. Our methods of analyses are described in the “Explanatory Notes” chapter (this volume).

Two physical property measurements were determined for each section of the cores from Hole 851B. Cores from Hole 851E were sampled once per section. Index property samples were always taken at the same depth interval as the velocity measurements. No shear strength tests nor thermal conductivities were determined for sections from Hole 851E. Here, we describe the downhole distribution of the physical properties from Hole 851B, because we determined two index property values in each section of the cores from this hole, which thus provided us with the highest resolution profiles of any Leg 138 hole.

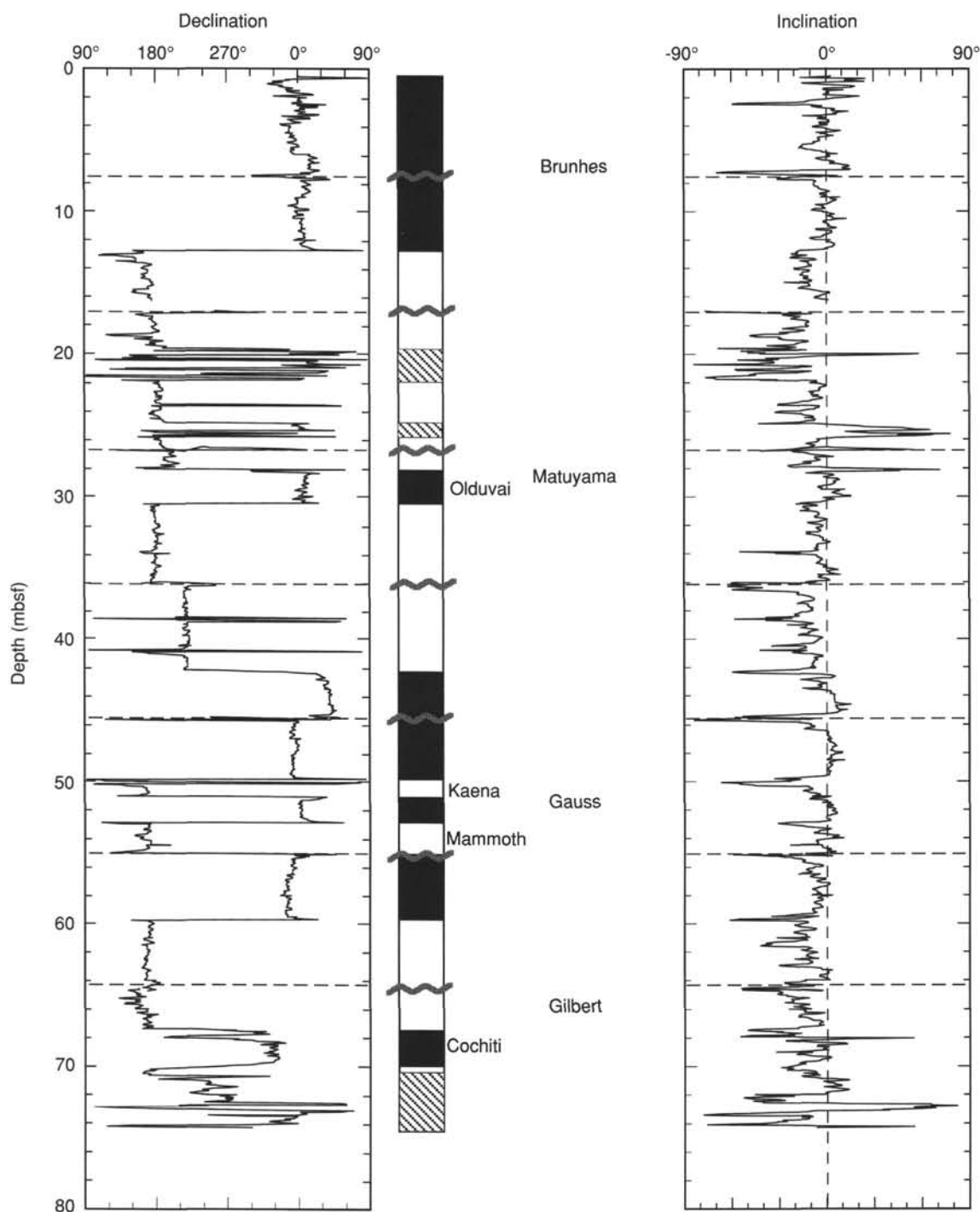


Figure 19. Declination and inclination profiles from the pass-through magnetometer, demagnetized at 15 mT, and identification of polarity chronozones in Hole 851B. Black = normal, white = reverse, hatched area = no data or no interpretation. Dashed line indicates core boundaries. Declinations have been rotated as described in Table 7.

Index Properties

Wet-bulk density values range from 1.24 to 1.76 g/cm³ and generally increase with depth (Fig. 38; Table 16, CD ROM, back pocket). Intervals of lower bulk densities occur at 130 to 150 and 220 to 280 mbsf.

Water content, expressed relative to dry weight (Fig. 39; Table 16, CD ROM, back pocket), varies between 252% and 52% and generally decreases downhole. Intervals having high water content are seen

between 130 and 150 mbsf and 225 and 294 mbsf. Porosity (the volumetric expression for water content) ranges between 58% and 87%, with a mean value near 75%. Porosity generally decreases with depth (Fig. 40; Table 16, CD ROM, back pocket), and its downhole variation is similar to that of water content.

Grain density (Fig. 41; Table 16, CD ROM, back pocket) varies between 2.27 and 2.76 g/cm³, with a mean value of 2.59 g/cm³. No downhole trend is evident in the data. Intervals having low grain

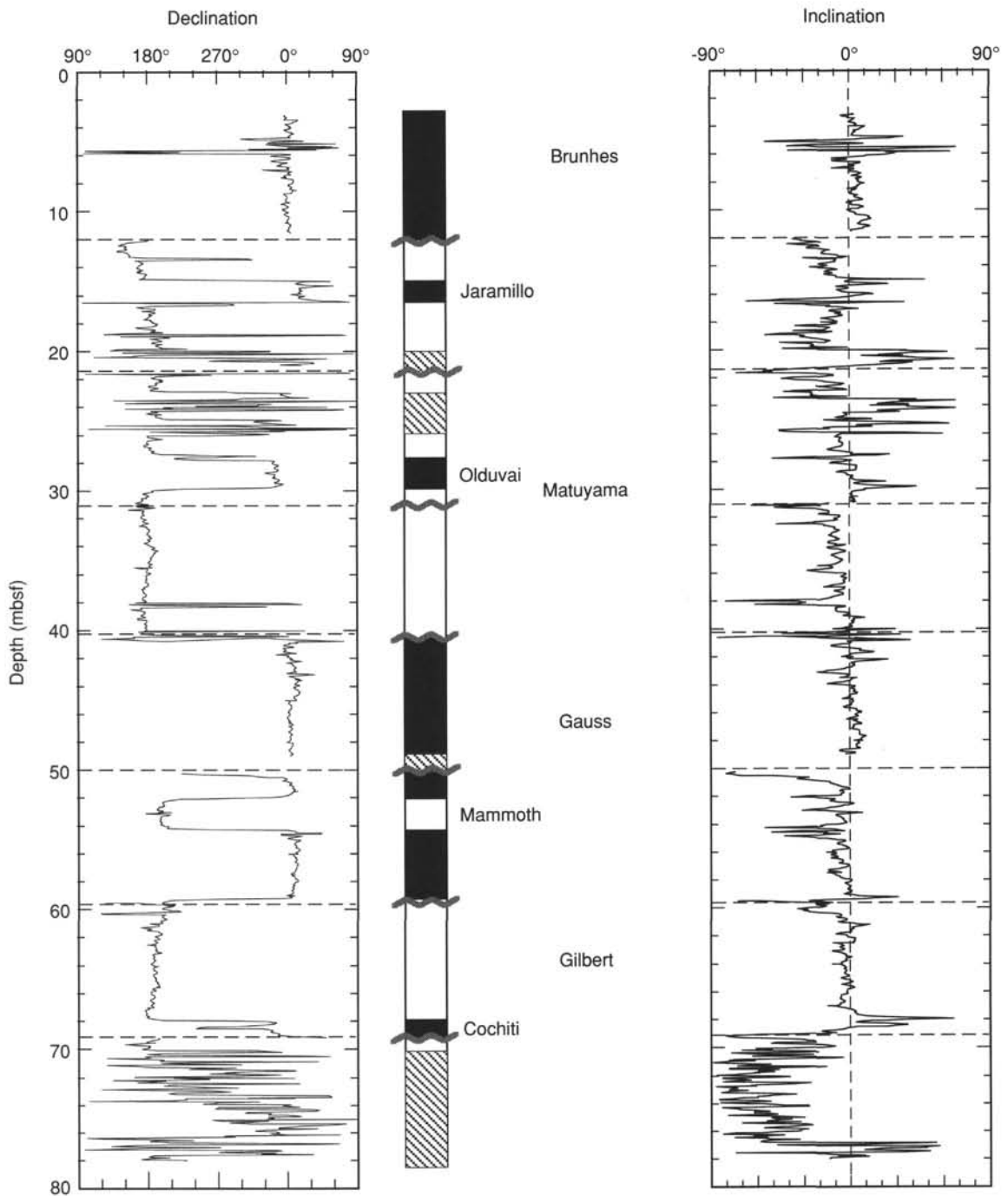


Figure 20. Declination and inclination profiles from the pass-through magnetometer, demagnetized at 15 mT, and identification of polarity chronozones in Hole 851C. Black = normal, white = reverse, hatched area = uninterpreted. Dashed line indicates core boundaries. Declinations have been rotated as described in Table 7.

densities can be seen between 89 and 155 mbsf and 225 to 294 mbsf. These depth intervals also are characterized by lower wet-bulk densities and high water contents.

Compressional-Wave Velocity

Compressional-wave velocity was measured perpendicular to bedding in split cores from Holes 851B and 851E. These measurements were performed for Cores 138-851B-1H through -17X and 138-851E-1H through -14H. Results of these velocity measurements are presented in Table 17 (CD ROM, back pocket) and graphically

illustrated in Figure 42. Compressional-wave velocity values range between 1502 and 1554 m/s and increase with depth below 30 mbsf, although the values are highly variable.

Shear Strength

Undrained shear strength was measured twice per section in Hole 851B in Cores 138-851B-1H through -15H using the Wykeham-Farrance vane shear device (see "Explanatory Notes" section, this volume). Values range between 9 and 110 kPa and increase with depth below seafloor (Fig. 43; Table 18, CD ROM, back pocket). A zone of

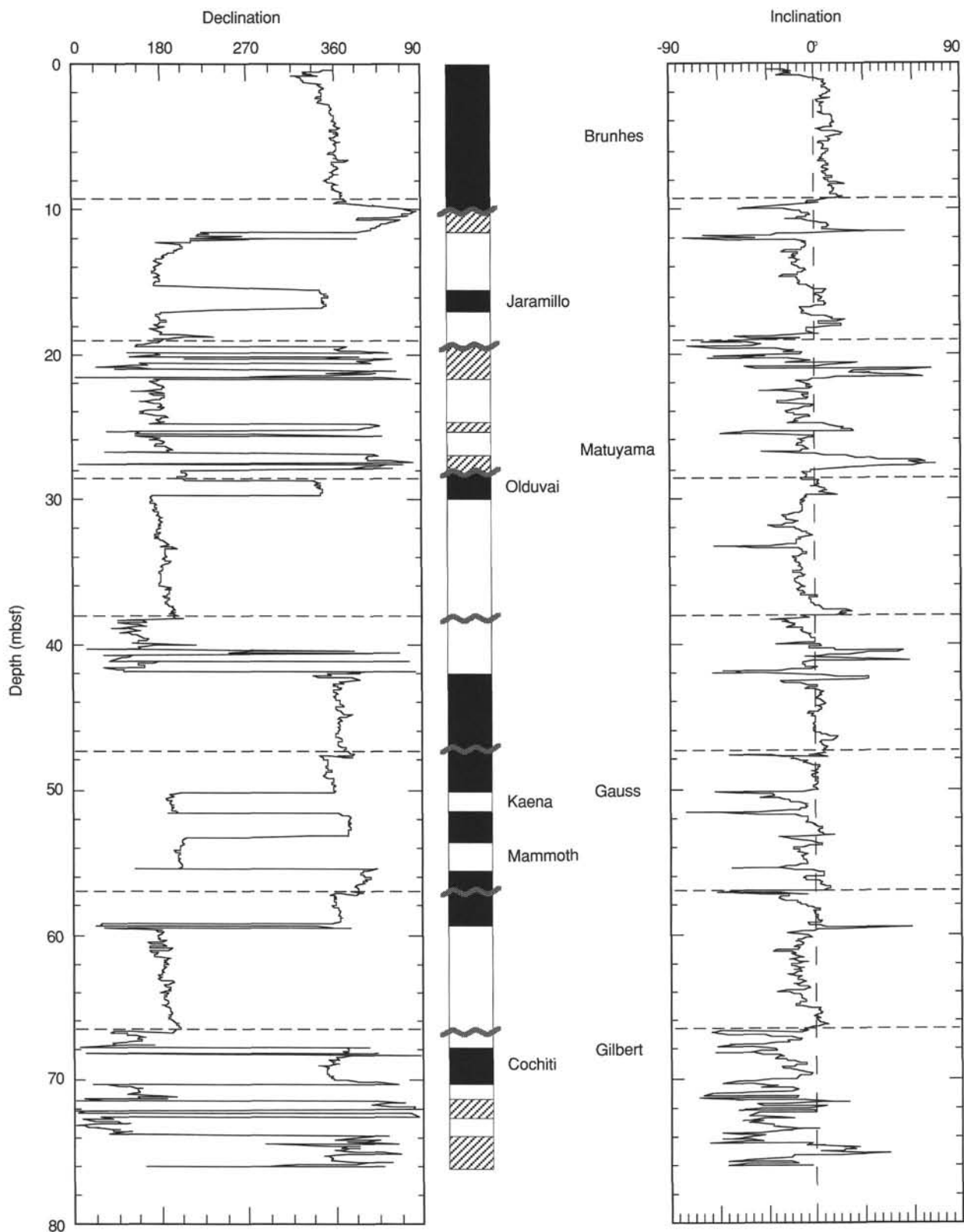


Figure 21. Declination and inclination profiles from the pass-through magnetometer, demagnetized at 15 mT, and identification of polarity chronozones in Hole 851E. Black = normal, white = reverse, hatched area = no data or no interpretation. Dashed lines indicate core boundaries. Declinations have been rotated as described in Table 7.

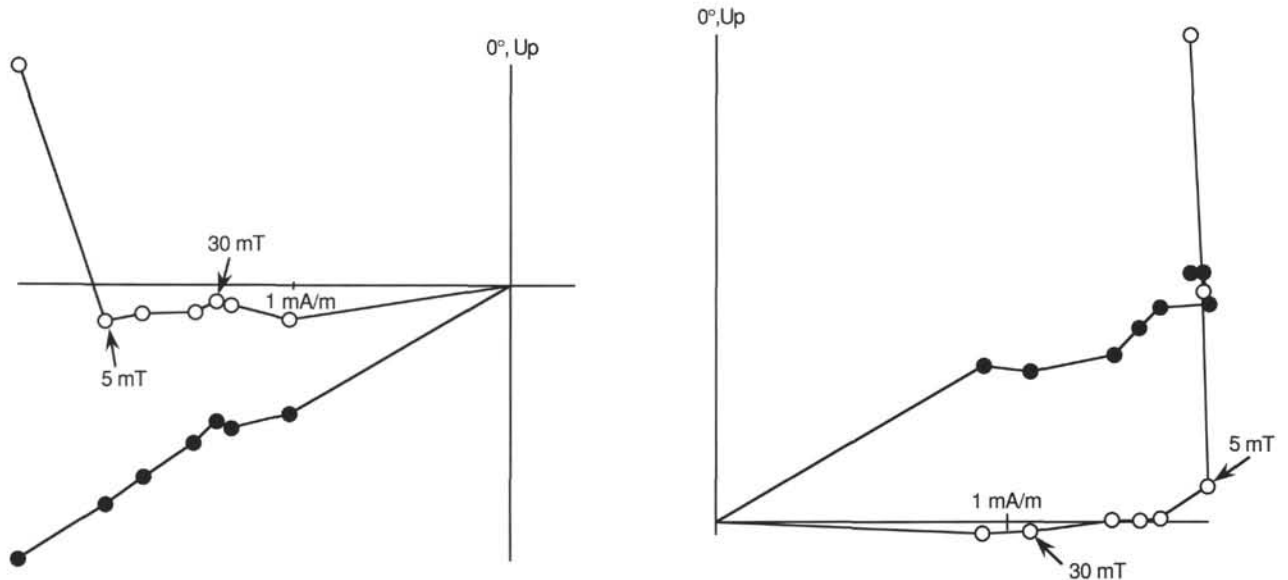


Figure 22. Vector projection demagnetization diagrams of two discrete samples at Site 851 showing the ubiquitous vertical upward overprint, which for these samples has been removed with AF demagnetization to 5 mT, exposing a stable characteristic remanence. Open circles denote projection onto horizontal (vertical) plane. Azimuthal orientation is with respect to the double fiducial line on the core liners.

high shear strength values (shear strength of 60 kPa) occurs between 52 and 110 mbsf.

Thermal Conductivity

Thermal conductivities were determined routinely for four sections (Sections 1, 3, 5, and 7) from each core at Hole 851B to a depth of 321 mbsf. Thermal conductivity values vary between 0.65 and 1.56 W/(m • K), with a mean value of 1.08 W/(m • K) (Fig. 44; Table 19, CD ROM, back pocket). Profiles for thermal conductivity generally mirror that of wet-bulk density and are inversely related to water content and porosity.

Relationships of Physical Properties to Lithology

The downhole distribution of physical properties at Site 851 is controlled by gravitational compaction processes and lithologic variation. Consolidation with depth, due to increasing overburden, results in a reduction of water content and porosity with concomitant increases in wet-bulk density, shear strength, and thermal conductivity. Superimposed on these downhole trends are large variations that resulted from changes (meter-scale to tens of meters) in lithology between calcareous- and siliceous-rich sediments (e.g., the intervals between 100 and 110 mbsf). These intervals are characterized by lower grain density and wet-bulk density, and higher porosity and water content than the more nannofossil-rich intervals. The interlocking nature of the siliceous tests results in a strong, more open, sediment framework at depth. The higher shear strength values measured in the uppermost siliceous-rich interval also attests to this increased framework strength.

DOWNHOLE MEASUREMENTS

Quality of Data

As in the majority of sites during Leg 138, the quality of the geophysical and geochemical logs at Site 851 is excellent. Two intervals, at 266 mbsf and from 272 to 275 mbsf, have anomalous density and far velocity values, respectively (Fig. 45). The absence of agreement for all but the middle maximum between the near and

far velocity logs suggests that the other maxima and minima are invalid and were probably caused by tool-related problems associated with the chert layers in this interval (see below). A density dropout at 266 mbsf is probably related to the presence of a ledge in the borehole, which is apparent in the caliper log (Fig. 45B).

The quality of the FMS log has been degraded as a result of failure of Pad 4, which sustained damage during the FMS run at Site 850 (see "Operations" section, this chapter and "Operations" section, "Site 850" chapter, this volume). No dips were calculated, and generation of dynamic images was not possible because of this failure. In addition, images in the interval from 90 to 140 mbsf are suspect because of large hole diameters and because two of the FMS pads failed to contact the borehole wall. With the exception of this interval, however, images produced by Pads 1 through 3 are good, and resistivity variations are generally correlative among the three pads. The depth intervals of the usable logging data are shown in Table 20.

Log Stratigraphic Units

We identified a single log unit at Site 851 that is composed of three subunits that have been distinguished by different trends of the various log parameters with depth.

Subunit 1A (63–205 mbsf; 3.6–8.0 Ma)

Log Subunit 1A is characterized by a fairly steady downhole velocity increase overprinted by cycles that correlate with patterns in density, resistivity, and Ca-yield. Density and resistivity values display cyclic variations on a scale of about 40 m, but exhibit no strong trends with depth (Table 21; Figs. 46 and 47). Trends of Ca-yield values in Subunit 1A resemble those in density and resistivity and display cyclicity, but no monotonic relationship with depth (Fig. 48). We identified four maxima in Ca-yield values (marked A through D in Fig. 48), laboratory-determined carbonate values (see "Organic Geochemistry" section, this chapter), and in calcareous microfossils (estimated from smear slides; see "Lithostratigraphy" section, this chapter) that occurred at approximately 4.3, 5.8, 6.5, and 7.5 Ma. These patterns are similar to those observed at other Leg 138 sites and

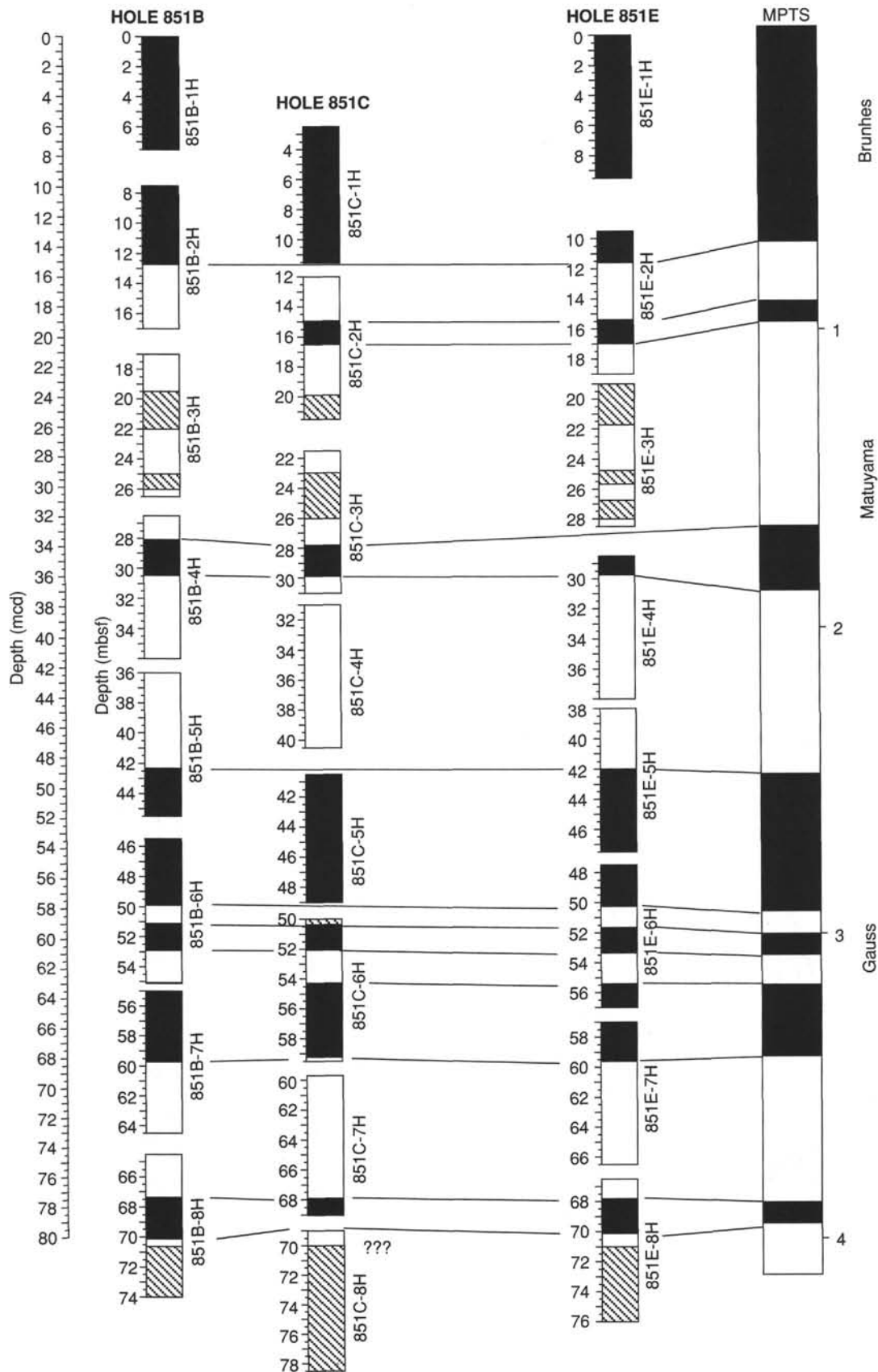


Figure 23. Magnetostatigraphic synthesis at Site 851. Depth ticks on individual cores are in meters below sea floor (mbsf). Cores are located at appropriate composite depth (mcd). Black zones indicate normal polarity; white zones indicate reverse polarity; hatched zones have not been interpreted. MPTS = magnetic polarity time scale.

Table 8. Reversal boundary depths from Site 851.

| Interval (cm) | Depth (mbsf) | Depth (mcd) | Interpretation | Age | Comments |
|------------------|--------------|-------------|------------------|------|--------------------|
| 138-851B-2H-4,75 | 12.75 | 15.10 | Brunhes/Matuyama | 0.73 | |
| 4H-2,10 | 28.10 | 33.50 | Olduvai (t) | 1.66 | |
| 4H-3,98 | 30.48 | 35.88 | Olduvai (o) | 1.88 | |
| 5H-5,30 | 42.30 | 48.60 | Matuyama/Gauss | 2.47 | |
| 6H-3,140 | 49.90 | 57.75 | Kaena (t) | 2.92 | Near section break |
| 6H-4,108 | 51.08 | 58.93 | Kaena (o) | 2.99 | |
| 6H-5,142 | 52.92 | 60.77 | Mammoth (t) | 3.08 | Near section break |
| 6H-7,60 | 55.10 | 62.95 | Mammoth (o) | 3.18 | |
| 7H-4,22 | 59.72 | 68.17 | Gauss/Gilbert | 3.40 | |
| 8H-2,140 | 67.40 | 77.30 | Cochiti (t) | 3.88 | Near section break |
| 8H-4,110 | 70.10 | 80.00 | Cochiti (o) | 3.97 | |
| -851C-2H-2,145 | 14.95 | 18.95 | Jaramillo (t) | 0.91 | |
| 2H-4,0 | 16.50 | 20.50 | Jaramillo (o) | 0.98 | Top of section |
| 3H-5,30 | 27.80 | 33.85 | Olduvai (t) | 1.66 | |
| 3H-6,85 | 29.85 | 35.90 | Olduvai (o) | 1.88 | |
| 6H-2,55 | 52.05 | 60.75 | Mammoth (t) | 3.08 | |
| 6H-3,130 | 54.30 | 63.00 | Mammoth (o) | 3.18 | |
| 6H-7,25 | 59.25 | 67.95 | Gauss/Gilbert | 3.40 | |
| 7H-6,95 | 67.95 | 77.55 | Cochiti (t) | 3.88 | |
| -851E-2H-1,70 | 11.58 | 15.08 | Brunhes/Matuyama | 0.73 | |
| 2H-5,05 | 15.43 | 18.93 | Jaramillo (t) | 0.91 | Top of section |
| 2H-6,10 | 16.98 | 20.48 | Jaramillo (o) | 0.98 | |
| 4H-1,125 | 29.75 | 35.95 | Olduvai (o) | 1.88 | |
| 5H-3,90 | 41.90 | 48.70 | Matuyama/Gauss | 2.47 | |
| 6H-2,125 | 50.25 | 57.85 | Kaena (t) | 2.92 | |
| 6H-3,110 | 51.60 | 59.20 | Kaena (o) | 2.99 | |
| 6H-4,135 | 53.35 | 60.95 | Mammoth (t) | 3.08 | |
| 6H-6,45 | 55.45 | 63.05 | Mammoth (o) | 3.18 | |
| 7H-2,110 | 59.60 | 68.20 | Gauss/Gilbert | 3.40 | |
| 8H-1,130 | 67.80 | 77.40 | Cochiti (t) | 3.88 | |
| 8H-3,80 | 70.30 | 79.90 | Cochiti (o) | 3.97 | |

(t) = termination; (o) = onset.

are thought to be related to changes in carbonate preservation (see below). A zone of low Si-yield values occurs from 136 mbsf to the base of Subunit 1A (Fig. 48). Although thin layers of lower Si-yield exist, the interval between 136 and 204 mbsf represents the thickest section of low Si-yield values at this site and corresponds to an interval of generally low abundances of siliceous microfossils (estimated from smear slides; see "Lithostratigraphy" section, this chapter).

Subunit 1B (205–277 mbsf; 8.0–10.4 Ma)

The boundary between log Subunits 1A and 1B is marked by sharp decreases in density, resistivity, and velocity. All three properties decrease slightly to a depth of 256 mbsf, where a 10-m-thick peak was observed in a physical property log (Figs. 46 and 47). The mean Ca-yield value in Subunit 1B is lower than those in Subunits 1A and 1C and also exhibits an abrupt decrease at the Subunit 1A/Subunit 1B boundary (Table 21; Fig. 48). An increase corresponding to those observed in the physical property logs occurs at 256 mbsf. Changes in Ca-yield are mirrored in the sum of foraminifer and nannofossil tests (estimated from smear slides; see "Lithostratigraphy" section, this chapter) and laboratory-determined carbonate contents (see "Organic Geochemistry" section, this chapter).

The base of Subunit 1B is a 9-m-thick zone (268–277 mbsf) of silica-rich sediments (2 m of diatom ooze overlain by 7 m of nannofossil ooze with gradually increasing silica content; see "Lithostratigraphy" section, this chapter). This zone is clearly evident in all the logs and is characterized by low density, resistivity, and velocity, and high porosity, H-yield, and PHIG (porosity values) (Figs. 46 and 47). Ca-yield values are relatively low (Fig. 48). Si-yield values poorly differentiate this silica-rich interval. A peak in Si-yield occurs at 273 mbsf, but Si-yield values are highly variable in this interval (Fig. 48). Si-yield values do not correlate well with estimates of siliceous microfossils throughout this hole (see below).

Chert, fragments of which were recovered in Holes 851B and 851E (see "Lithostratigraphy" section, this chapter), occurs in the middle of this silica-rich zone. In contrast to chert layers at previous Leg 138 sites (e.g., Sites 846, 847, and 850), however, this chert interval at Site 851 is not characterized by dramatic changes in log properties. Density and resistivity values are higher in the chert interval than in adjacent strata, but are low relative to measurements in most of the hole (Figs. 46 and 47).

Subunit 1C (277–320.1 mbsf; 10.4–10.9 Ma)

Log Subunit 1C is characterized by high mean values of density, resistivity, and velocity and high rates of increase with depth from the top of Subunit 1c to approximately 290 mbsf (Table 21; Figs. 46 and 47). Values reach maxima from 288 to 292 mbsf before leveling off (resistivity) or declining (density). Ca-yield values also increase in this subunit and reach a maximum at 290 mbsf, when these decrease slightly.

Lithologic Controls of Log Properties

Relative abundances of calcareous material in sediments strongly influence the physical properties at Site 851, as at previous Leg 138 sites. A plot of density vs. Ca-yield has a large amount of scatter, but shows that a positive relationship exists between the two properties (Fig. 49A). An inverse relationship exists between porosity (estimated from the neutron geochemistry tool) and Ca-yield (Fig. 49A). The most obvious changes in carbonate content, from relatively high values above 200 mbsf to lower values from approximately 200 to 280 mbsf, are associated with the log subunit boundaries (Fig. 48). Density, resistivity, and velocity values are relatively high in Subunit 1A, low in Subunit 1B, and increase with increasing carbonate content in Subunit 1C. In addition, correlations exist between trends of the three independent measures of carbonate content: log

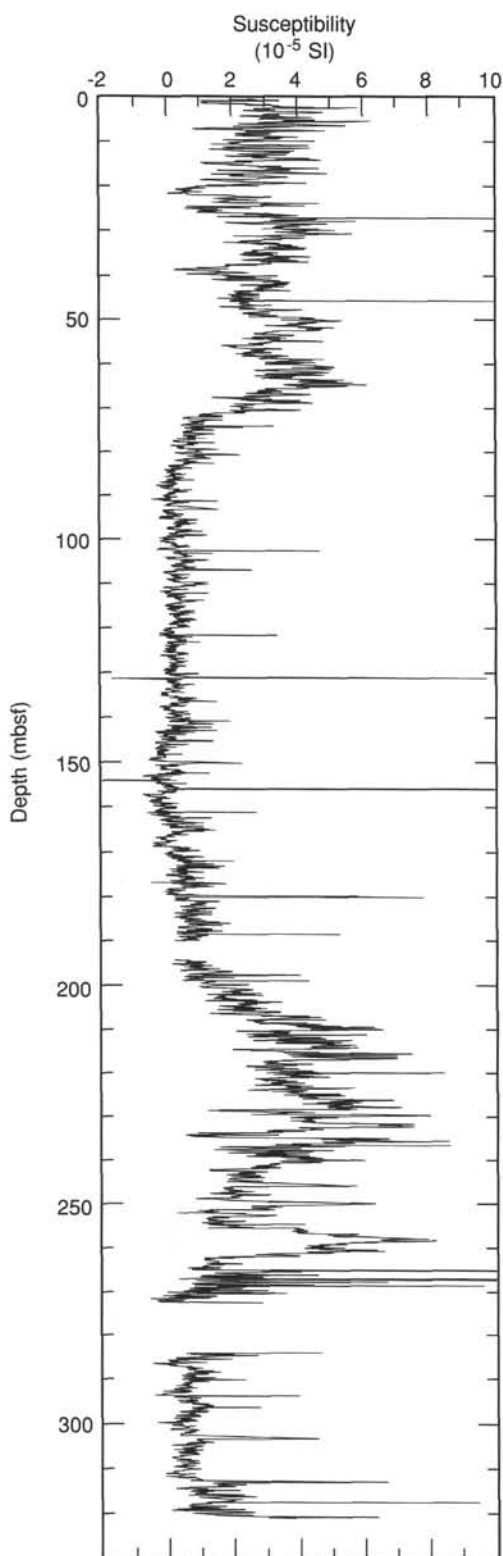


Figure 24. Susceptibility profile for the entire sedimentary section at Hole 851B, emphasizing the boundary at 70 mbsf and the susceptibility enhancement between 210 and 270 mbsf.

Ca-yield, laboratory-determined carbonate (Fig. 50A; see "Organic Geochemistry" section, this chapter), and estimates of calcareous microfossils (Fig. 50B; from smear slides; see "Lithostratigraphy" section, this chapter).

Other log geochemistry measurements match only laboratory data in their overall trends, however. For instance, although most maxima and minima in the trend of siliceous microfossils and clay contents (from smear slides; see "Lithostratigraphy" section, this chapter) correspond to peaks in the Si-yield logs, numerous differences between the two trends exist (Fig. 50C). Part of this difference may be a result of dissolution of the microfossils, which would not be quantified by estimates of smear-slide abundances. In addition, measurements of aluminum concentration should be related to clay content, having few other sources in these sediments, but no such relationship was observed (Fig. 51A). Similarly, correlations between clay abundance and concentrations of potassium and thorium, which are also associated with terrigenous material, are poor (Fig. 51B). We suspect that errors when estimating clay in the smear slides are major causes of these discrepancies, although the very low concentrations of aluminum, thorium, and potassium in the sediments also contribute to the poor correlations.

Cherts at Site 851

Chert fragments were recovered in Holes 851B and 851E at depths of approximately 275 mbsf, but no core was recovered over a 9-m interval below this level. The FMS image of the interval shows the existence of two separate layers of high-resistivity chert (white bands marked in Fig. 52), within a 9-m-thick stratum of low resistivity. The low resistivity zone is a silica-rich, high-porosity layer (see "Lithostratigraphy" section, this chapter).

Very high shallow-resistivity values (20 ohm-m) have marked the occurrence of chert layers at other Leg 138 sites. Although shallow-resistivity measurements at Site 851 are never greater than 1 ohm-m, these do clearly distinguish the two separate chert layers, whereas only a single high-resistivity layer is present in the intermediate-resistivity log, which averages over a wider depth interval (Fig. 53). Si-yield shows two fairly broad peaks centered at the depths of the two chert layers, which suggests that the upper layer is richer in Si. The two chert beds also are characterized by local minima in Ca-yield, maxima in estimated porosity, natural gamma-ray activity (Fig. 54), and Cl-yield. The relatively high gamma-ray values have been attributed primarily to high thorium, rather than uranium, concentrations (Fig. 54). The relatively high concentrations of thorium in the chert layers suggest that terrigenous sediment may have been incorporated into the chert layers at this site.

The thinness of the chert layers, higher shallow- vs. intermediate-resistivity values, and weak chemical and physical-property signatures suggest that the cherts at Site 851 are not laterally continuous and that the sediments have not been as strongly altered as those observed at other Leg 138 sites. Similarities in the chemistry of the interstitial waters above and below the cherts at Site 851 also suggest that the chert beds do not form so impermeable a barrier at this site. These thin chert layers may still be in the process of forming.

Paleoceanographic Significance

The four density maxima observed in Subunit 1A, as well as others deeper in Hole 851B, can be correlated to similar maxima at other Leg 138 sites (Fig. 46). These variations in density are roughly synchronous and generally occur at the same depths as peaks in Ca-yield values. Given the correlation between carbonate content and density (Mayer, 1991), the density log gives a first-order carbonate profile. The high carbonate

Table 9. Depths of top and bottom of each core in Site 851 in the composite depth section.

| Core | ODP depth (mbsf) | Core length (m) | Composite depth (mcd) | Δ (m) |
|-------------|------------------|-----------------|-----------------------|--------------|
| 138-851A-1H | 0-6.45 | 6.45 | 0-6.45 | 0.00 |
| -851B-1H | 0-7.58 | 7.58 | 0-7.58 | 0.00 |
| 2H | 7.50-17.17 | 9.67 | 9.85-19.52 | 2.35 |
| 3H | 17.00-27.10 | 10.10 | 21.15-31.25 | 4.15 |
| 4H | 26.50-36.41 | 9.91 | 31.90-41.81 | 5.40 |
| 5H | 36.00-45.89 | 9.89 | 42.30-52.19 | 6.30 |
| 6H | 45.50-55.60 | 10.10 | 53.35-63.45 | 7.85 |
| 7H | 55.00-65.04 | 10.04 | 63.45-73.49 | 8.45 |
| 8H | 64.50-74.54 | 10.04 | 74.40-84.44 | 9.90 |
| 9H | 74.00-84.14 | 10.14 | 84.40-94.54 | 10.40 |
| 10H | 83.50-93.46 | 9.96 | 95.45-105.41 | 11.95 |
| 11H | 93.00-103.01 | 10.01 | 106.15-116.16 | 13.15 |
| 12H | 102.50-112.64 | 10.14 | 117.50-127.64 | 15.00 |
| 13H | 112.00-122.19 | 10.19 | 127.80-137.99 | 15.80 |
| 14H | 121.50-131.37 | 9.87 | 138.65-148.52 | 17.15 |
| 15H | 131.00-140.89 | 9.89 | 149.35-159.24 | 18.35 |
| 16X | 140.50-150.00 | 9.50 | 159.05-168.55 | 18.55 |
| 17X | 150.10-159.87 | 9.77 | 173.60-183.37 | 23.50 |
| 18X | 159.80-169.49 | 9.69 | 188.25-197.94 | 28.45 |
| 19X | 169.40-179.03 | 9.63 | 199.15-208.78 | 29.75 |
| 20X | 179.10-188.93 | 9.83 | 215.05-224.88 | 35.95 |
| 21X | 188.30-197.14 | 8.84 | 227.65-236.49 | 39.35 |
| 22X | 197.50-207.29 | 9.79 | 236.85-246.64 | 39.35 |
| 23X | 207.10-216.87 | 9.77 | 252.05-261.82 | 44.95 |
| 24X | 216.80-226.56 | 9.76 | 262.90-272.66 | 46.10 |
| 25X | 226.40-236.19 | 9.79 | 275.50-285.29 | 49.10 |
| 26X | 236.10-245.25 | 9.15 | 288.90-298.05 | 52.80 |
| 27X | 245.80-255.68 | 9.88 | 300.65-310.53 | 54.85 |
| 28X | 255.50-265.14 | 9.64 | 311.40-321.04 | 55.90 |
| 29X | 265.10-272.83 | 7.73 | 323.50-331.23 | 58.40 |
| 30X | 274.80-274.80 | 0.00 | 333.20-333.20 | 58.40 |
| 31X | 284.00-293.96 | 9.96 | 342.40-352.36 | 58.40 |
| 32X | 293.60-302.94 | 9.34 | 353.85-363.19 | 60.25 |
| 33X | 303.20-333.13 | 9.93 | 367.15-377.08 | 63.95 |
| 34X | 312.90-321.49 | 8.59 | 378.45-387.04 | 65.55 |
| -851C-1H | 2.50-11.82 | 9.32 | 6.00-15.32 | 3.50 |
| 2H | 12.00-21.86 | 9.86 | 16.00-25.86 | 4.00 |
| 3H | 21.50-31.44 | 9.94 | 27.55-37.49 | 6.05 |
| 4H | 31.00-41.18 | 10.18 | 37.85-48.03 | 6.85 |
| 5H | 40.50-49.22 | 8.72 | 49.00-57.72 | 8.50 |
| 6H | 50.00-59.99 | 9.99 | 58.70-68.69 | 8.70 |
| 7H | 59.50-69.39 | 9.89 | 69.10-78.99 | 9.60 |
| 8H | 69.00-78.59 | 9.59 | 79.50-89.09 | 10.50 |
| 9H | 78.50-87.93 | 9.43 | 90.80-100.23 | 12.30 |
| 10H | 88.00-97.23 | 9.23 | 101.10-110.33 | 13.10 |
| 11H | 97.50-107.59 | 10.09 | 112.15-122.24 | 14.65 |
| 12H | 107.00-117.15 | 10.15 | 123.00-133.15 | 16.00 |
| 13H | 116.50-126.62 | 10.12 | 133.60-143.72 | 17.10 |
| 14H | 126.00-136.14 | 10.14 | 144.40-154.54 | 18.40 |
| -851D-1H | 0-10.10 | 10.10 | 0-10.10 | 0.00 |
| 2H | 9.50-19.50 | 10.00 | 11.50-21.50 | 2.00 |
| -851E-1H | 0-9.86 | 9.86 | 0-9.86 | 0.00 |
| 2H | 9.50-19.19 | 9.69 | 13.00-22.69 | 3.50 |
| 3H | 19.00-29.06 | 10.06 | 23.20-33.26 | 4.20 |
| 4H | 28.50-38.55 | 10.05 | 34.70-44.75 | 6.20 |
| 5H | 38.00-48.12 | 10.12 | 44.80-54.92 | 6.80 |
| 6H | 47.50-57.61 | 10.11 | 55.10-65.21 | 7.60 |
| 7H | 57.00-67.10 | 10.10 | 65.60-75.70 | 8.60 |
| 8H | 66.50-76.39 | 9.89 | 76.10-85.99 | 9.60 |
| 9H | 76.00-86.10 | 10.10 | 87.05-97.15 | 11.05 |
| 10H | 85.50-95.63 | 10.13 | 97.50-107.63 | 12.00 |
| 11H | 95.00-105.13 | 10.13 | 108.30-118.43 | 13.30 |
| 12H | 104.50-114.61 | 10.11 | 118.95-129.06 | 14.45 |
| 13H | 114.00-124.06 | 10.06 | 130.30-140.36 | 16.30 |
| 14H | 123.50-133.68 | 10.18 | 140.20-150.38 | 16.70 |
| 15X | 133.00-141.94 | 8.94 | 149.40-158.34 | 16.40 |
| 16X | 139.00-147.13 | 8.13 | 159.80-167.93 | 20.80 |

Table 9 (continued).

| Core | ODP depth (mbsf) | Core length (m) | Composite depth (mcd) | Δ (m) |
|------|------------------|-----------------|-----------------------|--------------|
| 17X | 145.00-154.75 | 9.75 | 168.50-178.25 | 23.50 |
| 18X | 154.70-164.40 | 9.70 | 182.40-192.10 | 27.70 |
| 19X | 164.30-173.75 | 9.45 | 194.50-203.95 | 30.20 |
| 20X | 173.90-183.61 | 9.71 | 208.10-217.81 | 34.20 |
| 21X | 183.10-190.11 | 7.01 | 224.45-231.46 | 41.35 |
| 22X | 192.30-199.68 | 7.38 | 236.20-243.58 | 43.90 |
| 23X | 201.90-211.69 | 9.79 | 243.70-253.49 | 41.80 |
| 24X | 211.60-221.47 | 9.87 | 258.30-268.17 | 46.70 |
| 25X | 221.20-230.98 | 9.78 | 270.30-280.08 | 49.10 |
| 26X | 230.90-240.71 | 9.81 | 284.00-293.81 | 53.10 |
| 27X | 240.60-250.43 | 9.83 | 296.20-306.03 | 55.60 |
| 28X | 250.30-260.17 | 9.87 | 307.60-317.47 | 57.30 |
| 29X | 259.90-268.92 | 9.02 | 320.40-329.42 | 60.50 |
| 30X | 269.60-271.14 | 1.54 | 331.10-332.64 | 61.50 |
| 31X | 279.30-288.13 | 8.83 | 339.20-348.03 | 59.90 |
| 32X | 288.50-296.90 | 8.40 | 349.90-358.30 | 61.40 |
| 33X | 298.10-307.11 | 9.01 | 361.50-370.51 | 63.40 |
| 34X | 307.80-317.34 | 9.54 | 371.40-380.94 | 63.60 |
| 35X | 317.40-318.14 | 0.74 | 381.00-381.74 | 63.60 |

Note: See text for details about composite depth sections.

contents have several possible origins: increased productivity, decreased dissolution, decreased dilution by siliceous microfossils and/or terrigenous material, or some combination of these phenomena. In addition, several density minima correspond to seismic reflectors identified by Mayer et al. (1985). Specifically, the interval between carbonate peaks A and B corresponds to the green reflector; the brown reflector occurs between peaks C and D (Fig. 46). The purple reflector has been marked by very low carbonate contents (Mayer et al., 1985) and is represented at Site 851 by the interval of silica-rich sediments at the base of Subunit 1B.

Comparison of Logs to Laboratory Values

Log density values in Subunit 1A generally are lower than GRAPE values at equivalent depths. Below the Subunit 1A/Subunit 1B boundary, however, most GRAPE values are lower than the log densities (Fig. 55). The average log density minus GRAPE density value in Subunit 1C is near zero. Density differences of log-to-GRAPE and gravimetric measurements show similar downhole variations, but the log density minus gravimetric density trend is offset to higher, generally positive, values throughout the hole (Fig. 55). Average values of density difference correlate, to a first approximation, with estimates of siliceous microfossils and exhibit a negative relationship to abundances of calcareous microfossils (estimated from smear slides, see "Lithostratigraphy" section, this chapter). We observed these same relationships previously (e.g., see "Downhole Measurements" section, "Site 849" chapter, this volume) and attributed them to a higher degree of *in-situ* to laboratory rebound that occurs in the high silica-rich sediments relative to carbonate-rich material. Further evidence of this relationship was observed in the silica-rich zone at the base of Subunit 1B where the delta density values are greatest in the hole (Fig. 55).

SEISMIC STRATIGRAPHY

Modeling Procedures

Synthetic seismograms were generated from velocity and density models for Site 851 to correlate reflectors in the seismic section to stratigraphic changes.

A density model was created by merging laboratory density with *in-situ* logging density. Depth-shifted logging density (by correlation

Table 10. Control points for sedimentation rates.

| Composite depth (mcd) | Sediment, rate (m/m.y.) | Age (Ma) | Remarks |
|-----------------------|-------------------------|----------|---|
| 0 | | 0 | Core top |
| 15.09 | 20.7 | 0.73 | B Brunhes Chron |
| 18.95 | 21.4 | 0.91 | T Jaramillo Subchron |
| 20.48 | 21.9 | 0.98 | B Jaramillo Subchron |
| 33.7 | 17.4 | 1.66 | T Olduvai Subchron |
| 35.91 | 10.3 | 1.88 | B Olduvai Subchron |
| 48.65 | 21.6 | 2.47 | B Matuyama Chron |
| 57.85 | 20.3 | 2.92 | T Kaena Subchron |
| 59.06 | 17.9 | 2.99 | B Kaena Subchron |
| 60.83 | 19.4 | 3.08 | T Mammoth Subchron |
| 63.0 | 21.7 | 3.18 | B Mammoth Subchron |
| 68.1 | 23.2 | 3.40 | B Gauss Chron |
| 77.35 | 19.3 | 3.88 | T Cochiti Subchron |
| 79.95 | 28.9 | 3.97 | B Cochiti Subchron |
| 97.4 | 25.3 | 4.66 | B <i>Ceratolithus rugosus</i> |
| 116.47 | 59.6 | 4.98 | T <i>Discoaster quinqueramus</i> |
| 168.0 | 46.0 | 6.1 | B <i>Thalassiosira praeconvexa</i> |
| 199.7 | 48.8 | 6.75 | B <i>Nitschia miocenica</i> |
| 226.39 | 34.2 | 7.5 | B <i>Discoaster berggreni</i> |
| 315.0 | 36.4 | 9.94 | T <i>Coccolithus miopelagicus</i> |
| 363.19 | 51.0 | 10.9 | T <i>Coscinodiscus guigas</i> var. and B <i>Hemidiscus cuneiformis</i> (see text) |

T = top; B = bottom.

with the Hole 851B GRAPE density) was used over the interval 74.1 to 312.0 m (72.8–307.6 mbsf) (see “Downhole Measurements” section, this chapter). Over the interval 0 to 72.8 mbsf, a 10-point boxcar-filtered GRAPE density from Hole 851B was merged with the depth-shifted logging density after removal of data from 44.0 to 44.5 mbsf caused by core disturbance. After we plotted the GRAPE and logging density vs. depth (mbsf) over the interval 70 to 150 mbsf (Fig. 56), we found that the GRAPE densities are $\sim 0.05 \text{ g/cm}^3$ greater than the log densities. Thus, the GRAPE density values were reduced by 0.05 g/cm^3 prior to splicing. Beyond 307.6 mbsf to the depth of basement (320.5 mbsf), we used a constant density equal to the log density at 409.5 mbsf (1.58 g/cm^3).

A velocity model was created in a similar manner as just described. For 62.0 to 299.2 mbsf, we used a depth-shifted logging velocity. To fill a gap in the upper part of the section, we corrected laboratory velocity collected with the DSV to *in-situ* conditions for changes of sound speed as a function of temperature and pressure. Again, the temperature gradient of $^{\circ}\text{C/km}$ and bottom-water temperature from Site 849 were used because of problems with the downhole temperature tool at the site. For 299.2 to 320.5 mbsf, we used a constant velocity equal to the final log velocity (1744 m/s).

The accuracy of the traveltimes-to-depth conversion was evaluated by our generating synthetic seismograms and subsequently comparing them with the seismic record collected over the site. Synthetic seismograms were generated using the above merged velocity and density data. These data were resampled at a 1-ms sample interval (approximately 60 cm) and then used to calculate acoustic impedance and reflection coefficients and, finally, a synthetic seismogram. Density and velocity values typical of basalt (2.5 g/cm^3 and 3000 m/s, respectively) were added at the basement depth to generate a basement reflector in the synthetic seismogram. The model we used to generate the synthetic seismograms, described by Mayer et al. (1985), assumes plane waves, no multiples, and no signal attenuation. The final synthetic seismogram was filtered from 70 to 250 Hz, the same filter parameters as the field record collected during the Site 851 seismic survey.

Results

A comparison of the synthetic seismogram with the seismic profile collected at Site 851 shows a good match between the two (Fig. 57), which suggests that our traveltimes-to-depth conversion was fairly accurate.

Given an acceptable velocity model, the origin of some of the reflectors at Site 851 can be analyzed. We emphasize that these are preliminary results that will be undoubtedly modified after more careful analysis. We identified 14 major reflectors or reflector packages. These reflectors were selected on the basis of amplitude and lateral coherency in the seismic record in the immediate area of Site 851. We measured the two-way traveltime on the synthetic seismogram of the top and bottom of each reflector, and by using the assumed velocity model, we were able to determine the depth range of each reflector.

Our velocity, density, and acoustic impedance models were compared to depth ranges calculated from traveltimes to determine any changes in physical properties that might have caused the selected seismic reflectors. Within each depth range, a large change in density and/or velocity can be associated with each reflector (Fig. 58). Reflectors for the upper 110 m (reflectors 1 through 7) are solely related to large changes in density. Beyond 110 m, the reflectors are caused by synchronous, large fluctuations in velocity and density, although the amplitude of the density fluctuations, in general, is greater. Depths (synthetic, mbsf, and mcd) and ages (based on magnetostratigraphy and biostratigraphy of Site 851, see “Sedimentation Rates” section, this chapter) of these reflectors are presented in Table 22. A detailed understanding of the lithologic, biostratigraphic, and, ultimately, the paleoceanographic significance of these events must await shore-based studies at this time.

SUMMARY AND CONCLUSIONS

Site 851 is the fourth site drilled along the western transect of the area selected for Leg 138. This transect, situated along 110°W , was designed to sample the various elements of the equatorial circulation system in an area far removed from the influence of the eastern boundary of the Pacific Ocean. The transect also serves as the eastern end-member of a series of studies (Legs 85 and 130) aimed at understanding the regional and global responses of the equatorial Pacific Ocean to changes in climate. The present location of Site 851 is at the northern edge of the westward-flowing SEC, and thus the site was selected to provide the latest Neogene history of the oceanic conditions within this highly productive region.

Site 851 is located about 860 km west of the East Pacific Rise on crust generated about 11 to 12 Ma. The backtrack path of the site is straightforward and is constrained only by the movement of the

Table 11. Interstitial-water geochemical data for Holes 851A and 851B.

| Core, section, interval (cm) | Depth (mbsf) | pH | Salinity | Chloride (mM) | Sodium (mM) | Alkalinity (mM) | Sulfate (mM) | Magnesium (mM) | Calcium (mM) | Potassium (mM) | Strontium (μ m) |
|------------------------------|--------------|------|----------|---------------|-------------|-----------------|--------------|----------------|--------------|----------------|----------------------|
| 138-851A-1H-1, 135-140 | 1.4 | 7.09 | 35.0 | 556 | 483 | 2.953 | 27.31 | 53.43 | 10.49 | 10.9 | 88 |
| 1H-4, 135-140 | 5.9 | 7.48 | 35.0 | 557 | 483 | 3.020 | 26.76 | 53.23 | 10.45 | 11.1 | 86 |
| 851B-3H-6, 145-150 | 26.0 | 7.25 | 35.5 | 561 | 488 | 3.103 | 28.11 | 53.99 | 10.65 | 11.3 | 96 |
| 6H-6, 145-150 | 54.5 | 7.28 | 35.8 | 564 | 489 | 3.252 | 26.98 | 53.87 | 10.61 | 11.0 | 101 |
| 9H-6, 145-150 | 83.0 | 7.82 | 35.8 | 564 | 490 | 3.555 | 26.20 | 52.77 | 10.50 | 10.7 | 109 |
| 12H-6, 145-150 | 111.5 | 7.19 | 35.5 | 562 | 487 | 3.585 | 26.41 | 53.47 | 10.61 | 10.9 | 129 |
| 15H-6, 145-150 | 140.0 | 7.24 | 36.0 | 559 | 484 | 3.745 | 26.19 | 53.29 | 10.62 | 10.9 | 140 |
| 18X-4, 145-150 | 165.8 | 7.07 | 36.5 | 560 | 485 | 3.840 | 26.39 | 53.15 | 10.60 | 10.6 | 142 |
| 21X-5, 142-150 | 195.8 | 7.06 | 35.5 | 558 | 482 | 3.727 | 25.77 | 53.54 | 10.45 | 11.0 | 160 |
| 24X-6, 142-150 | 225.8 | 7.13 | 35.5 | 559 | 486 | 3.509 | 26.76 | 52.71 | 10.48 | 11.5 | 180 |
| 27X-6, 142-150 | 254.8 | 7.18 | 35.2 | 561 | 487 | 3.511 | 26.71 | 53.16 | 10.76 | 11.0 | 184 |
| 31X-6, 144-150 | 293.0 | 7.15 | ** | 559 | 484 | 3.561 | 26.09 | 52.98 | 10.37 | 10.7 | 146 |
| 32X-4, 142-150 | 299.6 | 7.17 | 36.0 | 561 | 488 | 3.094 | 27.46 | 53.53 | 10.55 | 10.6 | 136 |
| 33X-5, 142-150 | 310.7 | 7.11 | 35.8 | 558 | 485 | 2.956 | 27.30 | 53.29 | 10.62 | 10.5 | 115 |
| 34X-3, 142-150 | 317.4 | 7.23 | 35.8 | 559 | 487 | 2.544 | 27.99 | 53.52 | 10.32 | 10.2 | 102 |

Pacific Plate. Poles of rotation of the Pacific Plate have been estimated based on traces of hot spots (Duncan and Claque, 1985) and also by using the age distribution of sediments from DSDP sites along the equatorial sediment bulge (van Andel et al., 1975; see Fig. 2). Depending on which of these rotation schemes is used, the equatorial crossing of Site 851 can differ by as much as 2 m.y. We present the results of van Andel et al.'s (1975) rotation in Figure 2 and Table 23; however, a more detailed analysis of the coring and paleomagnetic results from all Leg 138 sites may help to refine these rotation schemes.

From an original ridge crest depth of approximately 2800 m, the site has subsided to its present depth of 3772 m and, in doing so, has intercepted a regionally and temporally variable lysocline. Throughout its history, Site 851 has existed above the CCD. The combination of triple APC and double XCB coring in conjunction with real-time monitoring of continuous core logs (GRAPE, susceptibility, and color

reflectance) assured us an almost continuous recovery of a 320-m-thick section. The sedimentary sequence spans the interval from the uppermost middle Miocene to the Pleistocene and can be described as a single lithological unit that is composed of varying mixtures of foraminifer nannofossil ooze and diatom nannofossil ooze.

The pattern of sedimentation at Site 851 is typical of pelagic sediments within this region of the equatorial Pacific Ocean. The first sediment to accumulate above the newly formed Site 851 was a nannofossil ooze that contained a substantial component of iron-oxides and clays. Initial sedimentation rates at the site were about 50 m/m.y. As with many sites in this equatorial region, sedimentation rates decreased after 10 Ma (Fig. 59). Sedimentation rates during the time interval from 10 to 8 Ma were about 35 m/m.y. This rate is higher than that of Site 849, which should have been south of the equatorial divergence region at this time, but about the same

Table 13. Duplicate analyses of percentages of CaCO₃ in samples from Site 851.

| Core, section, interval (cm) | ODP depth (mbsf) | Composite depth (mcd) | First run CaCO ₃ (%) | Second run CaCO ₃ (%) | Absolute value of CaCO ₃ (difference) |
|------------------------------|------------------|-----------------------|---------------------------------|----------------------------------|--|
| 138-851B-4H-3, 117-119 | 30.68 | 36.08 | 59.02 | 59.75 | 0.73 |
| 7H-4, 102-104 | 60.53 | 68.98 | 64.97 | 63.08 | 1.89 |
| 7H-5, 104-106 | 62.05 | 70.50 | 85.43 | 85.25 | 0.18 |
| 7H-6, 102-104 | 63.53 | 71.98 | 62.62 | 63.08 | 0.46 |
| 11H-2, 33-35 | 94.84 | 107.99 | 82.50 | 81.08 | 1.42 |
| 11H-2, 104-106 | 95.55 | 108.70 | 56.08 | 56.17 | 0.08 |
| 13H-2, 103-105 | 114.54 | 130.34 | 64.30 | 64.25 | 0.05 |
| 16X-5, 102-104 | 147.53 | 166.08 | 56.50 | 57.00 | 0.50 |
| 18X-1, 100-102 | 160.81 | 189.26 | 67.90 | 68.92 | 1.01 |
| 20X-1, 100-102 | 180.11 | 216.06 | 56.42 | 55.92 | 0.50 |
| 25X-1, 100-102 | 227.41 | 276.51 | 20.12 | 20.58 | 0.46 |
| 25X-5, 98-100 | 233.39 | 282.49 | 30.26 | 31.00 | 0.74 |
| 26X-2, 100-102 | 238.61 | 291.41 | 57.09 | 56.67 | 0.43 |
| 27X-2, 100-102 | 248.31 | 303.16 | 36.77 | 35.71 | 1.06 |
| 27X-3, 100-102 | 249.81 | 304.66 | 58.26 | 59.20 | 0.94 |
| 27X-4, 100-102 | 251.31 | 306.16 | 21.50 | 22.42 | 0.91 |
| 28X-1, 100-102 | 256.51 | 312.41 | 74.11 | 72.70 | 1.41 |
| 28X-2, 100-102 | 258.01 | 313.91 | 72.61 | 71.75 | 0.86 |
| 29X-2, 100-102 | 267.61 | 326.01 | 53.58 | 54.66 | 1.08 |
| 29X-5, 100-102 | 272.11 | 330.51 | 11.65 | 12.17 | 0.51 |
| 31X-2, 99-101 | 286.50 | 344.90 | 35.71 | 35.50 | 0.21 |
| 31X-6, 96-98 | 292.47 | 350.87 | 68.16 | 68.65 | 0.49 |
| 32X-2, 100-102 | 296.11 | 356.36 | 85.17 | 86.53 | 1.35 |
| 33X-1, 100-102 | 304.21 | 368.16 | 67.64 | 65.83 | 1.80 |
| 34X-6, 8-10 | 320.49 | 386.04 | 79.05 | 79.86 | 0.81 |
| Average | | | | | 0.80 |

Note: The average difference between the original and the duplicate analysis was 0.8% for percentage of CaCO₃. The average values of the original and the duplicate analysis are reported in Table 12.

Table 11 (continued).

| Lithium (μ m) | Silica (μ m) | Ammonia (μ m) |
|-----------------------|----------------------|-----------------------|
| 27.4 | 699 | 13 |
| 25.7 | 664 | 18 |
| 23.3 | 748 | 49 |
| 22.3 | 783 | 52 |
| 20.0 | 796 | 74 |
| 16.4 | 864 | 77 |
| 12.9 | 1021 | 96 |
| 11.0 | 1029 | 101 |
| 9.6 | 1052 | 93 |
| 9.5 | 1077 | 61 |
| 9.9 | 1031 | 53 |
| 15.6 | 927 | 21 |
| 18.2 | 905 | 12 |
| 23.4 | 854 | <10 |
| 28.7 | 758 | <10 |

or possibly lower than the nearest southerly site, Site 850. Based on van Andel et al.'s pole rotation for the Pacific Plate, Site 850 would have been a little more than a degree from the equator during this time period (Table 23). This interval of reduced sedimentation rate is characterized by increased dissolution of calcium carbonate and coincides with a similar event seen at all Leg 138 sites; the interval may represent a major dissolution event within the Pacific Ocean. Thus, the record we see is a complicated interplay of large-scale temporal changes in ocean chemistry superimposed on more local responses to surface current regimes.

At about 7 Ma, an increase occurred in sedimentation rates to about 65 m/m.y., which is reflected in an increase in MARs of calcium

carbonate, organic carbon, and noncarbon material (see Fig. 36). As at other sites drilled during Leg 138, the latest Miocene and early Pliocene were marked by high sedimentation rates, although not as high as previous sites drilled along the 110°W transect. While these rates are relatively high, they are about 40% less than those recorded at Sites 849 and 850. During the Pliocene and Pleistocene, sedimentation rates decreased to a relatively constant 20 m/m.y. Again, this decrease is paralleled by decreases at more southerly sites, but as expected from productivity gradients in the present-day Pacific Ocean, recent sedimentation rates at Site 851 are less than those estimated for Sites 850 and 849.

In many aspects, Site 851 continues the trends in sediment, pore-water, and physical gradients defined along the 110°W transect. Sedimentation rates are relatively high, but the lower accumulation rates of organic carbon are reflected in less reducing pore waters, better preservation of calcium carbonate, and the presence of a stable magnetic signal for at least the last 4 m.y. This combination is unique and should make Site 851 a key record for high-resolution paleoceanographic studies along the 110°W transect.

REFERENCES

- Baker, P. A., 1986. Pore water chemistry of carbonate-rich sediments, Lord Howe Rise, Southwest Pacific Ocean. In Kennett, J. P., von der Borch, C. C., et al., *Init. Repts. DSDP, 90*; Washington (U.S. Govt. Printing Office), 1249–1256.
- Baker, P. A., Gieskes, J. M., and Elderfield, H., 1982. Diagenesis of carbonates in deep-sea sediments—evidence from Sr/Ca ratios and interstitial dissolved Sr^{2+} data. *J. Sediment. Petrol.*, 52:71–82.
- Duncan, R. A., and Clague, D., 1985. Pacific plate motion is recorded by linear volcanic chains. In Nairn, A.E.M., Stehli, F. G., and Uyeda, U. (Eds.), *The Ocean Basins and Margins* (Vol. 7A); New York (Plenum), 89–121.
- Elderfield, H., and Gieskes J. M., 1982. Sr isotopes in interstitial waters of marine sediments from Deep Sea Drilling Project cores. *Nature*, 333:493–497.

Table 14. Average values of sedimentary parameters calculated over time intervals defined by chronostratigraphic levels.

| Composite depth (mcd) | Age (Ma) | Mean CaCO_3 (%) | Mean C_{org} (%) | Sed. rate (m/m.y.) | Mean DBD (g/cm^3) | Mean Bulk MAR ($\text{g}/\text{cm}^2/\text{k.y.}$) | Mean CaCO_3 MAR ($\text{g}/\text{cm}^2/\text{k.y.}$) | Mean Non- CaCO_3 MAR ($\text{g}/\text{cm}^2/\text{k.y.}$) | Mean C_{org} MAR ($\text{mg}/\text{cm}^2/\text{k.y.}$) |
|-----------------------|----------|--------------------------|----------------------------------|--------------------|-------------------------------------|--|---|--|--|
| 12.10 | 0.73 | 84.10 | 0.05 | 16.58 | 0.61 | 1.01 | 0.85 | 0.16 | 0.46 |
| 18.95 | 0.91 | 83.97 | 0.08 | 38.06 | 0.62 | 2.37 | 1.99 | 0.38 | 1.80 |
| 20.50 | 0.98 | | | 22.14 | | | | | |
| 33.70 | 1.66 | 78.82 | 0.08 | 19.41 | 0.55 | 1.06 | 0.84 | 0.23 | 0.83 |
| 35.96 | 1.88 | 65.57 | | 10.27 | 0.43 | 0.44 | 0.29 | 0.15 | |
| 48.70 | 2.47 | 77.60 | | 21.59 | 0.57 | 1.24 | 0.96 | 0.28 | |
| 57.83 | 2.92 | 78.37 | 0.12 | 20.29 | 0.59 | 1.20 | 0.94 | 0.26 | 1.43 |
| 59.08 | 2.99 | 70.92 | | 17.86 | 0.51 | 0.91 | 0.65 | 0.26 | |
| 60.83 | 3.08 | 68.07 | | 19.44 | 0.47 | 0.91 | 0.62 | 0.29 | |
| 63.00 | 3.18 | 85.26 | | 21.70 | 0.67 | 1.45 | 1.24 | 0.21 | |
| 68.10 | 3.40 | 78.92 | 0.04 | 23.18 | 0.67 | 1.55 | 1.23 | 0.33 | 0.61 |
| 77.35 | 3.88 | 77.30 | 0.07 | 19.27 | 0.68 | 1.31 | 1.01 | 0.30 | 0.95 |
| 79.85 | 3.97 | 80.23 | | 27.78 | 0.68 | 1.89 | 1.52 | 0.37 | |
| 97.40 | 4.66 | 77.86 | 0.11 | 25.43 | 0.70 | 1.79 | 1.39 | 0.40 | 1.95 |
| 116.47 | 4.98 | 73.64 | 0.16 | 59.59 | 0.66 | 3.95 | 2.91 | 1.04 | 6.27 |
| 155.60 | 6.10 | 75.99 | 0.12 | 34.94 | 0.72 | 2.51 | 1.91 | 0.60 | 3.09 |
| 199.70 | 6.75 | 72.74 | 0.11 | 67.85 | 0.72 | 4.90 | 3.56 | 1.34 | 5.50 |
| 225.38 | 7.50 | 69.03 | 0.24 | 34.24 | 0.66 | 2.26 | 1.56 | 0.70 | 5.46 |
| 314.23 | 9.94 | 61.70 | 0.07 | 36.41 | 0.64 | 2.32 | 1.43 | 0.89 | 1.73 |
| 363.19 | 10.90 | 66.05 | 0.18 | 51.00 | 0.72 | 3.68 | 2.43 | 1.25 | 6.60 |

Note: See "Sedimentation Rates" section, this chapter, for more details. Parameters are % CaCO_3 , % C_{org} , DBD, LSR, Bulk MAR, CaCO_3 MAR, non- CaCO_3 MAR (calculated as 100% - % CaCO_3).

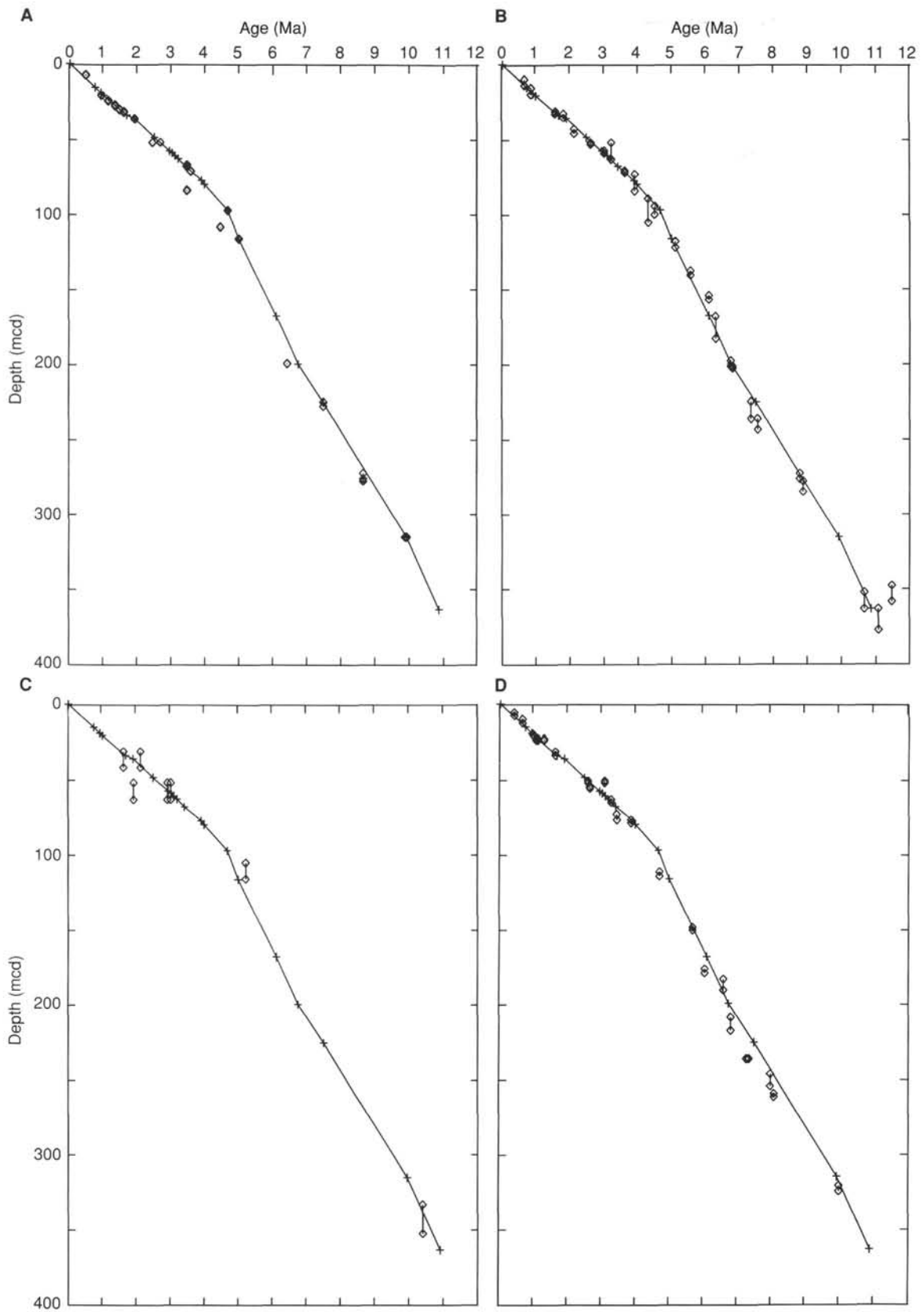


Figure 26. Plot of age vs. depth for Site 851, based on calibration points in Table 10, compared with microfossil datums. **A.** Nannofossils. **B.** Diatoms. **C.** Foraminifers. **D.** Radiolarians. For radiolarians, only datums that have appeared consistent in the earlier Leg 138 Sites 844 through 848 are shown. Age control points from Table 10 are indicated by crosses. For each datum, the depth limits within which it was observed have been indicated; where only a single symbol is visible, the limits were too small to indicate at this plot scale.

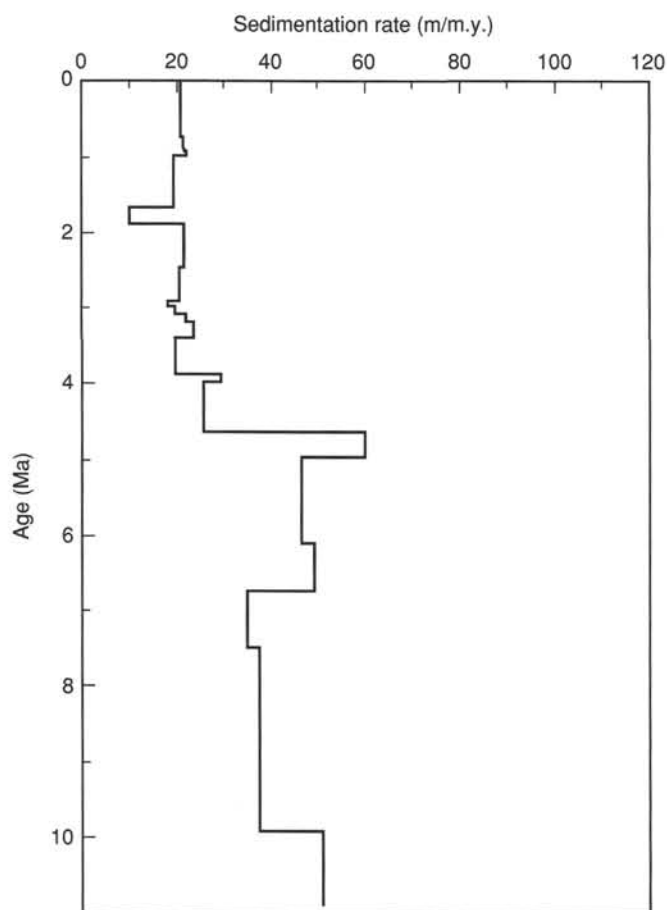


Figure 27. Linear sedimentation rate vs. age, based on data in Table 10.

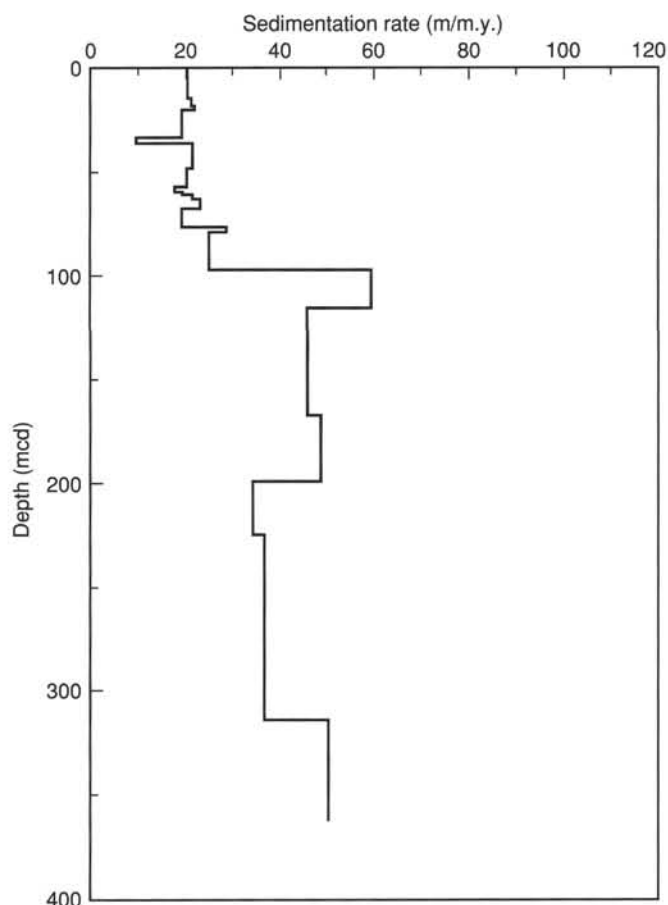


Figure 28. Linear sedimentation rate vs. composite depth, based on data in Table 10.

- Gieskes, J. M., 1974. Chemistry of interstitial waters of marine sediments. *Annu. Rev. Earth Planet. Sci.*, 3:433–394.
- Gieskes, J. M., Elderfield, H., and Palmer, M. R., 1986. Strontium and its isotopic composition in interstitial waters of marine carbonate sediments. *Earth Planet. Sci. Lett.*, 77:229–235.
- Johnson, D. A., and Nigrini, C. A., 1985. Synchronous and time-transgressive Neogene radiolarian datum levels in the equatorial Indian and Pacific Oceans. *Mar. Micropaleontol.*, 9:489–523.
- Kastner, M., 1981. Authigenic silicates in deep-sea sediments: formation and diagenesis. In Emiliani, C. (Ed.) *The Sea (Vol.7): The Oceanic Lithosphere*: New York (Wiley), 915–980.
- Mammerickx, J., 1989. Plate 1C. In *The Eastern Pacific Ocean and Hawaii*. Geol. Soc. Am., Geol. of North Am. Ser., Vol. N.
- Mankinen, E. A., and Dalrymple, G. B., 1979. Revised geomagnetic polarity time scale for the interval 0–5 m.y. BP. *J. Geophys. Res.*, 84:615–626.
- Martini, E., 1971. Standard Tertiary and Quaternary calcareous nannoplankton zonation. *Proc. 2nd Conf. Planktonic Microfossils, Roma 1970*. Rome (Ed. Tecnosci.), 739–785.
- Mayer, L. A., 1991. Extraction of high-resolution carbonate data for paleoclimate reconstruction. *Nature*, 352:148–151.

- Mayer, L. A., Shipley, T. H., Theyer, F., Wilkens, R., and Winterer, E. L., 1985. Seismic modeling and paleoceanography at Deep Sea Drilling Project Site 574. In Mayer, L. A., Theyer, F., et al., *Init. Repts. DSDP*, 85: Washington (U.S. Govt. Printing Office), 947–970.
- McDuff, R. E., 1981. Major cation gradients in DSDP interstitial waters: the role of diffusive exchange between seawater and the upper ocean crust. *Geochim. Cosmochim. Acta*, 45:1705–1713.
- Okada, H., and Bukry, D., 1980. Supplementary modification and introduction of code numbers to the low-latitude coccolith biostratigraphic zonation (Bukry 1973; 1975). *Mar. Micropaleontol.*, 5:321–325.
- Pedersen, T. F., and Shimmiel, G. B., 1991. Interstitial water chemistry, Leg 117: contrasts with the Peru Margin. In Prell, W. L., Niituma, N., et al., *Proc. ODP, Sci. Results*, 117: College Station, TX (Ocean Drilling Program), 499–513.
- van Andel, T. H., Heath, G. R., and Moore, T. C., 1975. Cenozoic tectonics, sedimentation, and paleoceanography of the central equatorial Pacific. *Mem. Geol. Soc. Am.*, 143.

Ms 138A-116

NOTE: For all sites drilled, core description forms (“barrel sheets”) and core photographs have been reproduced on coated paper and can be found in Section 8, beginning on page 1099. Forms containing smear-slide data can be found in Section 9, beginning on page 1435.

Formation microscanner images for this site are presented on microfiche in the back of Part 2.

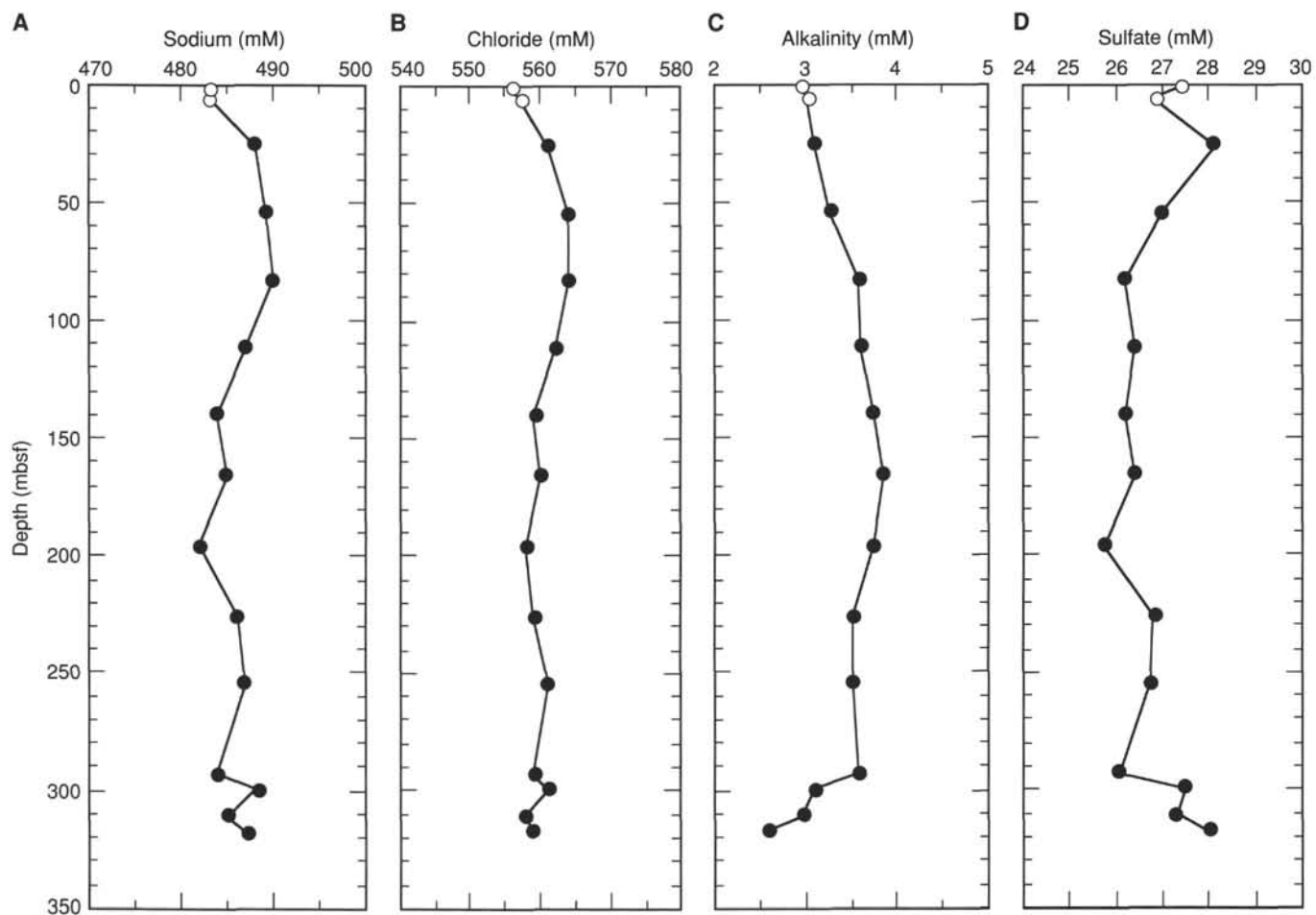


Figure 29. Interstitial-water geochemical data with sub-bottom depths for Holes 851A (open circles) and 851B (solid circles). **A.** Sodium. **B.** Chloride. **C.** Alkalinity. **D.** Sulfate.

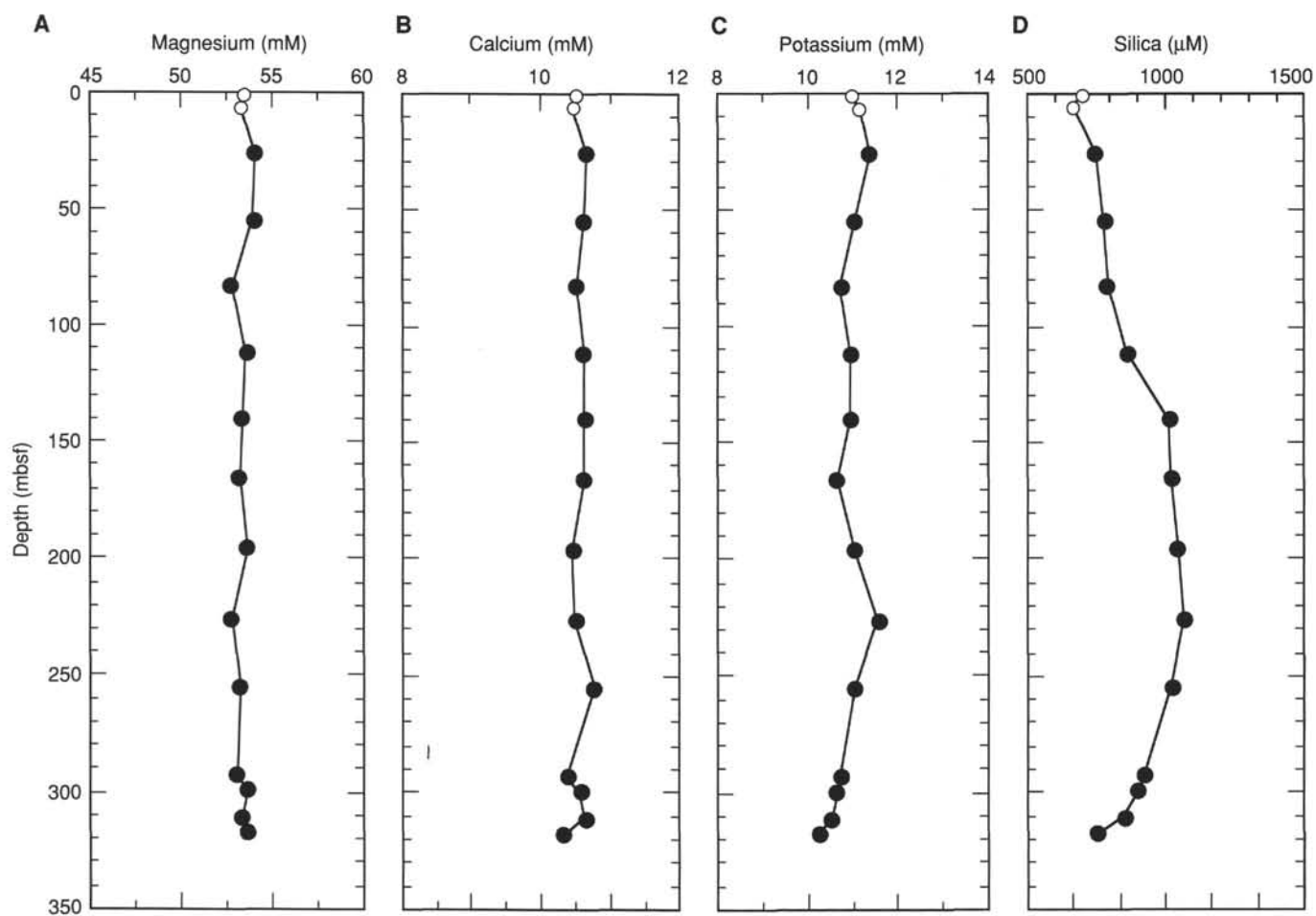


Figure 30. Interstitial-water geochemical data with sub-bottom depths for Holes 851A (open circles) and 851B (solid circles). **A.** Magnesium. **B.** Calcium. **C.** Potassium. **D.** Silica.

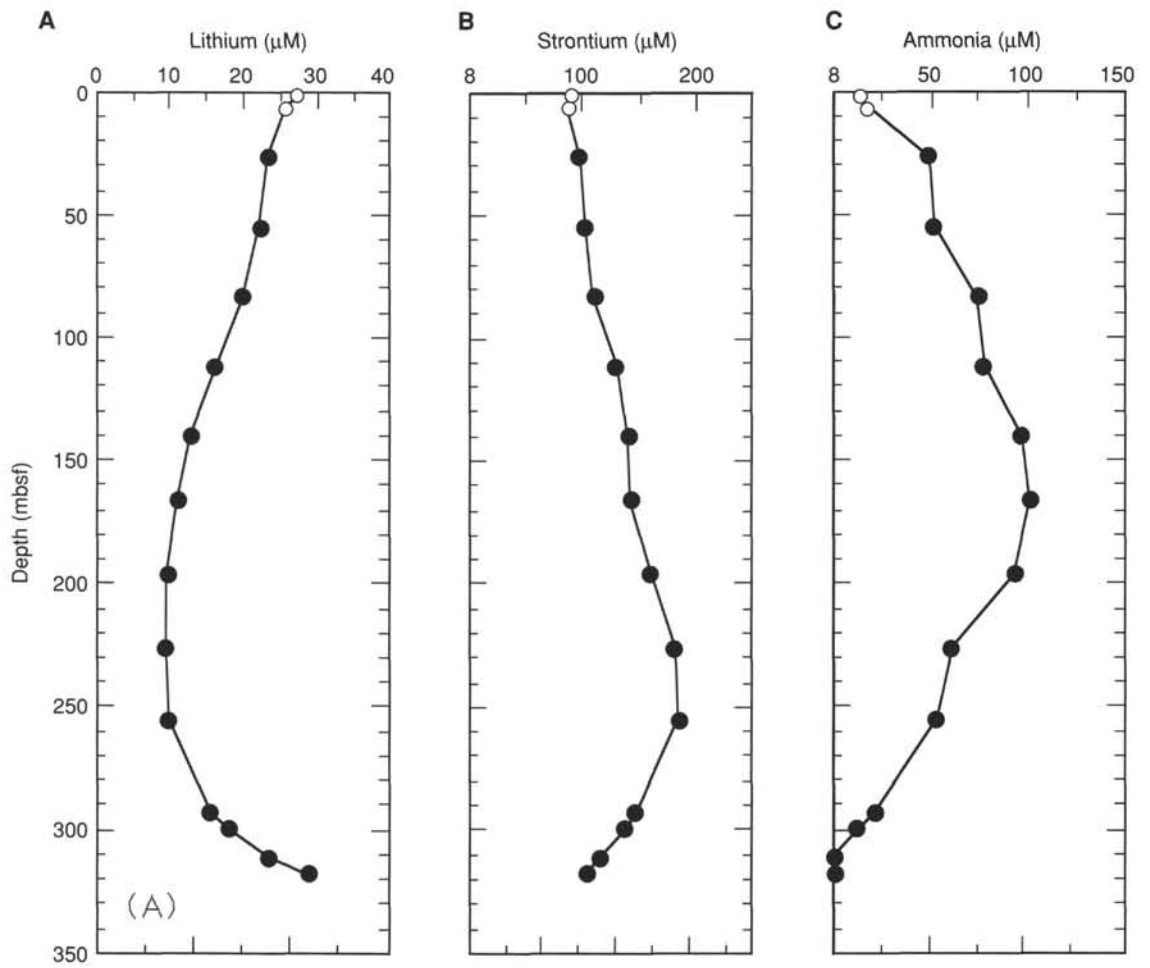


Figure 31. Interstitial water geochemical data with sub-bottom depths for Holes 851A (open circles) and 851B (solid circles). **A.** Lithium. **B.** Strontium. **C.** Ammonia.

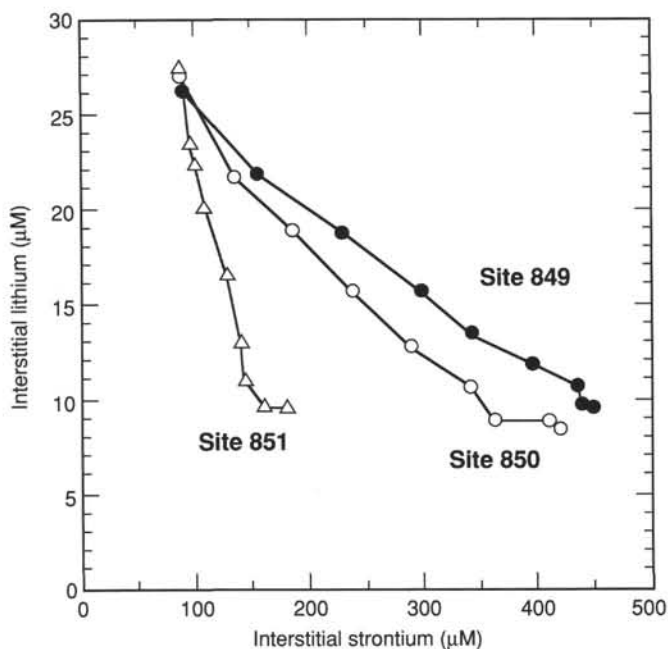


Figure 32. Concentrations of interstitial lithium plotted vs. concentrations of interstitial strontium for Sites 849, 850, and 851. Only data above 250 mbsf have been plotted to avoid the influence of chert layers and basement.

Table 15. Concentrations of methane in samples from Hole 851B.

| Core, section, interval (cm) | Depth (mbsf) | Methane ($\mu\text{L/L}$) |
|------------------------------|--------------|-----------------------------|
| 138-851B-1H-3, 145-150 | 4.45 | 17.5 |
| 2H-4, 145-150 | 13.45 | 1.3 |
| 3H-6, 140-145 | 25.90 | 3.7 |
| 4H-6, 145-150 | 35.45 | 13.8 |
| 5H-4, 145-150 | 41.95 | 8.5 |
| 6H-6, 140-145 | 54.40 | 6.8 |
| 7H-6, 145-150 | 63.95 | 5.0 |
| 8H-6, 145-150 | 73.45 | 10.8 |
| 9H-6, 140-145 | 82.90 | 3.7 |
| 10H-6, 135-140 | 92.35 | 11.8 |
| 11H-6, 145-150 | 101.95 | 9.6 |
| 12H-6, 140-145 | 111.40 | 5.1 |
| 13H-6, 145-150 | 120.95 | 11.4 |
| 14H-6, 145-150 | 130.45 | 6.1 |
| 15H-6, 140-145 | 139.90 | 9.7 |
| 16X-6, 145-150 | 149.45 | 18.5 |
| 17X-6, 145-150 | 159.05 | 6.4 |
| 18X-4, 140-145 | 165.70 | 10.3 |
| 19X-6, 145-150 | 178.35 | 8.5 |
| 20X-6, 145-150 | 188.05 | 8.1 |
| 21X-5, 137-142 | 195.67 | 10.6 |
| 22X-6, 145-150 | 206.45 | 10.1 |
| 23X-6, 145-150 | 216.05 | 8.0 |
| 24X-6, 137-142 | 225.67 | 18.3 |
| 25X-6, 145-150 | 235.35 | 11.6 |
| 26X-6, 145-150 | 245.05 | 9.8 |
| 27X-6, 137-142 | 254.67 | 14.0 |
| 28X-6, 145-150 | 264.45 | 14.7 |
| 29X-5, 0-5 | 271.10 | 12.5 |
| 31X-6, 139-144 | 292.89 | 18.5 |
| 32X-4, 137-142 | 299.47 | 3.4 |
| 33X-5, 137-142 | 310.57 | 0.0 |
| 34X-3, 137-142 | 317.27 | |

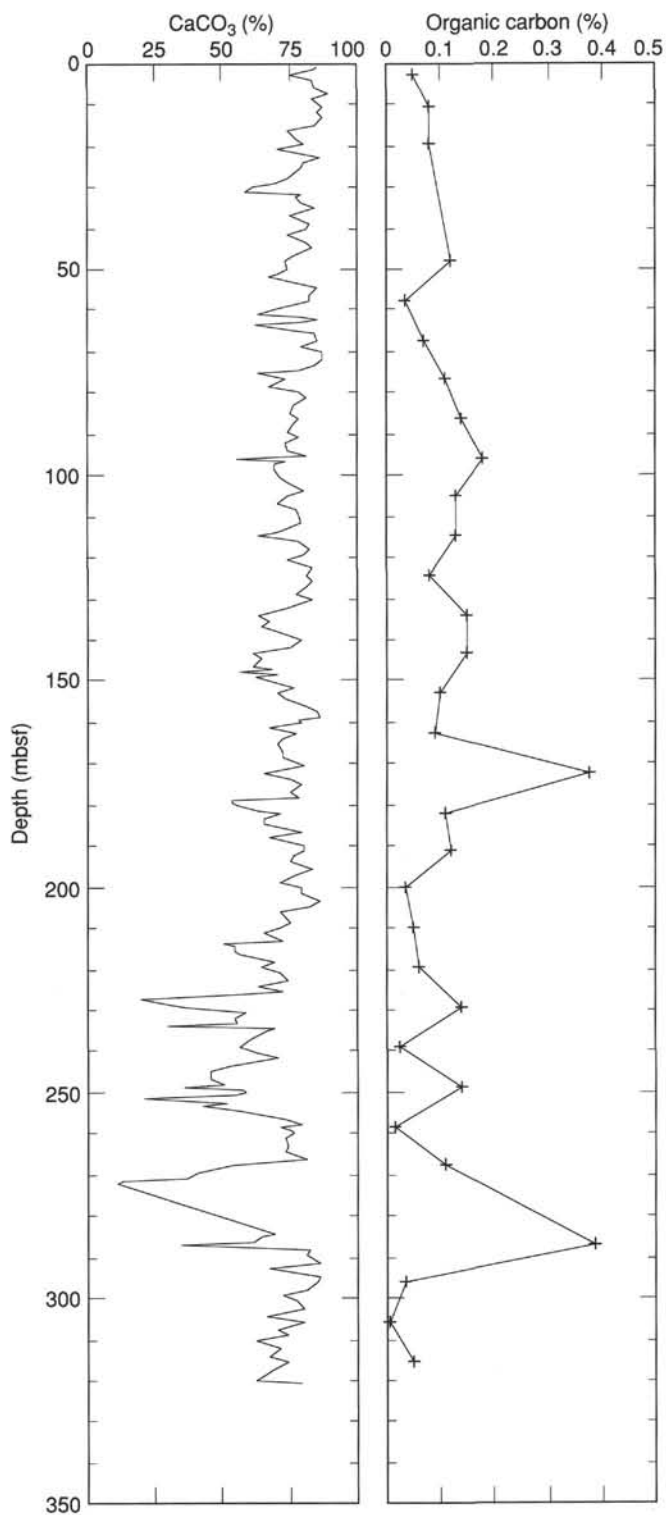


Figure 33. Downhole records of percentages of CaCO_3 and C_{org} vs. ODP depth for Site 851.

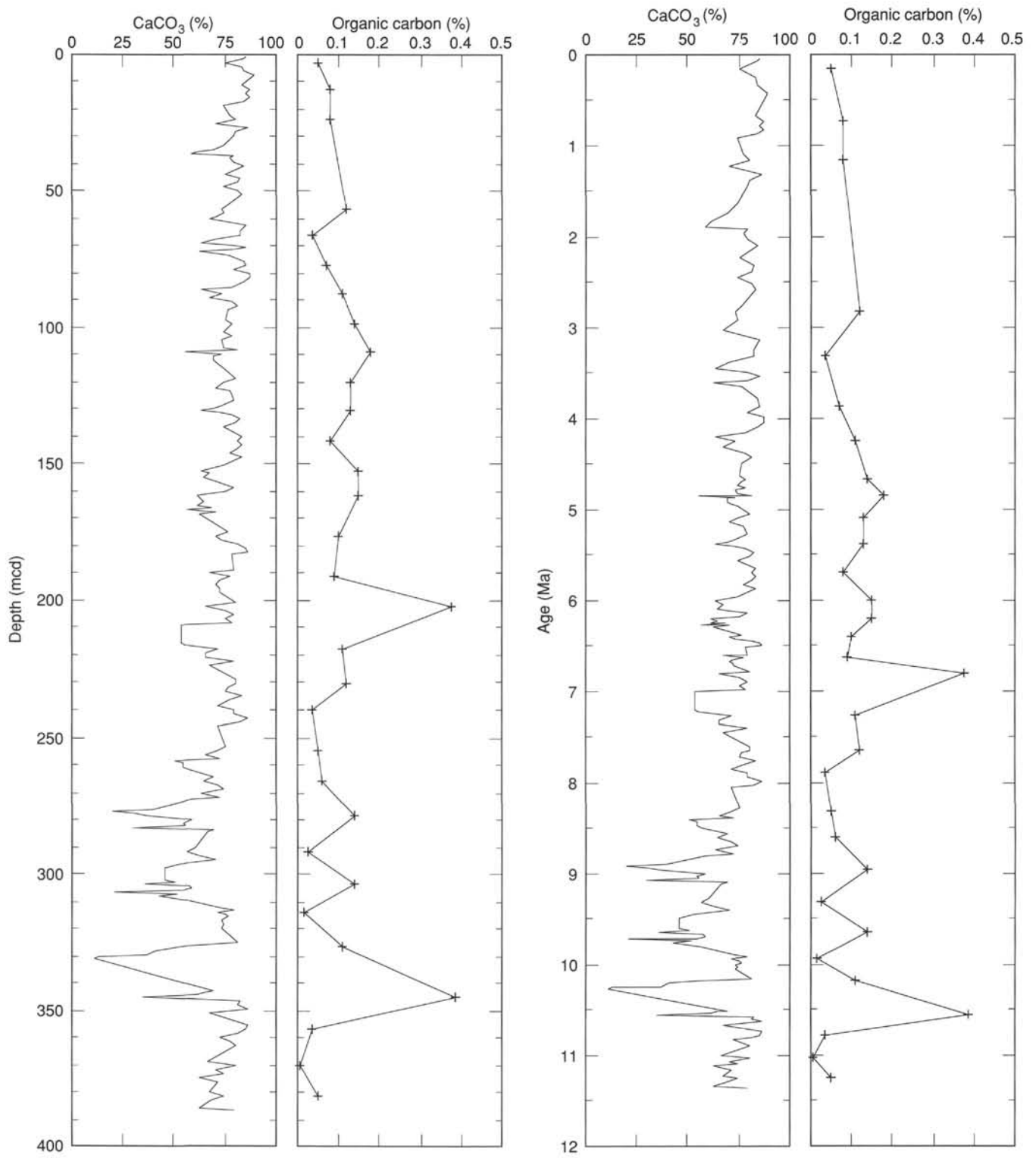


Figure 34. Plots of percentages CaCO_3 and C_{org} vs. composite depth and age for Site 851.

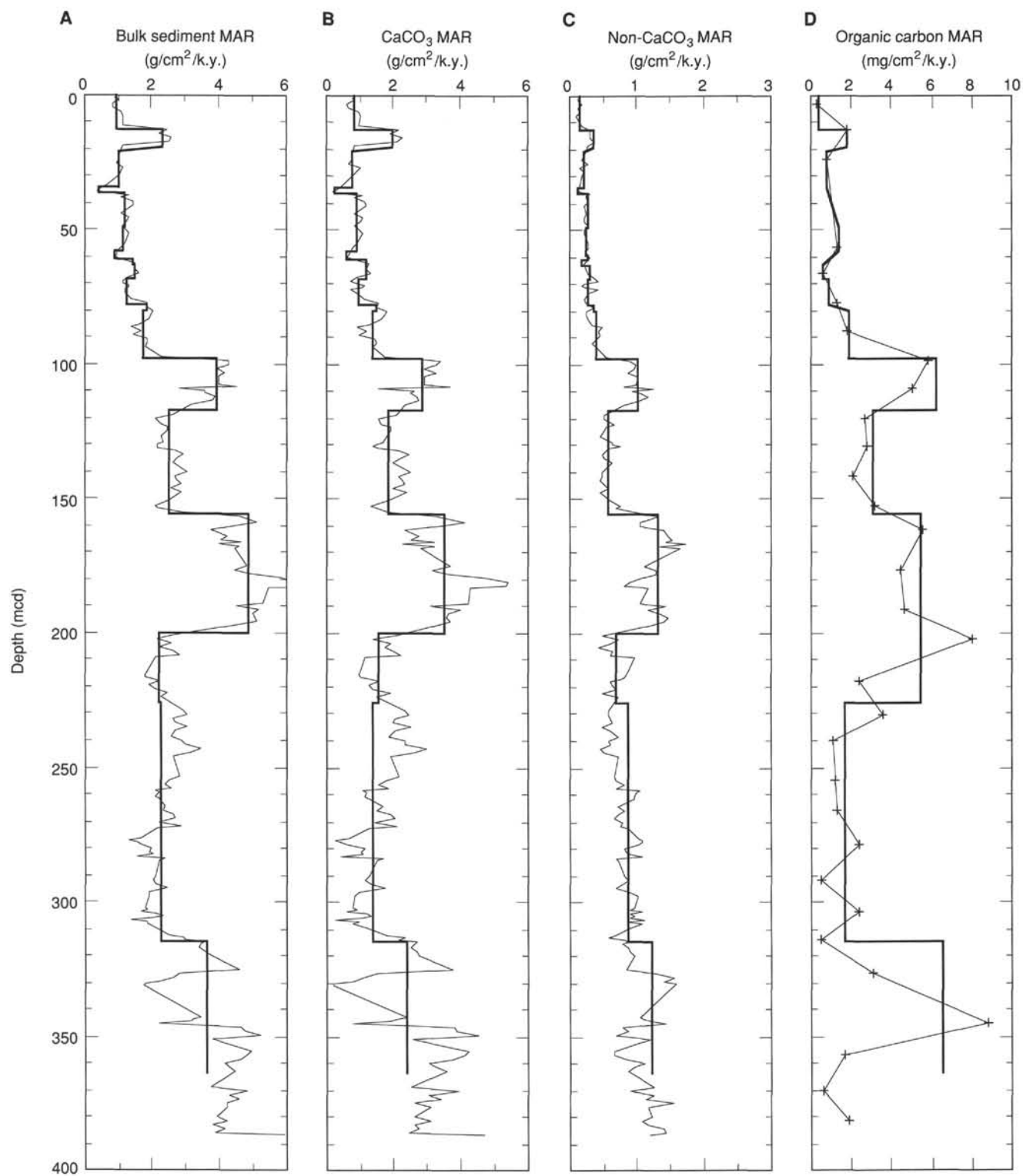


Figure 35. Mass accumulation rates of bulk sediment (A), CaCO₃ (B), non-CaCO₃ (C), and C_{org} (D) vs. composite depth at Site 851. Note different units for C_{org}. Thick line is the mean value between each stratigraphic datum plane; thin line shows discrete accumulation rates calculated for each sample.

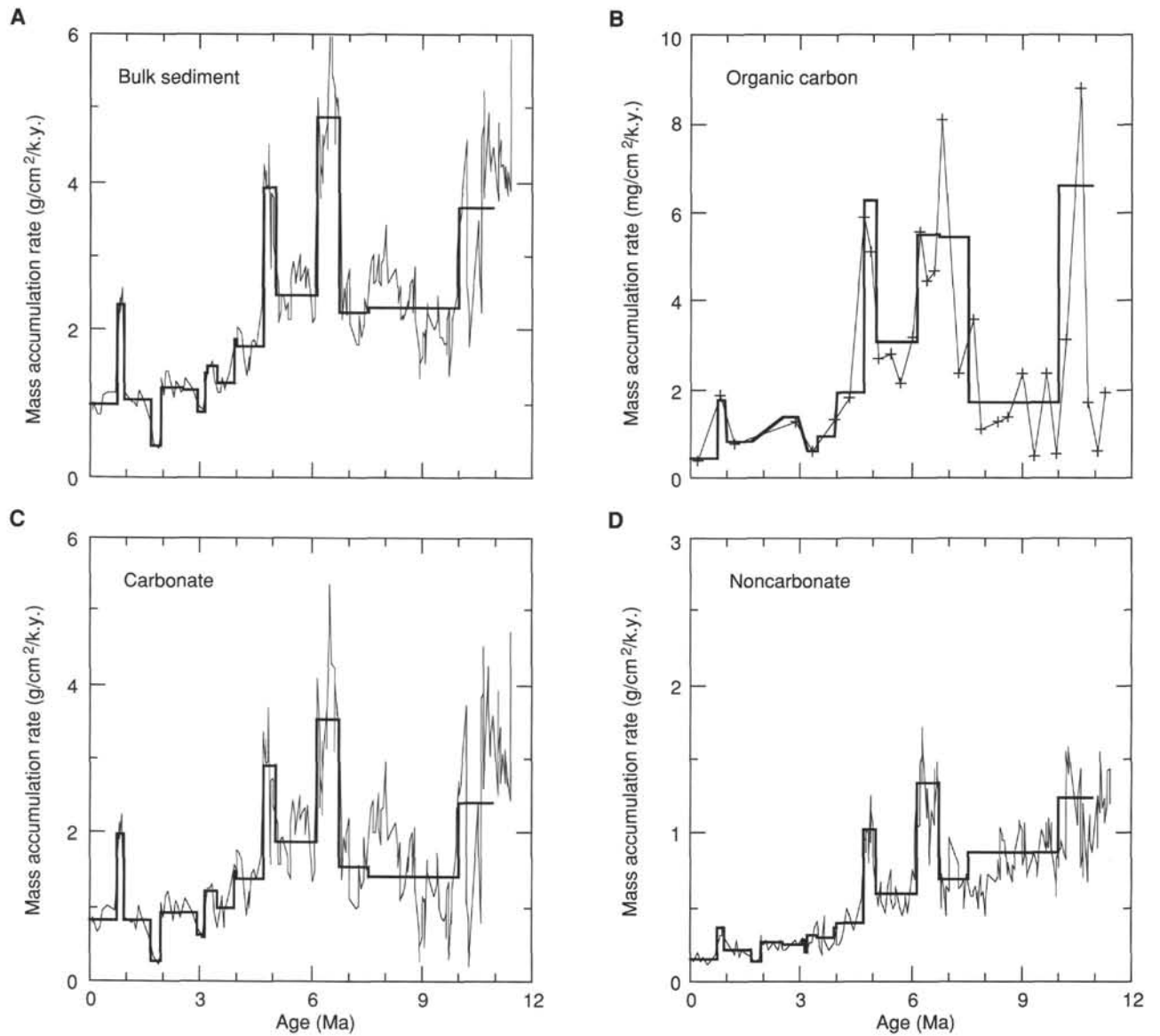


Figure 36. Mass accumulation rates of bulk sediment (A), C_{org} (B), CaCO₃ (C), and non-CaCO₃ (D) vs. age in sediments from Site 851. Thick line is the mean value between each stratigraphic datum plane; thin line shows discrete accumulation rates calculated for each sample.

Table 20. Depth intervals over which logging data were considered reliable.

| Log type | Depth (mbsf) |
|------------------------|--------------|
| Resistivity | 66.8–320.4 |
| Bulk density | 73.4–311.1 |
| Sonic velocity | 61.6–302.1 |
| Sonic waveforms | 61.6–302.1 |
| Gamma-ray/U-Th-K | 0–320.1 |
| Aluminum | 0–316.7 |
| Geochemistry | 0–318.4 |
| Caliper | 69.7–320.1 |
| Formation microscanner | 69.7–320.1 |

Note: Depth in mbsf was calculated assuming feet below rig floor (fbrf) = 3772; geophysical logs have been shifted +0.8 m; geochemical logs have been shifted -0.88 m; FMS logs were not shifted.

Table 21. Means and standard deviations of log properties in three log subunits.

| Tool string | Subunit IA | Subunit IB | Subunit IC |
|--|---------------|---------------|---------------|
| Geophysical | | | |
| Intermediate resistivity (ohm-m): | 0.68 ± 0.038 | 0.64 ± 0.054 | 0.75 ± 0.053 |
| Shallow resistivity (ohm-m): | 0.61 ± 0.042 | 0.59 ± 0.048 | 0.67 ± 0.051 |
| Gamma-ray activity (API units): | 5.68 ± 1.15 | 4.54 ± 0.79 | 4.42 ± 0.415 |
| Wet-bulk density (g/cm ³): | 1.51 ± 0.044 | 1.46 ± 0.053 | 1.57 ± 0.054 |
| Velocity (km/s): | 1.58 ± 0.048 | 1.61 ± 0.045 | 1.7 ± 0.053 |
| Calculated porosity (%): | 76.8 ± 9.2 | 64 ± 7.2 | 66.7 ± 4.6 |
| Geochemical | | | |
| Calcium-yield: | 0.095 ± 0.076 | 0.08 ± 0.019 | 0.115 ± 0.019 |
| Silicon-yield: | 0.016 ± 0.013 | 0.023 ± 0.015 | 0.018 ± 0.013 |
| Hydrogen-yield: | 0.274 ± 0.008 | 0.278 ± 0.01 | 0.271 ± 0.006 |
| PHIG (Porosity estimate): | 0.48 ± 0.076 | 0.50 ± 0.083 | 0.41 ± 0.062 |

Table 22. Summary of traveltimes, depths, and ages for Site 851 reflectors.

| Reflector | Traveltime (s) | Synthetic depth (m) | Depth (mbsf) | Depth (mcd) | Age (Ma) |
|-----------|----------------|---------------------|--------------|-------------|----------|
| R1 | 0.023 | 17.40 | 17.90 | 22.05 | 1.06 |
| | 0.027 | 20.50 | 20.40 | 24.55 | 1.19 |
| R2 | 0.055 | 41.60 | 44.50 | 50.80 | 2.57 |
| | 0.060 | 45.40 | 46.30 | 54.20 | 2.74 |
| R3 | 0.067 | 50.70 | 52.20 | 60.10 | 3.04 |
| | 0.073 | 55.30 | 55.00 | 62.90 | 3.17 |
| R5 | 0.085 | 64.34 | 63.20 | 71.65 | 3.58 |
| | 0.104 | 78.80 | 79.80 | 90.20 | 4.38 |
| R7 | 0.118 | 89.50 | 86.30 | 98.30 | 4.68 |
| | 0.122 | 92.50 | 90.00 | 102.00 | 4.74 |
| R11 | 0.157 | 119.70 | 121.80 | 137.60 | 5.58 |
| | 0.174 | 133.30 | 134.20 | 152.50 | 6.01 |
| R15 | 0.200 | 153.80 | 150.40 | 173.90 | 6.37 |
| | 0.214 | 165.00 | 159.80 | 188.30 | 6.58 |
| R16 | 0.222 | 171.50 | 176.10 | 205.80 | 6.93 |
| | 0.227 | 175.50 | 178.10 | 207.90 | 6.99 |
| R18 | 0.241 | 186.80 | 186.40 | 222.30 | 7.41 |
| | 0.250 | 194.20 | 193.10 | 232.40 | 7.69 |
| R20 | 0.265 | 206.70 | 204.90 | 244.30 | 8.02 |
| | 0.269 | 210.80 | 207.90 | 252.80 | 8.25 |
| R21 | 0.307 | 240.60 | 239.40 | 292.20 | 9.34 |
| | 0.315 | 247.00 | 243.50 | 296.30 | 9.45 |
| R23 | 0.335 | 263.10 | 263.80 | 319.70 | 10.05 |
| | 0.338 | 265.60 | 268.30 | 326.70 | 10.19 |
| R24 | 0.350 | 275.10 | 275.50 | 333.90 | 10.32 |
| | 0.357 | 280.70 | 278.20 | 336.60 | 10.38 |
| R25 | 0.362 | 284.90 | 284.30 | 342.70 | 10.50 |
| | 0.365 | 290.00 | 289.10 | 347.50 | 10.59 |

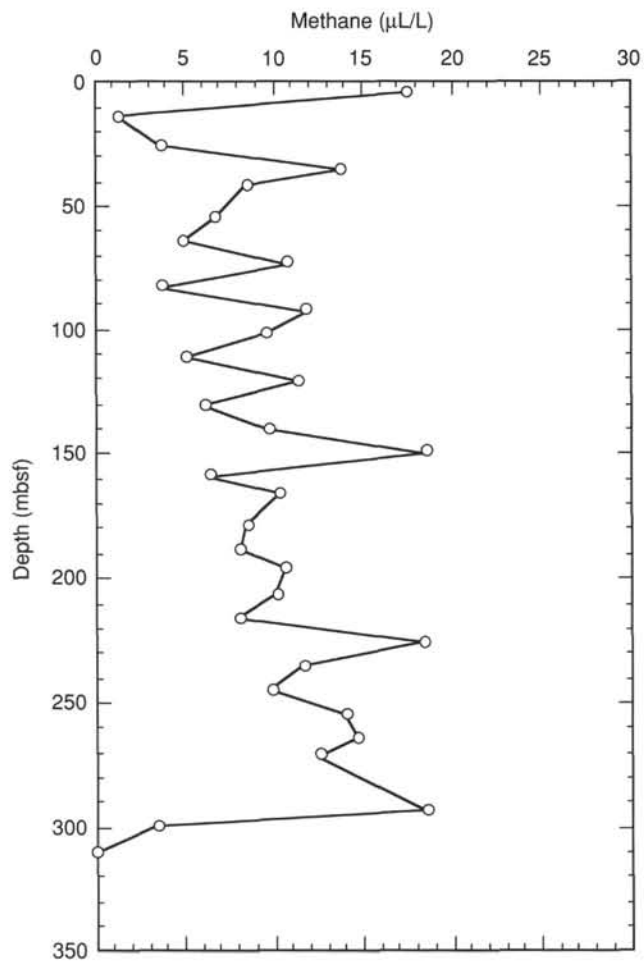


Figure 37. Concentrations of sorbed methane vs. depth in Hole 851B.

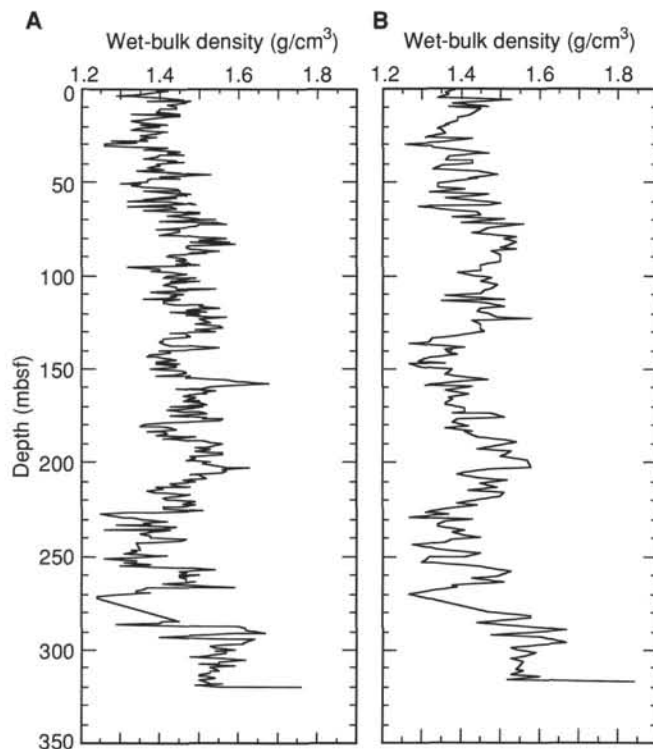


Figure 38. Wet-bulk density vs. depth, Holes 851B (A) and 851E (B).

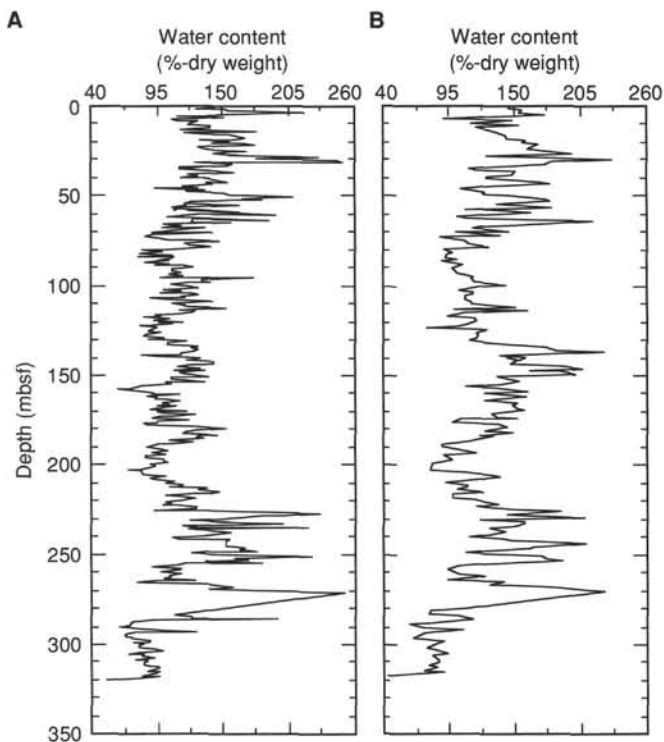


Figure 39. Water content (%dry weight) vs. depth, Holes 851B (A) and 851E (B).

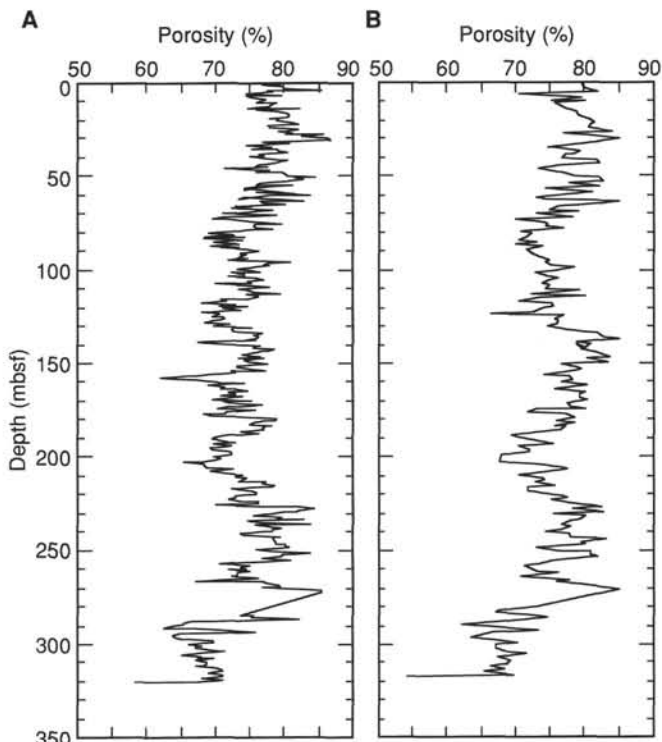


Figure 40. Porosity vs. depth, Holes 851B (A) and 851E (B).

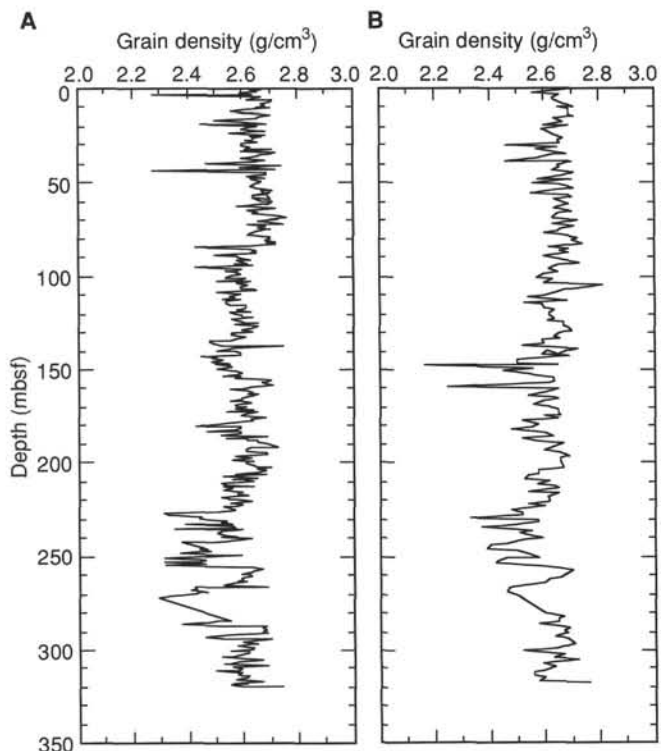


Figure 41. Grain density vs. depth, Holes 851B (A) and 851E (B).

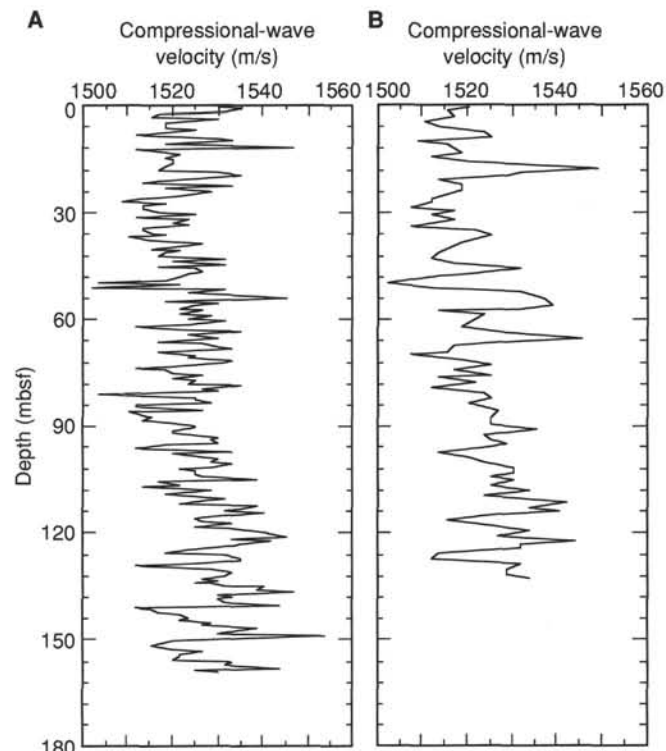


Figure 42. Compressional-wave velocity vs. depth, Holes 851B (A) and 851E (B).

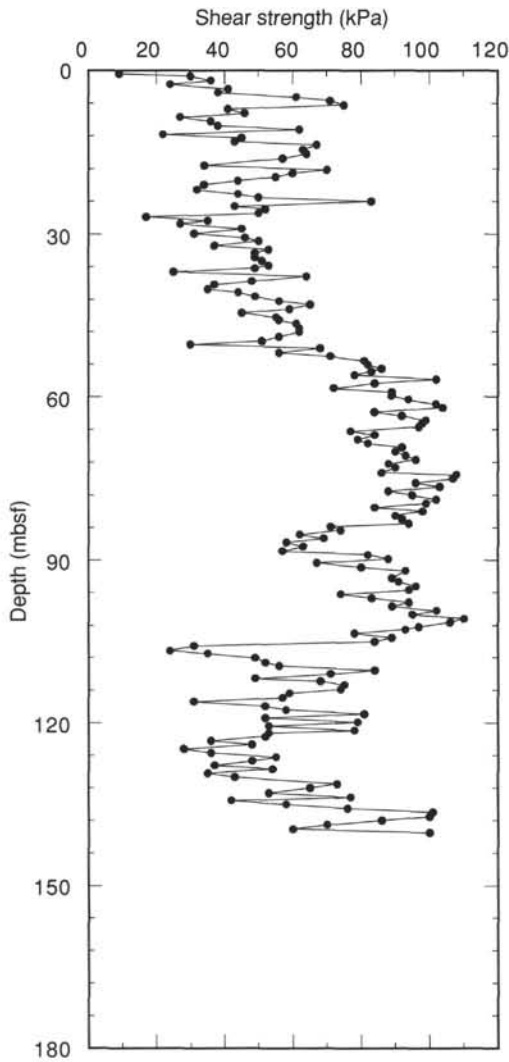


Figure 43. Undrained shear strength vs. depth, Hole 851B.

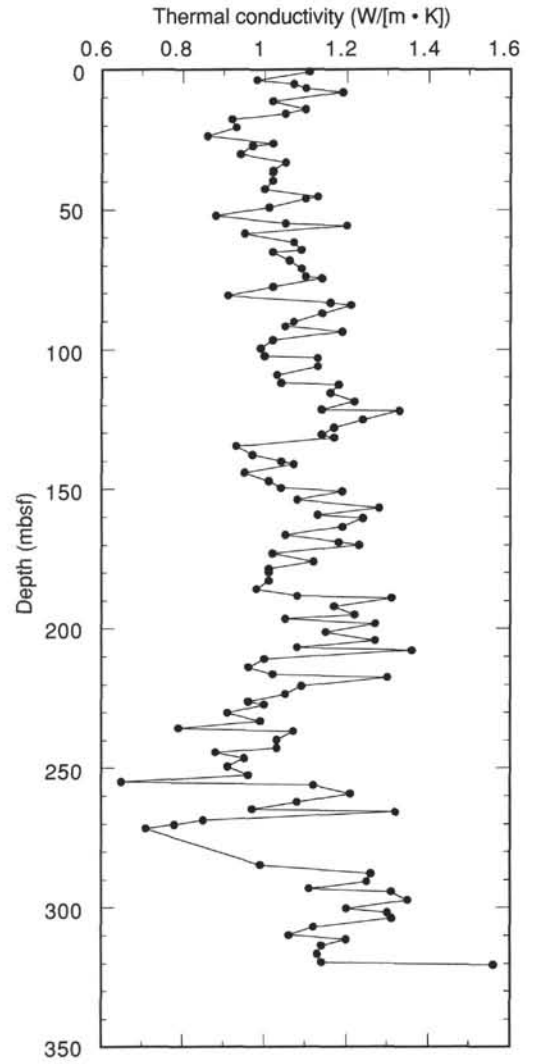


Figure 44. Thermal conductivity vs. depth, Hole 851B.

Table 23. Backtracked path for Site 851.

| Age (Ma) | Latitude (-°S; +°N) | Longitude (°W) |
|----------|---------------------|----------------|
| 1 | 2.55 | 109.85 |
| 2 | 2.30 | 109.09 |
| 3 | 2.05 | 108.33 |
| 4 | 1.81 | 107.58 |
| 5 | 1.56 | 106.82 |
| 6 | 1.32 | 106.06 |
| 7 | 1.09 | 105.30 |
| 8 | 0.86 | 104.54 |
| 9 | 0.63 | 103.78 |
| 10 | 0.40 | 103.02 |
| 11 | 0.17 | 102.26 |
| 12 | -0.05 | 101.49 |
| 13 | -0.26 | 100.73 |
| 14 | -0.48 | 99.96 |
| 15 | -0.69 | 99.20 |

Determined using pole of rotation: 0–12 Ma; 67.0° N, 59.0° W;
angular velocity: 0.84°/m.y.

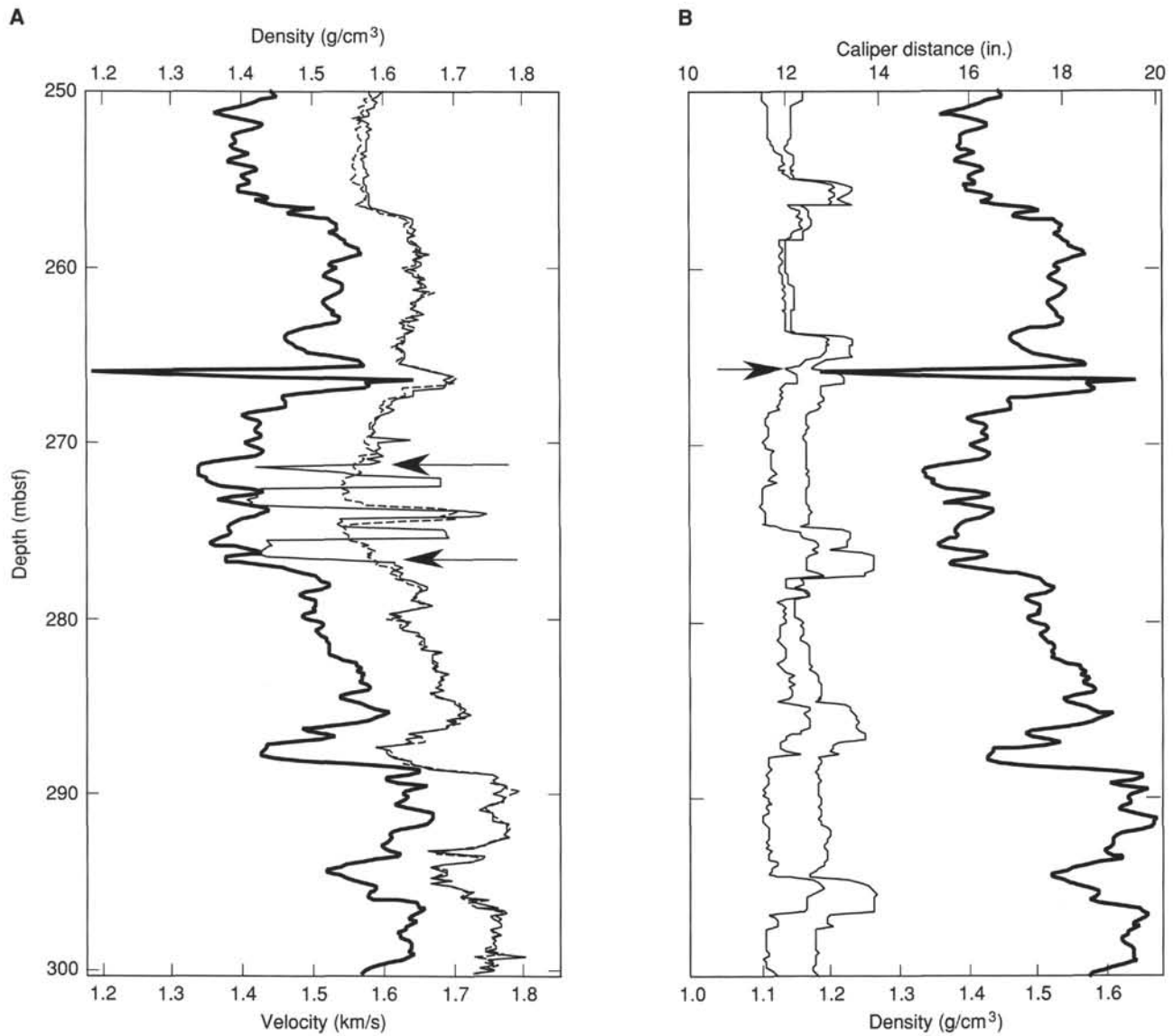


Figure 45. **A.** Density (thick solid line), near velocity (dashed line), and far velocity (thin line) values vs. depth. Limits of anomalous velocity data are marked with arrows. **B.** Caliper distances (thin solid lines) and density (thick solid line) vs. depth; position of ledge observed in Hole 851B is marked with an arrow.

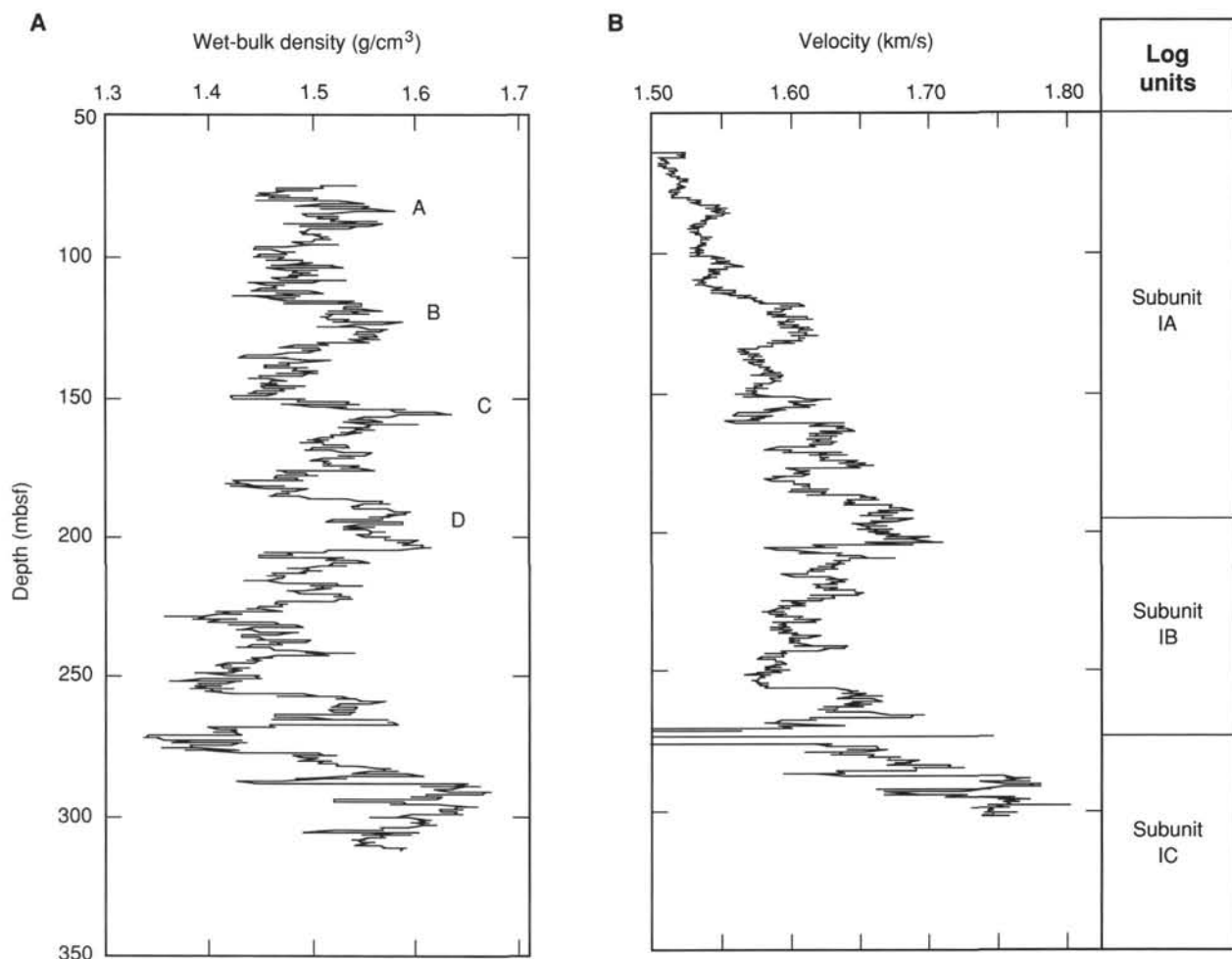


Figure 46. Plots of logging bulk density (A) and velocity (B) vs. depth in Hole 851B. Four maxima in density discussed in the text are identified in (A). Log subunits are marked on right-hand side of figure.

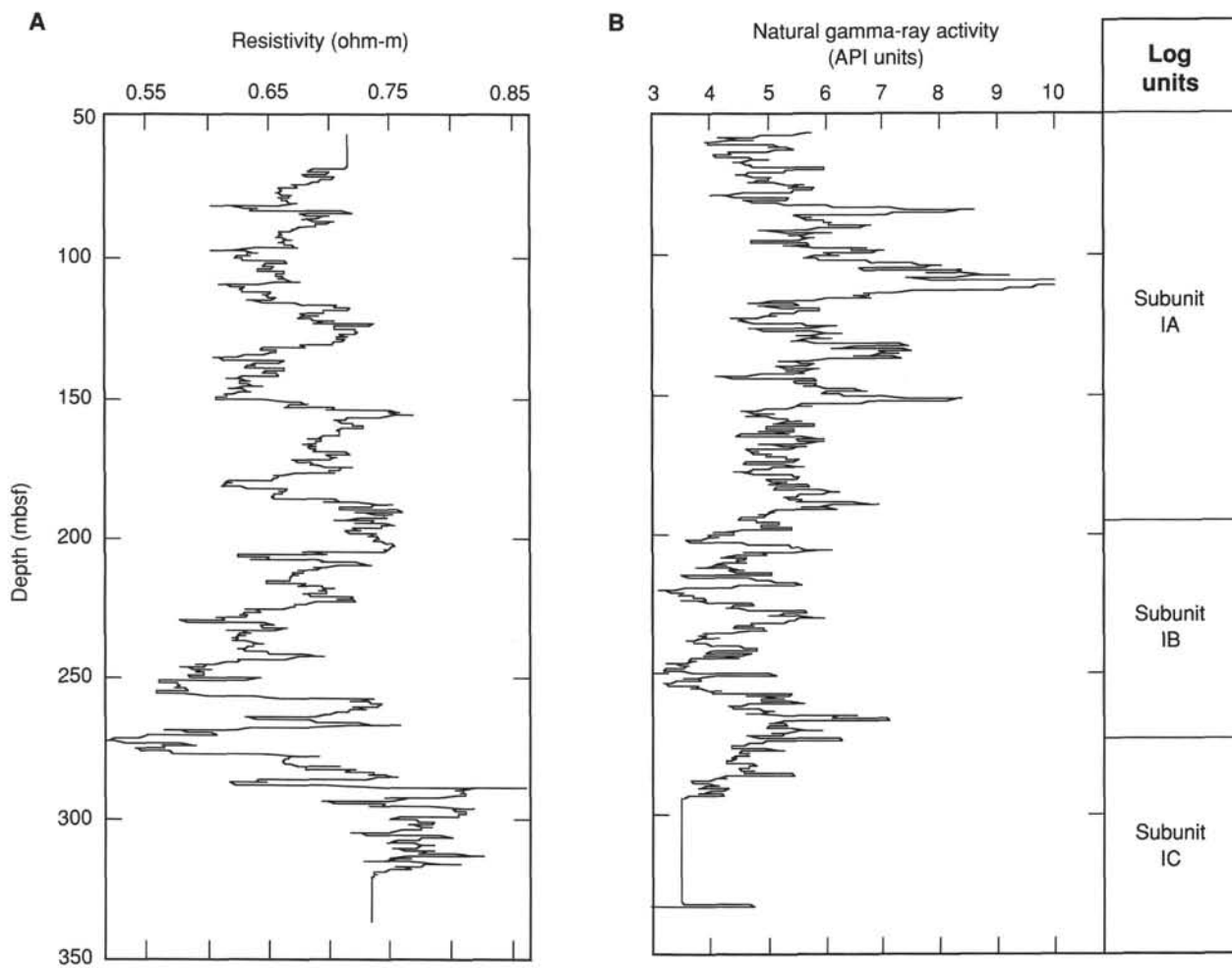


Figure 47. Intermediate resistivity (A) and natural gamma-ray activity (B) vs. depth. Log subunits are marked on right in figure.

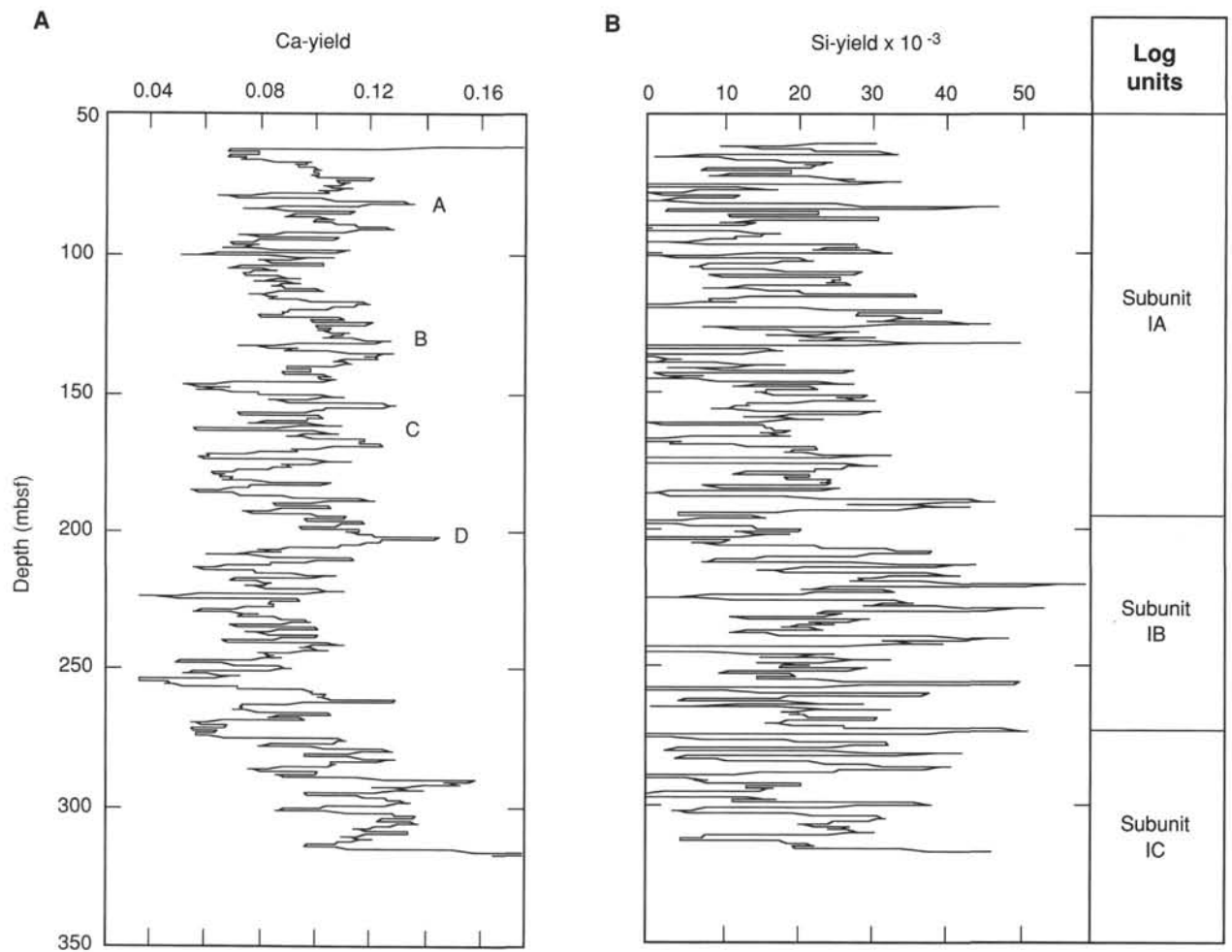


Figure 48. Ca-yield values (A) and Si-yield (B) values vs. depth. Four maxima in Ca-yield that correspond to peaks in density are identified in (A). Log subunits are marked on right in figure.

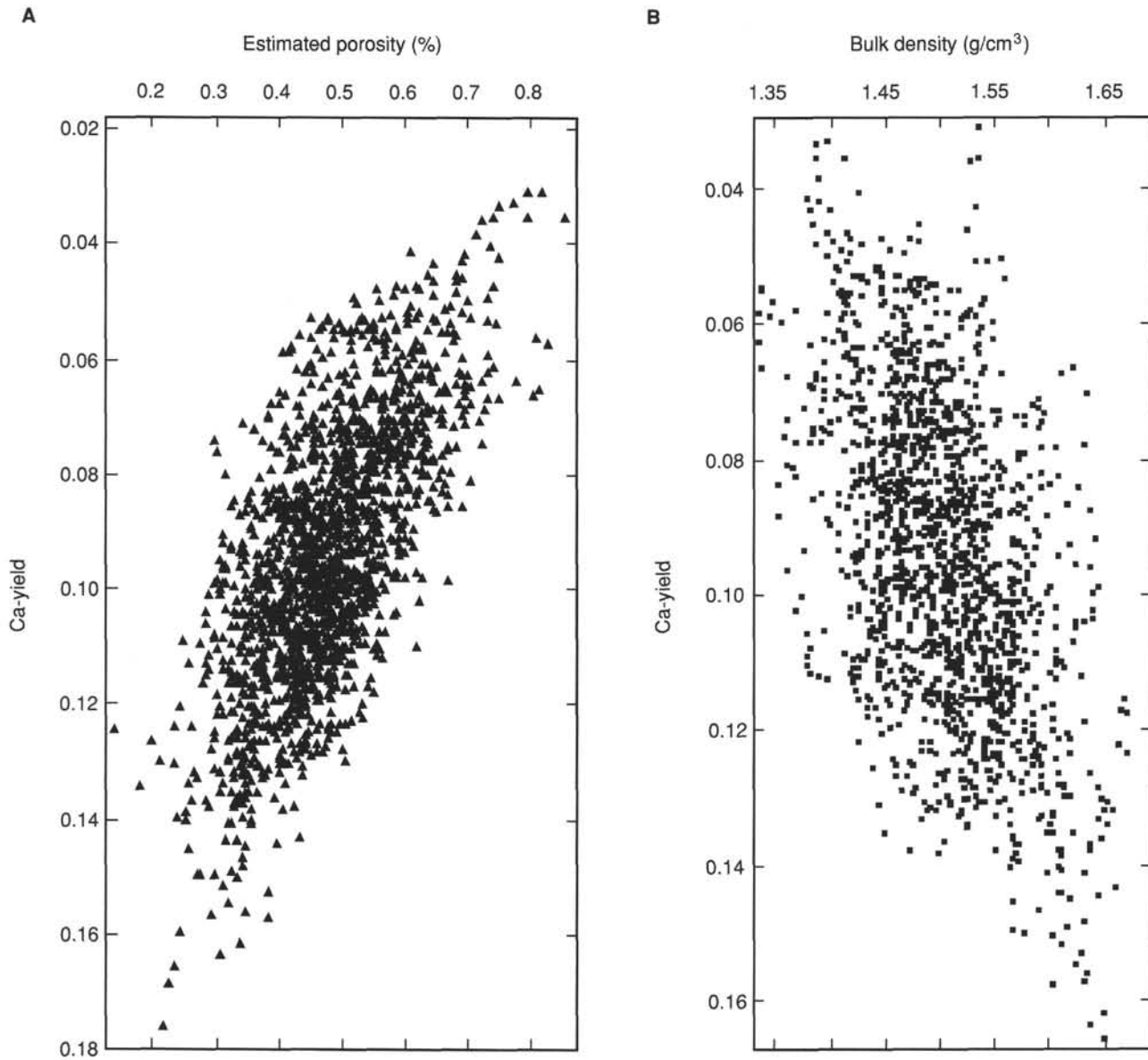


Figure 49. Porosity estimated from neutron geochemistry tool (A) and wet-bulk density (B) vs. Ca-yield. Equations of linear regression lines through the data are $\rho_b = 1.38 + 1.32 \text{ CCA}$; $R^2 = 0.50$ and $\text{PHIG} = 0.77 - 3.08 \text{ CCA}$; $r^2 = 0.68$. (ρ_b = bulk density; PHIG = estimated porosity; CCA = Ca-yield).

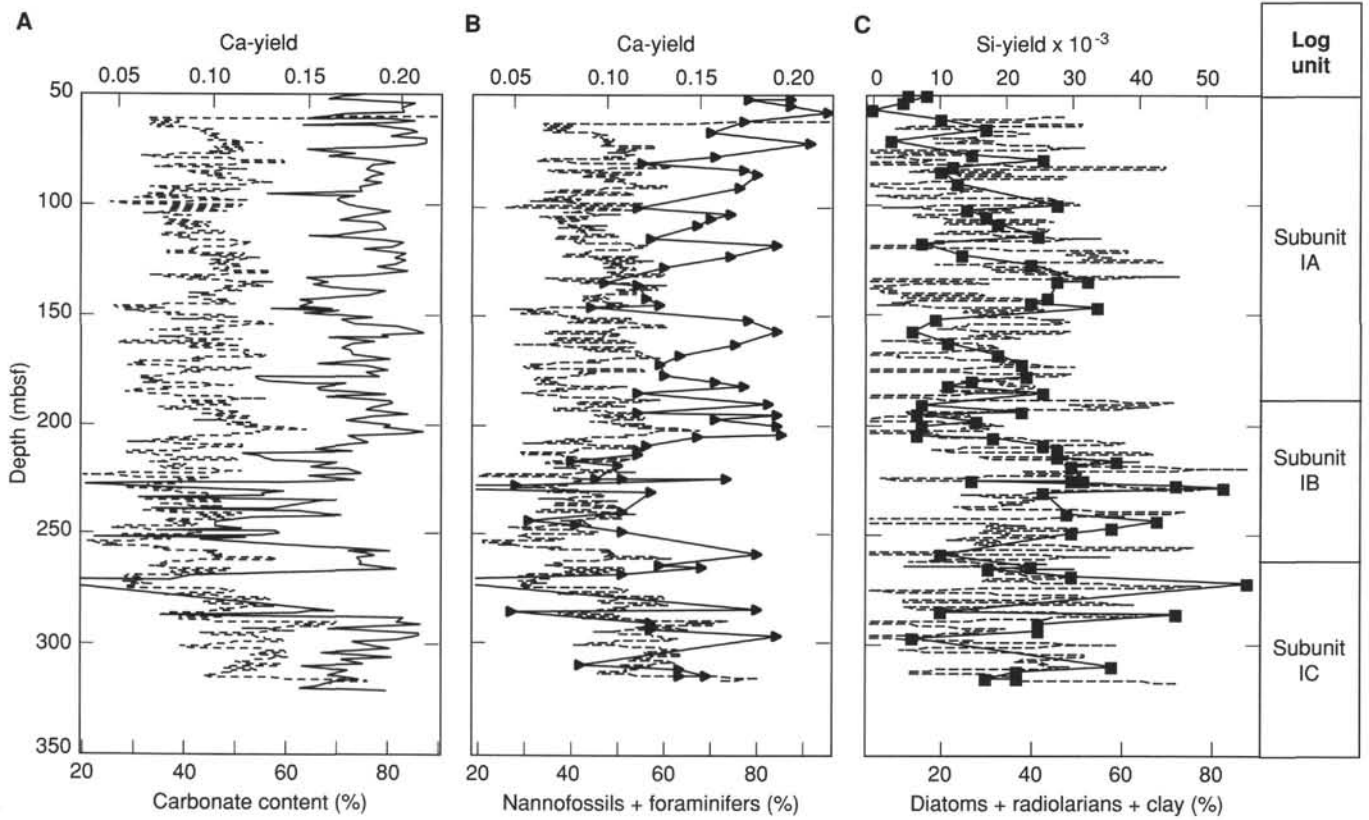


Figure 50. A. Ca-yield (dashed line) and laboratory-determined carbonate contents (solid line) vs. depth. B. Ca-yield (dashed line) and sum of calcareous microfossils (solid line and triangles; estimated from smear slides; Lithostratigraphy section, this chapter) vs. depth. C. Si-yield (dashed line) and sum of clay and siliceous microfossils vs. depth (solid line and squares; estimated from smear slides; see "Lithostratigraphy" section, this chapter). Major features in the trends of carbonate and silica were observed in all the different estimates. Log subunits are marked on right of figure.

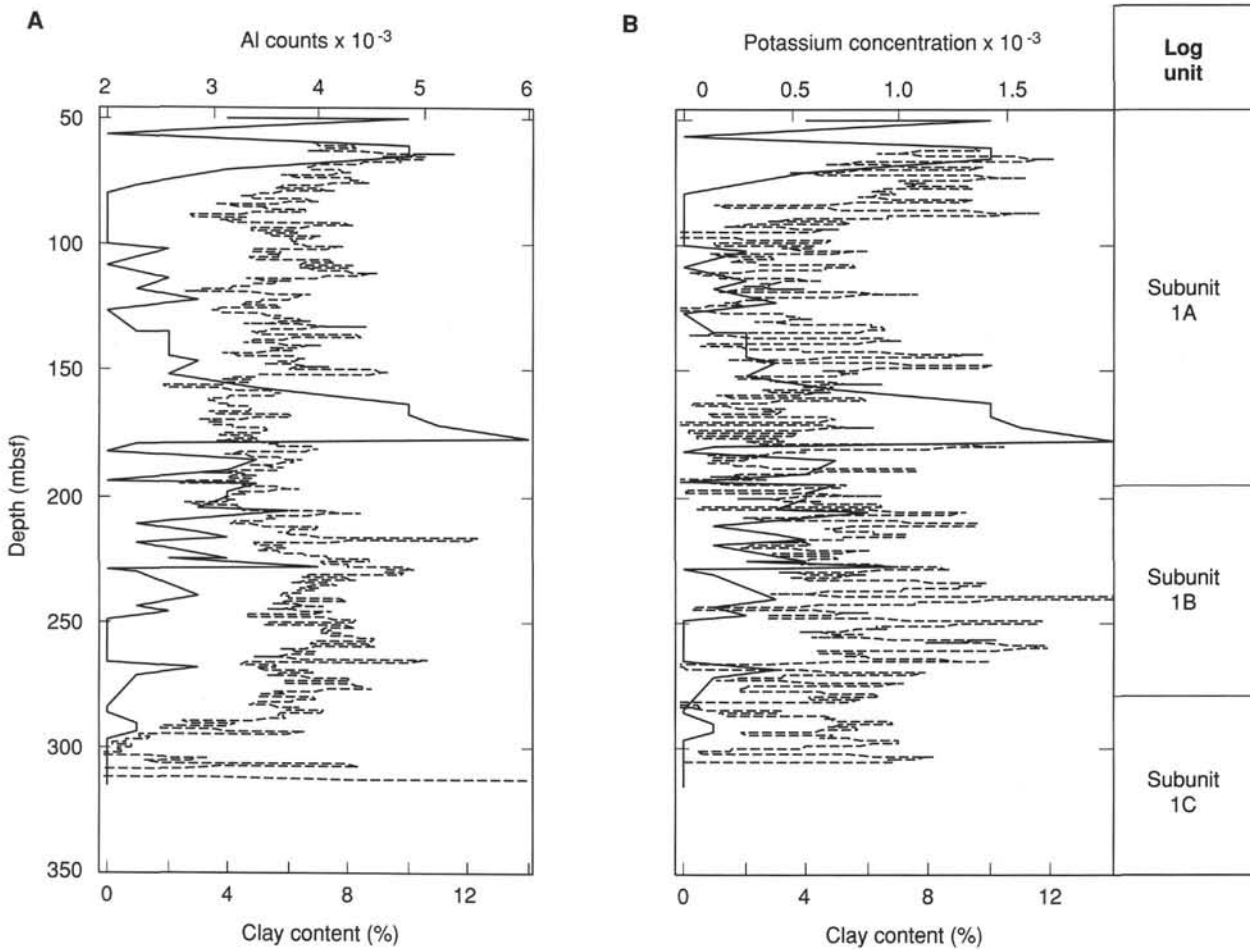


Figure 51. Aluminum counts (A, dashed line), potassium concentrations (B, dashed line), and clay contents (solid lines, estimated from smear slides; see “Lithostratigraphy” section, this chapter) vs. depth. Poor correlations were observed between clay content and these chemical proxies. Log subunits are marked on right in figure.

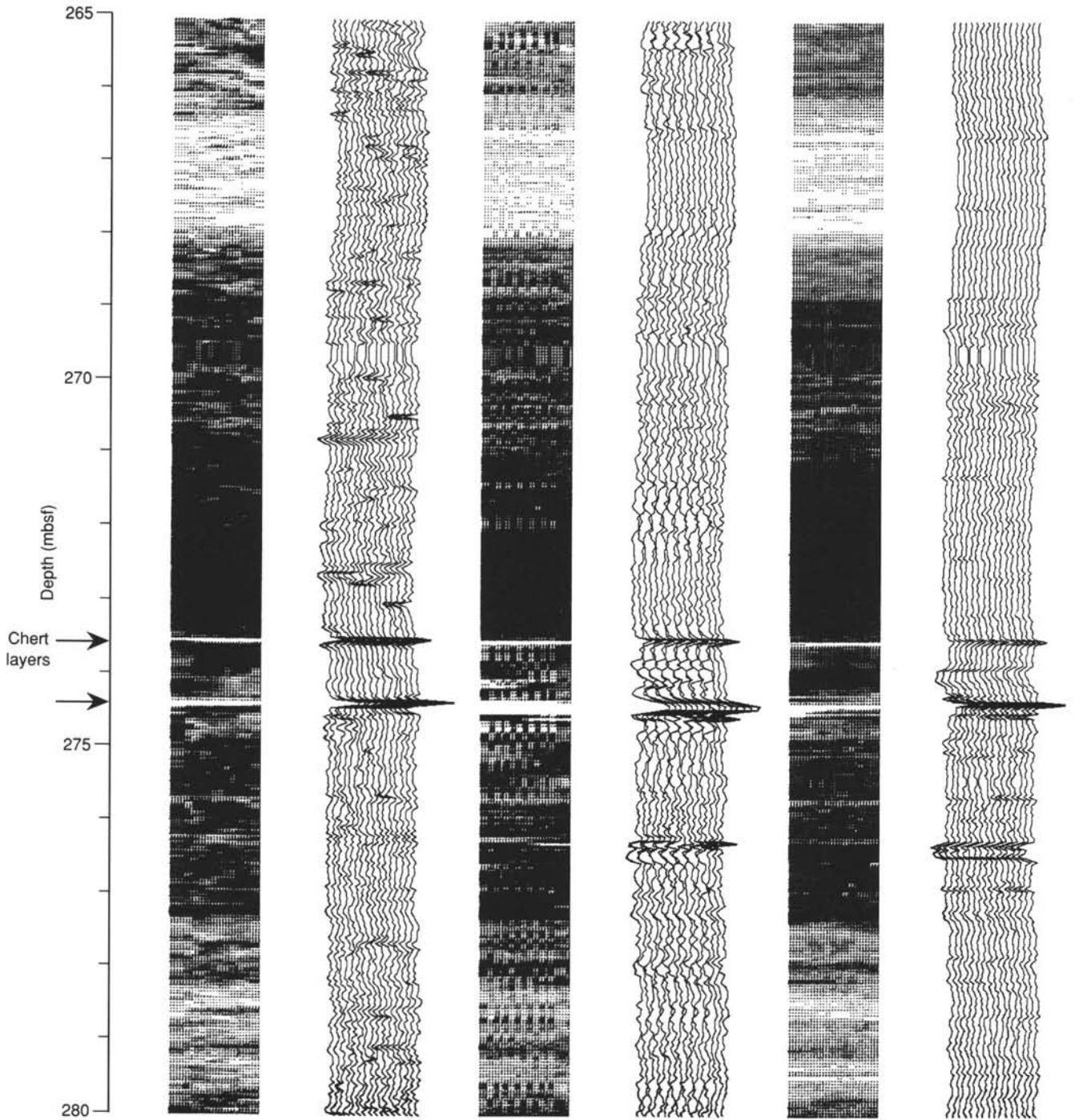


Figure 52. FMS image and “wiggle plots” (raw conductivity data from each button on the two pads shown) of the interval from 265 to 280 mbsf. Locations of two chert layers discussed in text are marked.

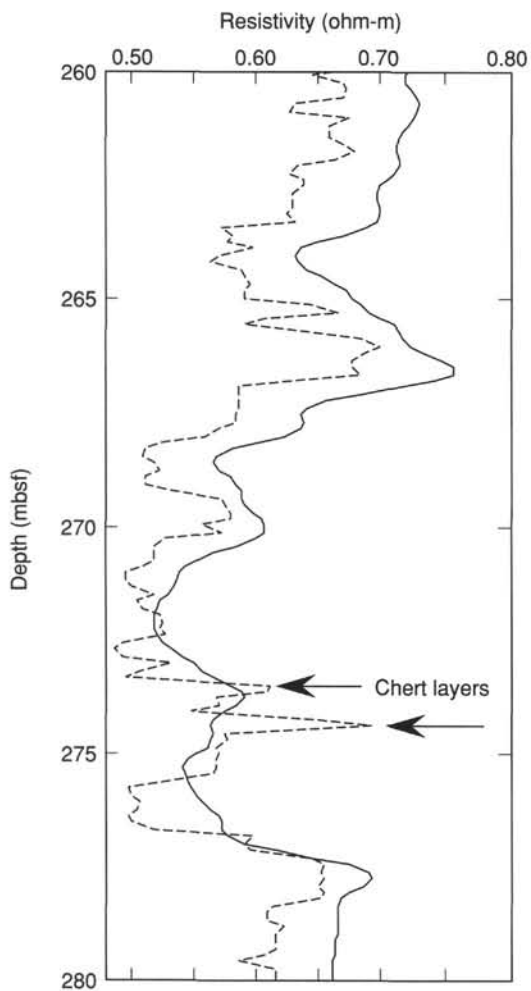


Figure 53. Intermediate resistivity (solid line) and shallow focused resistivity measurements (dashed line) vs. depth. Two peaks in shallow resistivity (marked with arrows) identify two distinct chert layers. Intermediate resistivity, which averages over a larger distance, shows only one peak.

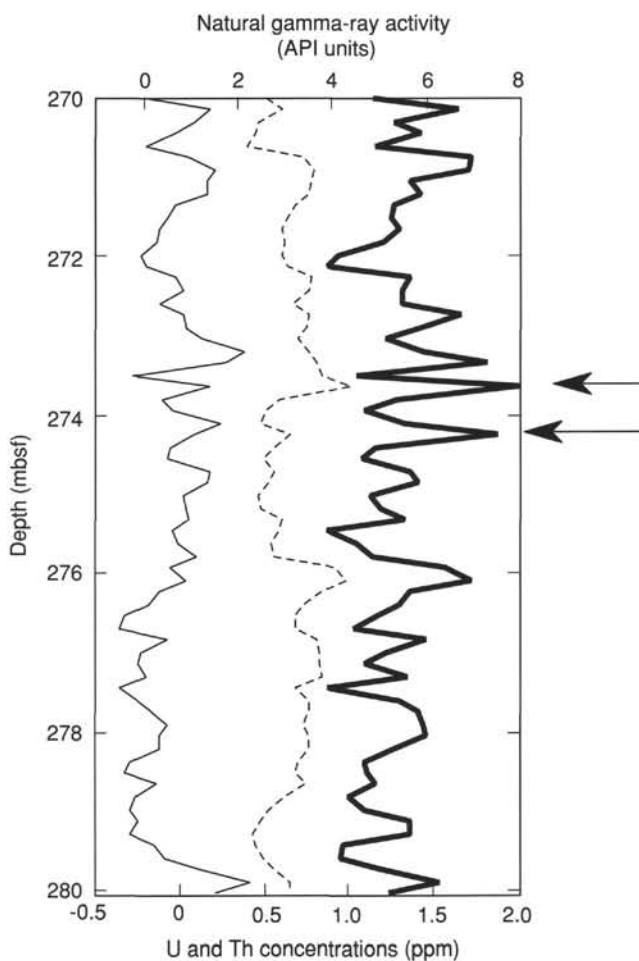


Figure 54. Natural gamma-ray activity (thick solid line), uranium concentration (dashed line), and thorium concentration (thin solid line) vs. depth from 270 to 280 mbsf. Positions of two chert layers are marked with arrows. Note that both chert layers are characterized by peaks in natural gamma-ray activities and thorium concentrations, but not uranium concentrations.

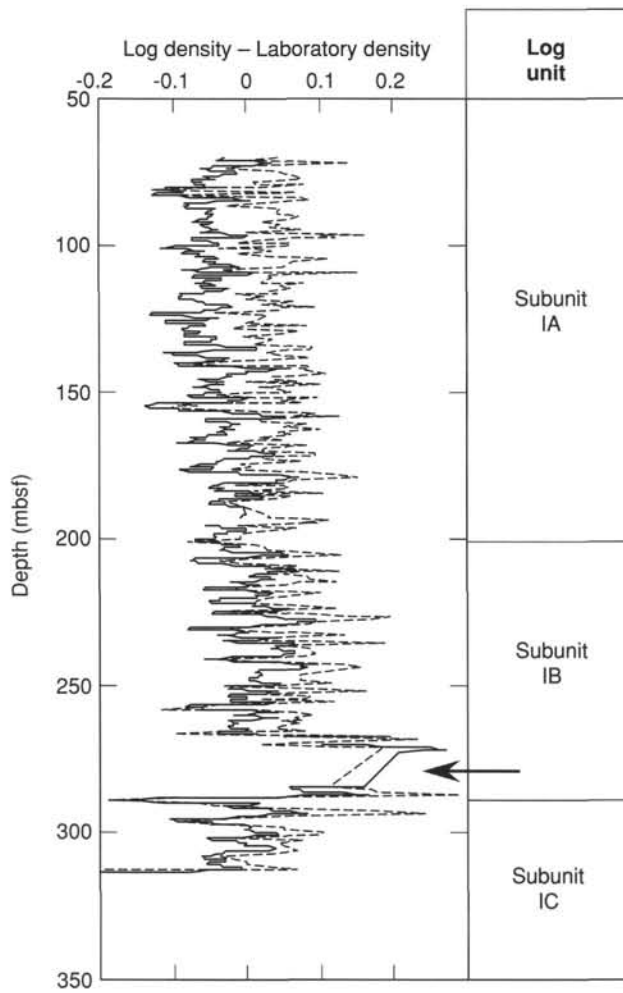


Figure 55. Delta density values vs. depth. Log density minus GRAPE density (solid line) and log density minus gravimetric density (dashed line). Arrow marks the silica-rich zone, much of which is characterized by poor core recovery. Log subunits are marked on right in figure.

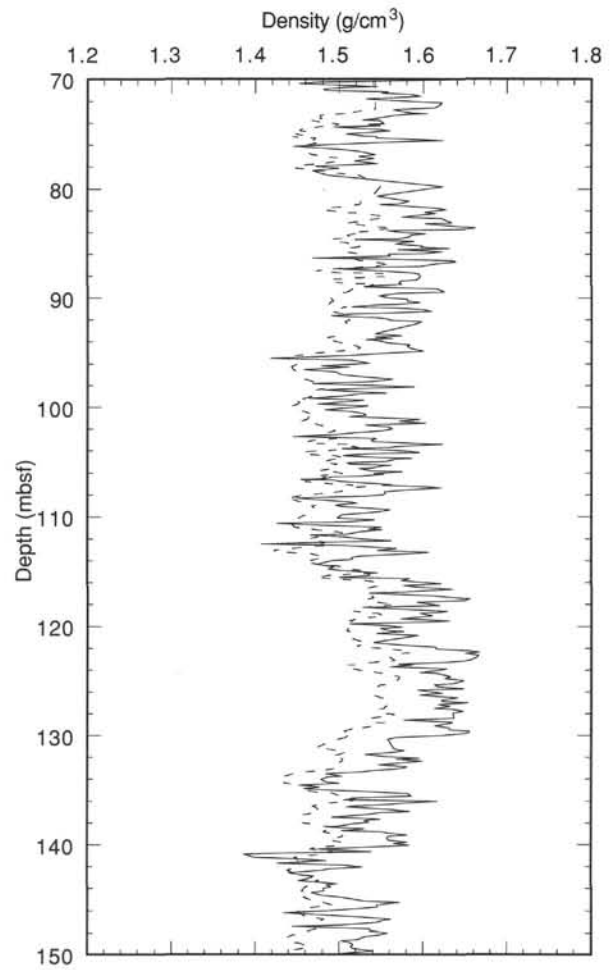


Figure 56. Comparison of Hole 851B GRAPE (solid line) and log density (dashed line) at interval from 70 to 150 mbsf.

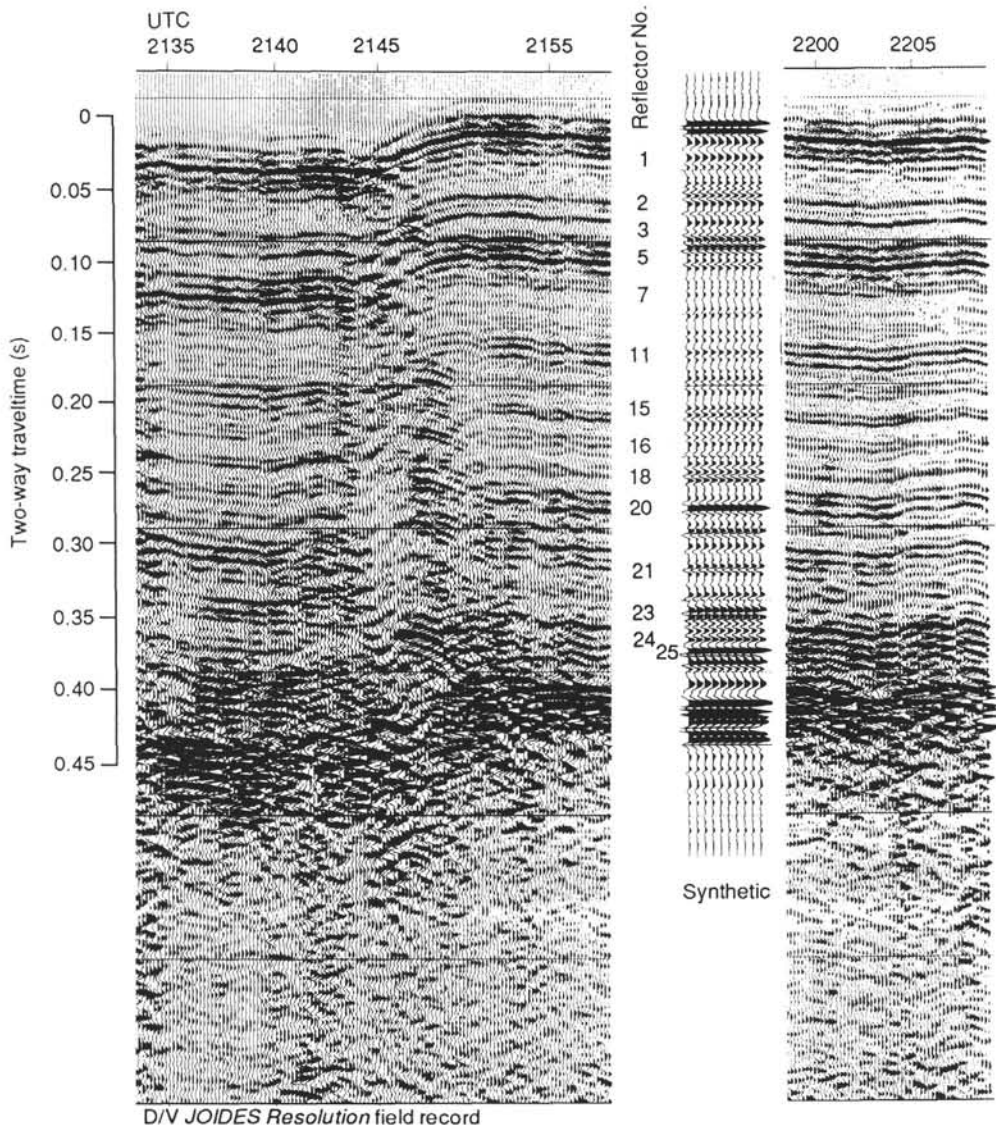


Figure 57. Comparison of synthetic seismogram with field record, Site 851.

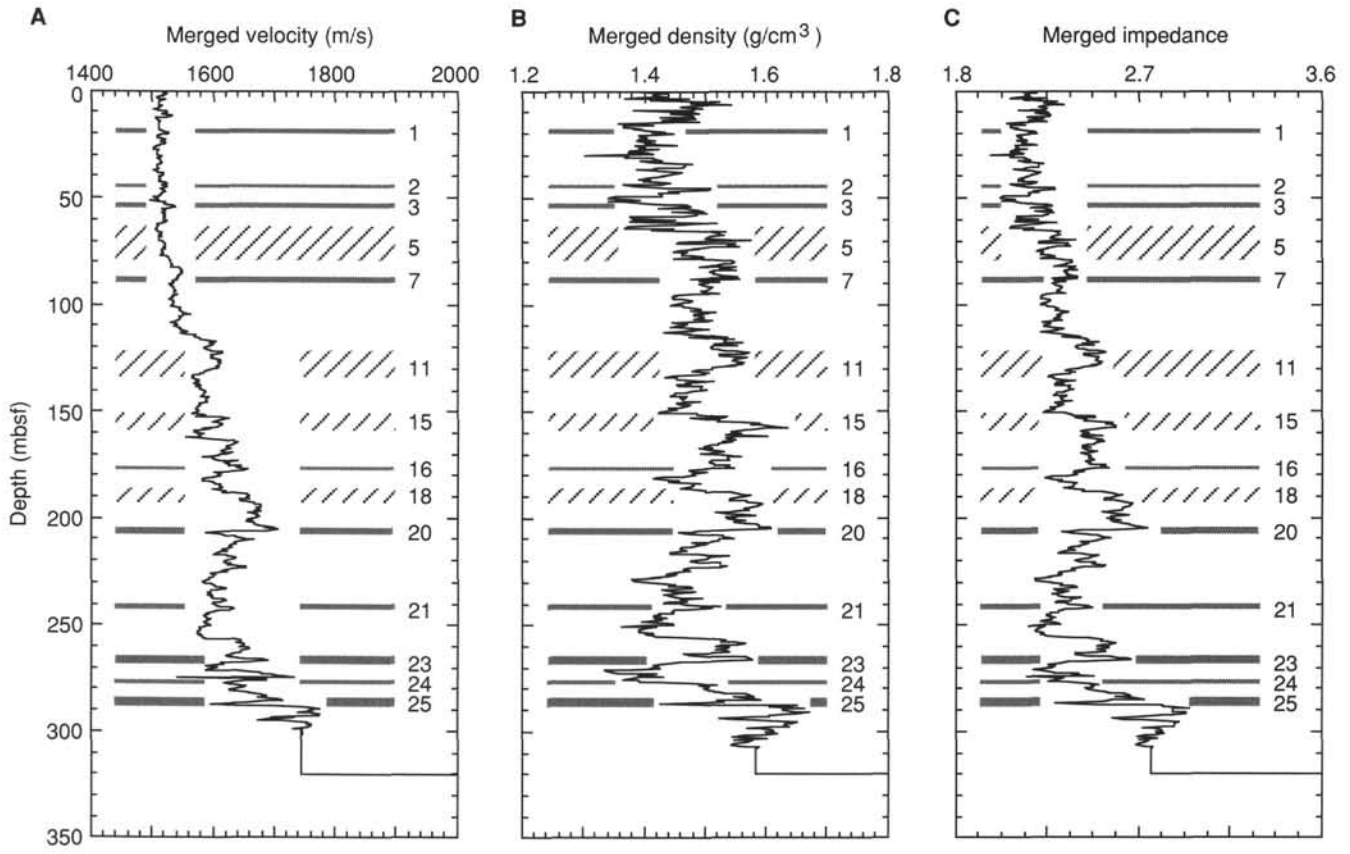


Figure 58. Velocity (A), density (B), and acoustic impedance (C) data used for generating Site 851 synthetic seismograms. The 14 reflectors picked from the synthetic seismogram are shown for comparison.

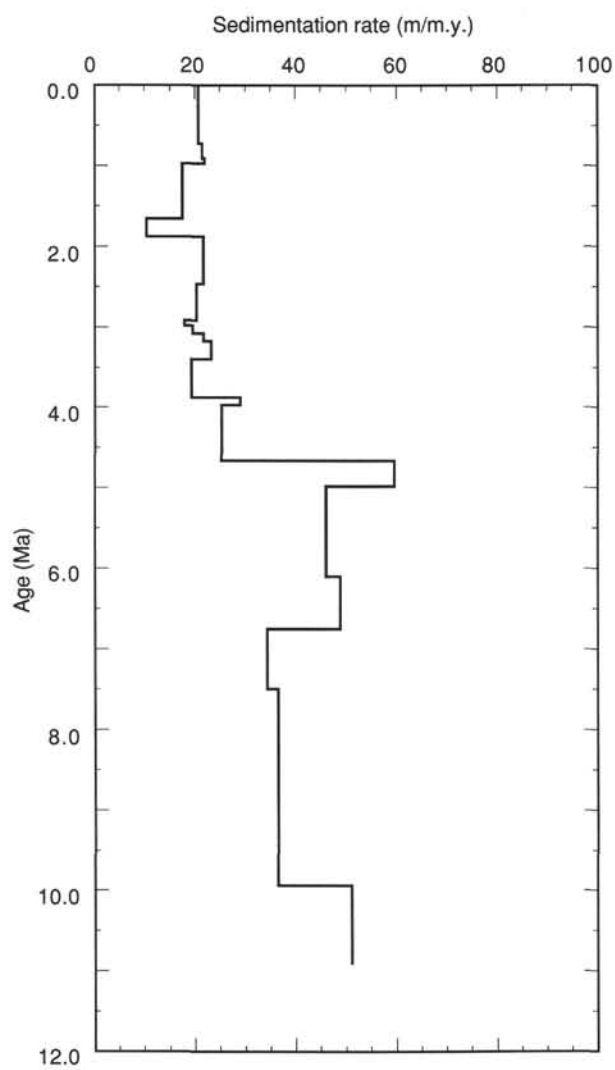
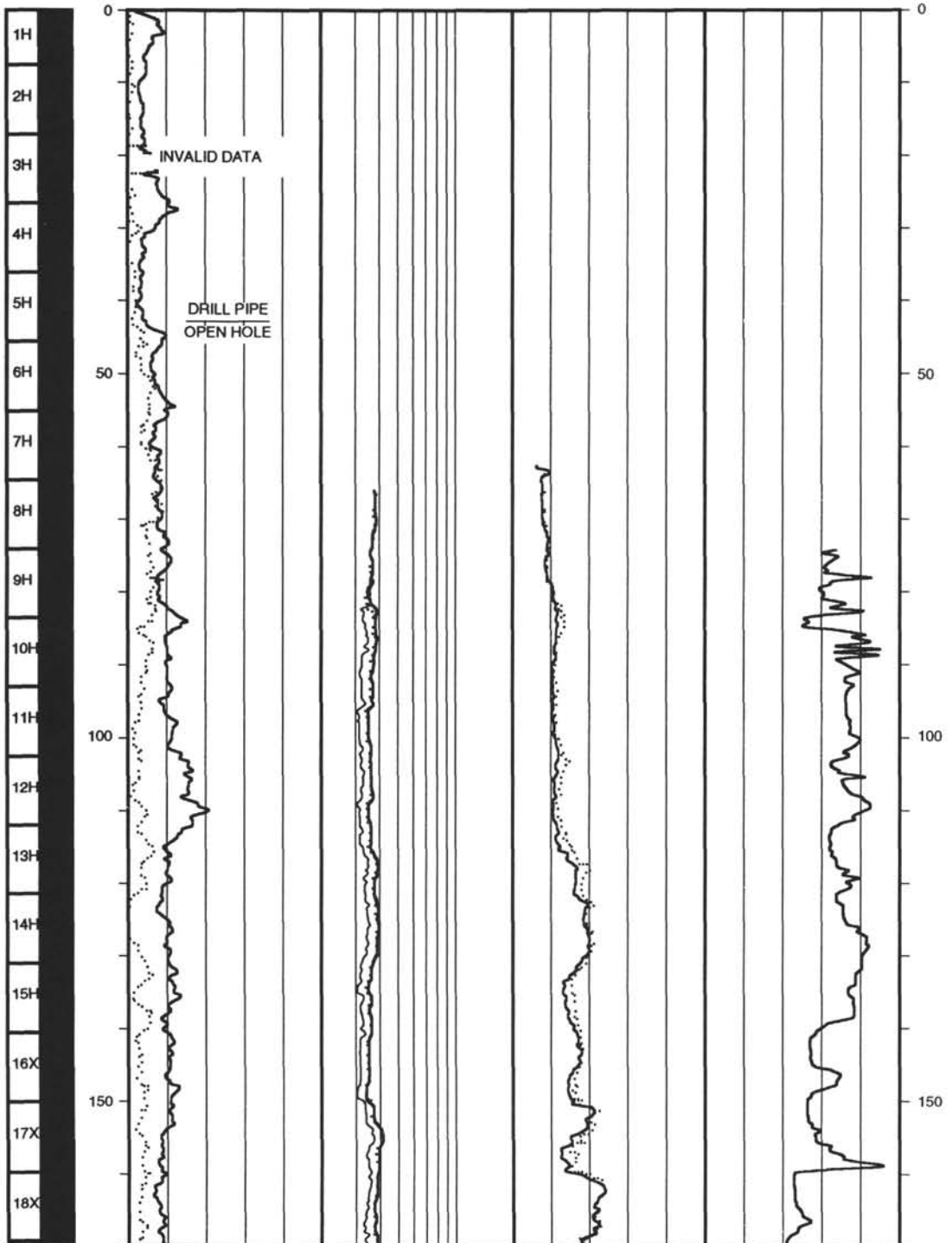


Figure 59. Sedimentation rate vs. sediment age at Site 851.

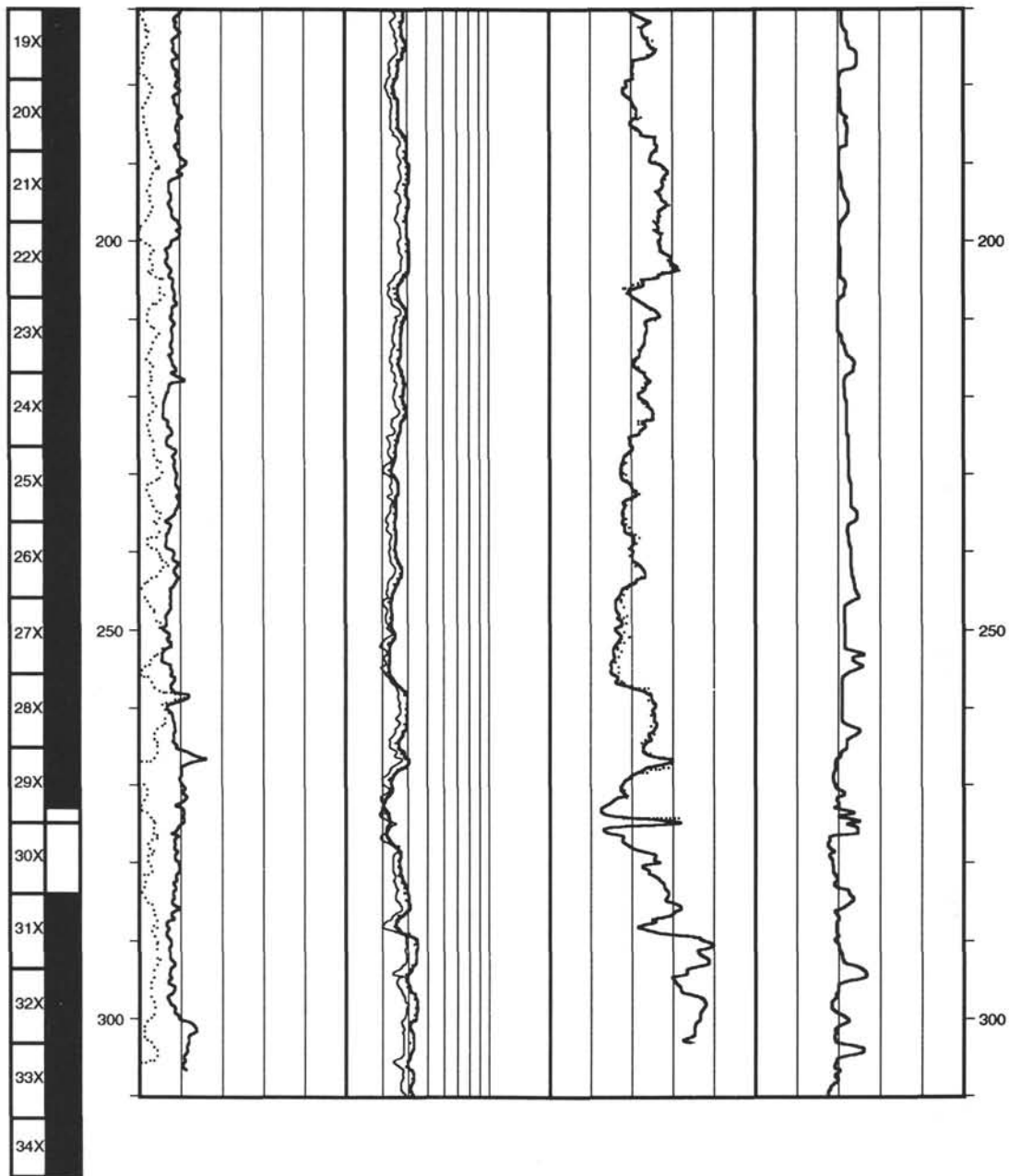
Hole 851B: Resistivity-Sonic-Natural Gamma Ray Log Summary

| CORE RECOVERY | RESISTIVITY | | | | | | | | | | DEPTH BELOW SEA FLOOR (m) |
|---------------|--------------------|-----------|------|---------|---------------|--------------|-------|---------|-----|---------|---------------------------|
| | SPECTRAL GAMMA RAY | | | FOCUSED | | TRANSIT TIME | | | | | |
| | COMPUTED | | | MEDIUM | | LONG-SPACING | | | | | |
| | 0 | API units | 30 | .2 | ohm·m | 2 | 210 | μs/ft | 160 | CALIPER | |
| TOTAL | | | DEEP | | SHORT-SPACING | | | CALIPER | | | |
| 0 | API units | 30 | .2 | ohm·m | 2 | 210 | μs/ft | 160 | 9 | in | 19 |



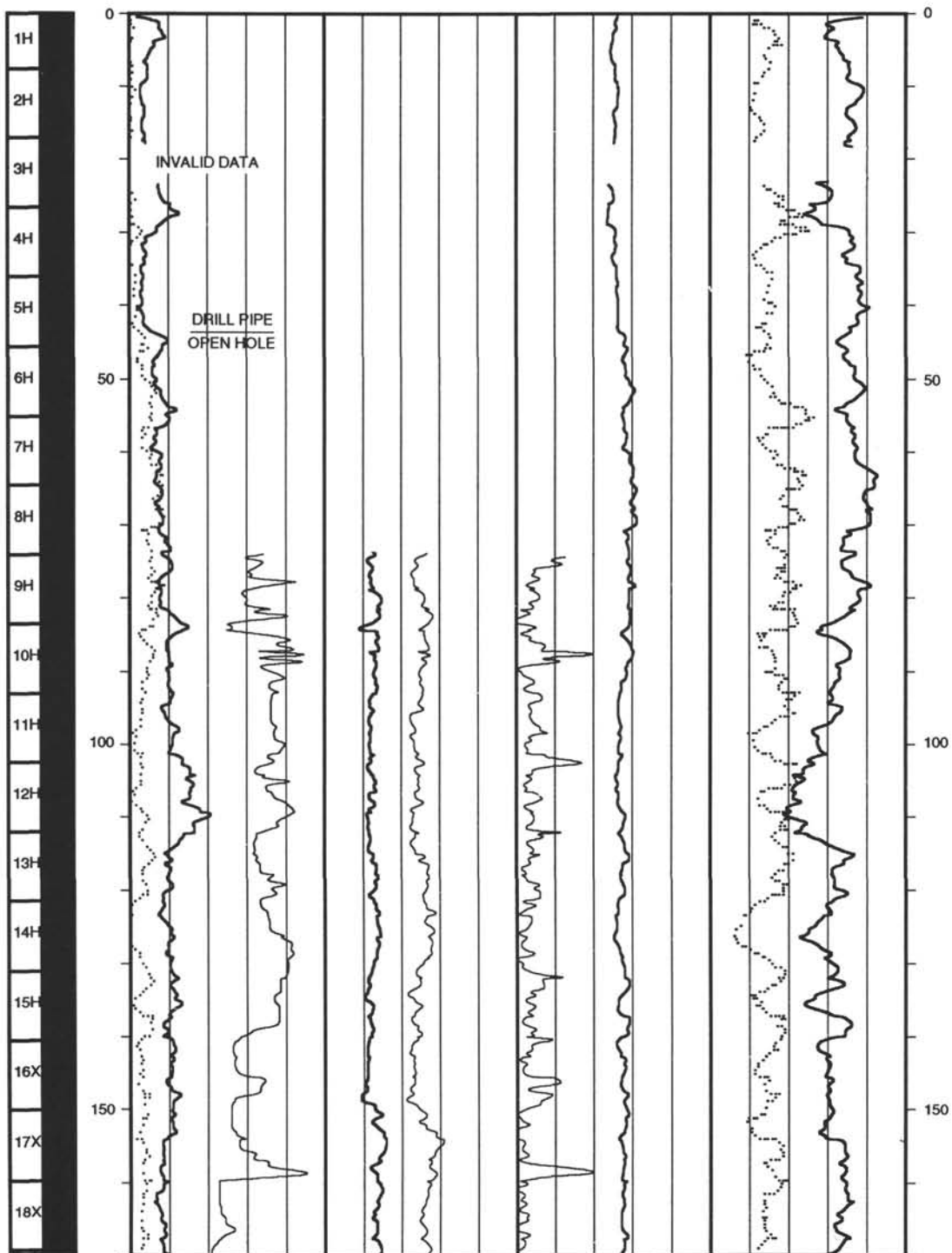
Hole 851B: Resistivity-Sonic-Natural Gamma Ray Log Summary (continued)

| CORE RECOVERY | DEPTH BELOW SEA FLOOR (m) | RESISTIVITY | | | | | | | | | | DEPTH BELOW SEA FLOOR (m) |
|---------------|---------------------------|--------------------|--------------|---------|-------|--------------|-----|---------------|-----|---------|----|---------------------------|
| | | SPECTRAL GAMMA RAY | | FOCUSED | | | | TRANSIT TIME | | | | |
| | | COMPUTED | | MEDIUM | | LONG-SPACING | | SHORT-SPACING | | CALIPER | | |
| | | 0 | API units 30 | .2 | ohm·m | 2 | 210 | μs/ft | 160 | 9 | in | |
| | | | | | | | | | | | | |

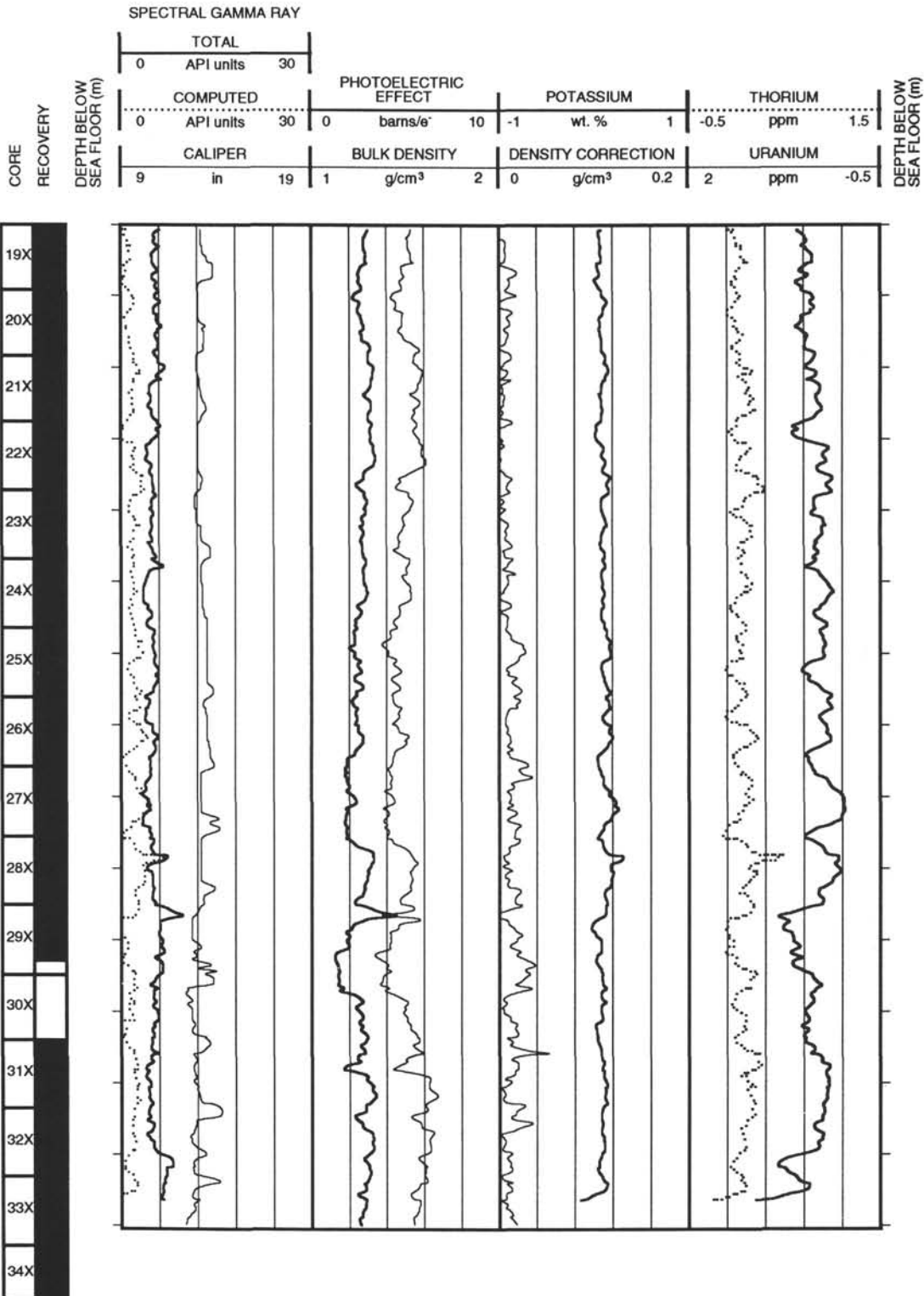


Hole 851B: Density-Natural Gamma Ray Log Summary

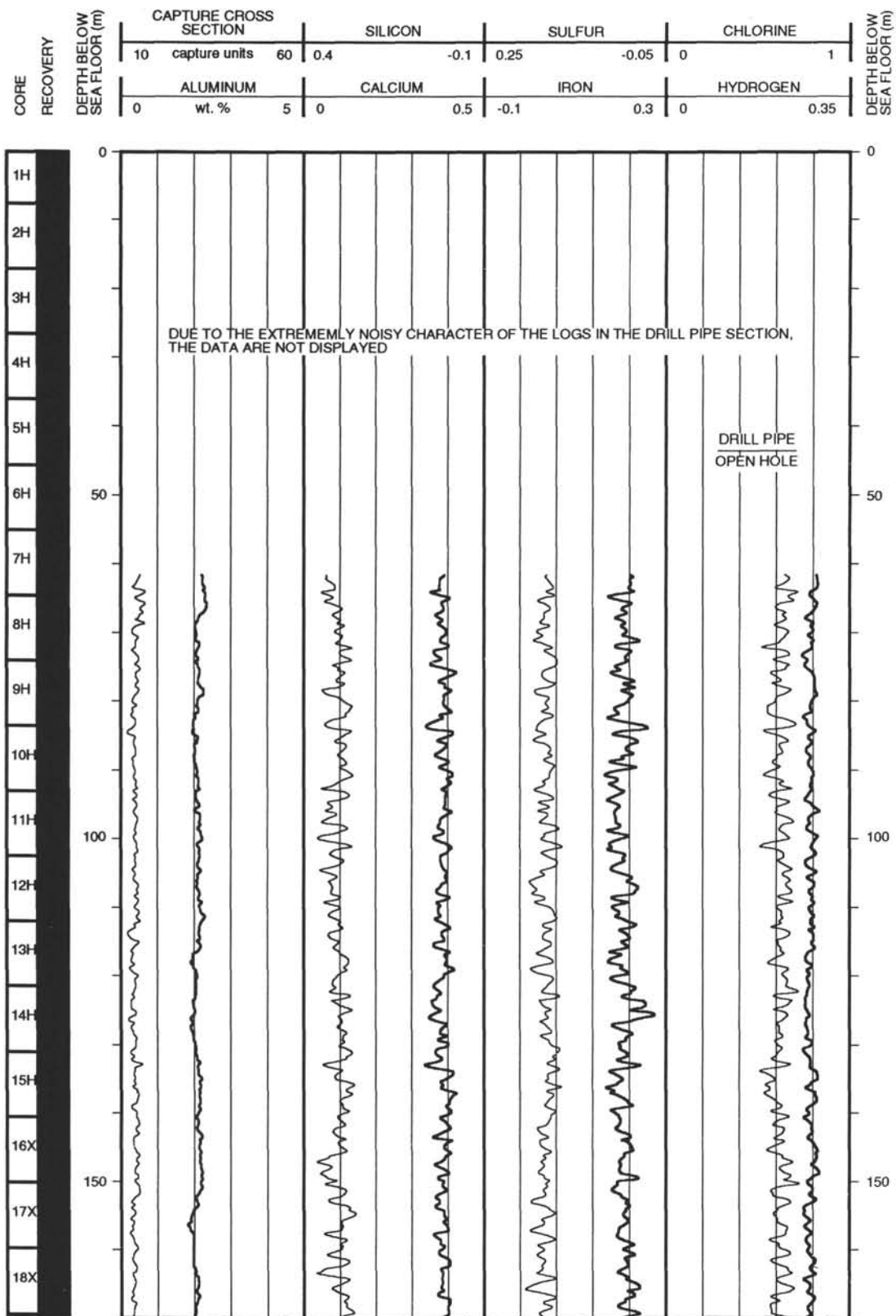
| | | SPECTRAL GAMMA RAY | | | | | | | | | | | |
|------------------|------------------------------|--------------------|-----------|-------------------------|-------|--------------------|-----------|---------|---------|------|--|------------------------------|--|
| CORE RECOVERY | DEPTH BELOW SEA FLOOR (m) | TOTAL | | PHOTOELECTRIC EFFECT | | | POTASSIUM | | THORIUM | | | DEPTH BELOW SEA FLOOR (m) | |
| | | 0 | 30 | 0 | 10 | -1 | 1 | -0.5 | 1.5 | | | | |
| | | API units | API units | barns/e ⁻ | wt. % | ppm | ppm | | | | | | |
| | | CALIPER | | BULK DENSITY | | DENSITY CORRECTION | | URANIUM | | | | | |
| | | 9 | 19 | 1 | 2 | 0 | 0.2 | 2 | ppm | -0.5 | | | |
| | | in | | g/cm ³ | | g/cm ³ | | | | | | | |



Hole 851B: Density-Natural Gamma Ray Log Summary (continued)



Hole 851B: Geochemical Log Summary



Hole 851B: Geochemical Log Summary (continued)

